PhD-FSTC-2017-05
The Faculty of Sciences, Technology and Communication

DISSERTATION

Defense held on 19/01/2017 in Luxembourg

to obtain the degree of

DOCTEUR DE L'UNIVERSITÉ DU LUXEMBOURG

EN PHYSIQUE

by

Jan SENDLER
Born on 01 November 1986 in Bonn, (Germany)

OPTICAL CHARACTERIZATION OF $Cu_2ZnSnSe_4$ THIN FILMS

Dissertation defense committee

Dr Susanne Siebentritt, dissertation supervisor
Professor, Université du Luxembourg

Dr Jan Lagerwall, Chairman
Professor, Université du Luxembourg

Dr Roland Sanctuary, Vice Chairman
Professor, Université du Luxembourg

Dr Charlotte Platzer Björkman
Professor, Uppsala Universitet

Dr Alex Redinger
Helmholtz-Zentrum Berlin

Abstract

CZTSSe is a suitable candidate for replacing $Cu(In,Ga)Se_2$ and CdTe as the absorber layer in thin film solar cells, because it is made up of earth abundant elements. However, CZTSSe based solar cells currently have a significantly lower conversion efficiency than competing technologies. This is mainly due to their V_{OC}-deficit. To understand the origins of this deficit, more research of the fundamental properties of CZTSSe is needed. This thesis deals with epitaxial CZTSe thin films in order to study the material properties without the influcence of grain boundaries. In the first main chapter of this thesis, the growth of epitaxial CZTSe thin films by two different growth processes of molecular beam epitaxy and their basic composition and structural characterization is described. The second main chapter shows, how spectroscopic ellipsometry can be used to extract information about the electronic structure of the epitaxial samples and that the electronic structure depends on the growth process and on the ordering state of the samples. The last main chapter contains temperature and excitation dependent photoluminescence measurement, which yield that the samples exhibit a fluctuating band structure. It is shown that the fluctuations are likely to be caused by band gap fluctuations and that the $Cu_{Zn} + Zn_{Cu}$ antisites, which depend on the ordering state of the sample, are probably not the reason for these fluctuations.

Contents

1. Introduction **7**

2. Growth of Epitaxial CZTSe Thin Films **9**

2.1. Introduction to CZTSe 9
2.1.1. Crystal Structure 9
2.1.2. Band Gap and Ordering of CZTSe 10
2.1.3. Phase Diagram 11
2.2. Basics of Molecular Beam Epitaxy of CZTSe thin films 12
2.2.1. Epitaxial Growth on GaAs 12
2.2.2. The PVD System 13
2.2.3. Previous Growth of Epitaxial Thin Films 15
2.3. Co-evaporation of CZTSe thin films 15
2.3.1. Growth Process 15
2.3.2. Ordering of CZTSe 17
2.4. Characterization of the Thin Films 18
2.4.1. Energy Dispersive X-ray Spectroscopy and Scanning Electron Microscopy 18
2.4.2. X-ray Diffraction 21
2.4.3. Raman Spectroscopy 25
2.4.4. X-ray Photoelectron Spectroscopy 30
2.4.5. Hall Measurements 32
2.4.6. Conclusion 33

3. Spectroscopic Ellipsometry **35**

3.1. Principles of Ellipsometry 35
3.1.1. Polarization of Light 35
3.1.2. The Ellipsometric Parameters 37
3.1.3. Dielectric Function and Joint Density of States 39
3.2. Ellipsometry Measurements 40
3.2.1. Variable Angle Spectroscopic Ellipsometry 40
3.2.2. Modelling of the Absorber Layers 42
3.3. Critical Point Analysis 46
3.3.1. Discussion 53

4. Photoluminescence **57**

4.1. Principles of Photoluminescence 57

4.2. Photoluminescence in a Semiconductor with a Fluctuating Band Structure 59
4.2.1. Density of States of a Heavily Doped Semiconductor 59
4.2.2. Band to Band Transitions 61
4.2.3. Band to Tail Transitions 62
4.2.4. Band to Impurity Transitions 64
4.2.5. Conclusion 65
4.3. Photoluminescence Measurements on Epitaxial CZTSe Thin Films 68
4.3.1. PL Setup 68
4.3.2. Measurements 69
4.3.3. Interpretation 74
4.3.4. The Cause of the Fluctuating Band Structure 79
4.3.5. The Effect of the Ordering Procedures 81
4.3.6. Summary 83

5. Conclusion **85**

A. Appendix **87**
A.1. Detailed XPS Scans 87
A.2. Fits of the Models to the Ellipsometric Parameters 89
A.2.1. Not annealed samples 89
A.2.2. Annealed Samples 94
A.3. Fits of the Second Derivative Spectra of $\tilde{\varepsilon}$ 96
A.4. Remaining PL Spectra 105

B. Acknowledgement **107**

C. List of Publications **109**

1. Introduction

Climate recordings show that the earth's surface temperature has been increasing since the 1950s in an unprecedented manner [1, 2]. Within the scientific community there is a consensus that this climate change has anthropogenic reasons, predominantly the emission of greenhouse gases due to the burning of fossil fuels [3, 4]. Even though it is a non-trivial task to accurately estimate the impact of global warming by a certain temperature, it is commonly accepted that there is an upper limit of temperature increase of $1.5 - 2\,°C$ with respect to the mean surface temperature before the industrialization, beyond which the consequences are very likely to be drastic and even uncontrollable for some societies [5]. In order to reach this target, a multitude of countries worldwide has policies in place, to increase the share of renewable energies and to decrease the burning of fossil fuels [6]. The European Union (EU) in particular has decided that by the year 2020 at least 20 % of the energy needs within the EU are to be covered by renewable sources [7].

A considerable share of these 20 % will be coming from photovoltaics (PV), which already constitutes $7 - 8\,\%$ of the electricity production in some countries [8]. Currently the market for PV modules is dominated by conventional silicon based technologies. Monocrystalline and multicrystalline silicon modules account for 90 % of the PV market. The rest of the market share is mainly held by thin-film technologies, among which copper indium gallium selenide $Cu(In,Ga)Se_2$ (CIGS) and cadmium telluride CdTe are the two largest fractions [9].

Despite their market share of currently only 10 %, thin film technologies have some advantages over the conventional silicon technology, that might increase this number in the future. Contrary to silicon, which is an indirect semiconductor, thin film solar cells utilize direct band gap semiconductors to absorb the sunlight. Due to the better absorption properties of a direct semiconductor, the light absorbing layer can be made roughly 100 times thinner, than in conventional silicon cells and consequently less material is needed. Furthermore, thin film mostly uses glass as a substrate. The advantage to this is, that a thin film module production line can utilize the know-how and the high capacity glass processing tools, which have been developed by the flat panel industry. This leads to a considerably higher throughput of a thin film production line. Ultimately, these two points result in a lower capital expenditure for thin films, which is an important number when installing a new production line [10].

However, the two leading thin film technologies have one common weak spot, which is that they contain the rare elements indium and tellurium respectively. Estimates indicate that the scarcity of these two elements might limit the production rate of these technologies to $10 - 100\,GW/a$ [11]. An additional problematic point in the case of $Cu(In,Ga)Se_2$ is that a significant percentage of the world's indium resources are located

in China. This might lead to a strategical dependence, if the PV industry of a country relies heavily on Chinese indium imports.

Therefore the direct band gap semiconductor compounds $Cu_2ZnSnSe_4$ (CZTSe) and the related Cu_2ZnSnS_4 (CZTS) have moved into focus as replacement for Cu(In,Ga)Se_2 and CdTe in thin film photovoltaic devices in the recent years([12]). CZTS(e) is derived from Cu(In,Ga)Se_2 by essentially replacing indium and gallium with zinc and tin. The main advantage of these compounds is that they consist of earth abundant elements, which avoids the possible bottlenecks indium and tellurium and potentially leads to lower material costs. This and the fact that the device structure can be copied from Cu(In,Ga)Se_2 devices, makes CZTS(e) a suitable replacement especially for Cu(In,Ga)Se_2 [13].

However, the main drawback of CZTS(e) devices is their shortcoming in terms of energy conversion efficiency, when compared to the market dominating technologies. The highest efficiency obtained on the lab scale for the sulphur-selenium alloy $Cu_2ZnSnSSe_4$ to this date is 12.6 % [14], while for pure CZTSe and CZTS it is 11.6 % [15] and 9.2 % [16] respectively. These are significantly lower than the maximum efficiencies for CdTe and CIGS, which have reached values of 22.1 % [17] and 22.6 % [18] respectively, and also lower than the maximum efficiency of crystalline silicon cells with 25.6 % [19].

It has been shown that the open circuit voltage V_{OC} of CZTS(e) devices is particularly low when compared to the theoretically highest V_{OC} possible, which can be estimated from the band gap of the absorber layer. This V_{OC}-deficit has been identified as the main reason for the low efficiencies [20]. As an explanation different mechanisms, like the existence of large band tails in the absorber [21] or interface recombination [22], have been proposed, but the exact origin of the open circuit voltage deficit is still not known.

It is therefore clear that a better understanding of both the device structure and of the fundamental properties of the absorber is needed in order to improve the performance of CZTS(e) based solar cells.

This thesis was written within the framework of the Marie Curie Initial Training Networks project Kestcells, initiated by the European Comission [23]. This project is aimed at studying the fundamental properties of CZTS(e) and its growth processes, the device structures of CZTS(e) based solar cells and the possibilities of industrial scale up.

The present work deals with the fundamental properties of the selenide compound CZTSe, with focus on epitaxially grown thin films. Epitaxial films have the property of containing no grain boundaries. It is known that grain boundaries have an effect on the material properties [24]. Therefore only single crystalline samples permit the study of the undistorted properties of CZTSe. The growth of epitaxial CZTSe thin films, which was done by molecular beam epitaxy, will be described in chapter 2. These samples were mainly characterized by spectroscopic ellipsometry and photoluminescence spectroscopy, which are the topics of the subsequent chapters 3 and 4. This thesis will be concluded with a summary and an outlook in chapter 5.

2. Growth of Epitaxial CZTSe Thin Films

This chapter describes the growth of epitaxial CZTSe thin films. The first part gives a brief overview of CZTSe itself. The second part introduces the concept of epitaxial growth and gives a summary of previous attempts to grow crystalline CZTSe thin films, since these are the basis for the present work. After that the growth of the samples is described. The subsequent part contains the characterization, that was performed besides spectroscopic ellipsometry and photoluminescence. The latter two will be described in greater detail in chapters 3 and 4.

2.1. Introduction to CZTSe

2.1.1. Crystal Structure

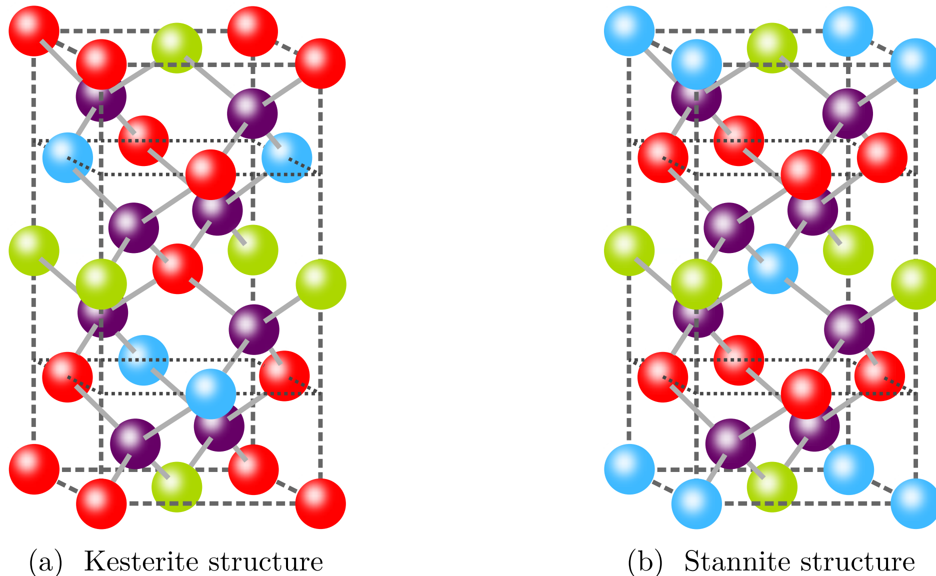

(a) Kesterite structure (b) Stannite structure

Figure 2.1.: CZTSe unit cell in the kesterite and the stannite structure. The color code is: Cu - red, Zn - blue, Sn - green, Se - purple. Courtesy of Germain Rey.

CZTSe is a member of the $A_2^{I}B^{II}C^{IV}X_4^{VI}$ compound family, with A = Cu, B = Zn, Fe, C = Sn and X = S, Se [25]. These compounds mainly occur in two different tetragonal crystal structures, the kesterite and the stannite type structure. Both structures can be

thought of as a cubic close-packed array of anions (X^{6-}), whose tetrahedral voids are occupied by cations (A^+, B^{2+} and C^{4+}). Both structures are characterized by different cation arrangements. In the kesterite structure the cations are arranged in alternating layers of CuSn and CuZn, which results in the space group $I\bar{4}$. In the stannite structure the cations form alternating layers of ZnSe and Cu_2, which leads to a $I\bar{4}2m$ space group. The unit cell of CZTSe in both the kesterite and the stannite structure is shown in figure 2.1.

It was theoretically predicted that the kesterite structure is energetically more favorable than the stannite structure [26, 27]. This result was confirmed by Schorr et al., who showed that both CZTS and CZTSe crystallize in the kesterite structure, by using neutron diffraction [25]. The lattice parameters a and c of CZTSe in the kesterite structure were found to be $a_{\mathrm{CZTSe}} = 5.695\,\text{Å}$ and $c_{\mathrm{CZTSe}} = 11.345\,\text{Å}$ [28].

2.1.2. Band Gap and Ordering of CZTSe

The band gap of CZTSe in the kesterite structure was theoretically calculated to be $1.00 - 1.05\,\mathrm{eV}$ [27, 29, 30]. However, Schorr et al. showed that in the kesterite structure disorder of Cu and Zn atoms in the $z = 1/4$ and $z = 3/4$ planes occurs, which results in the formation of $\mathrm{Cu_{Zn}} + \mathrm{Zn_{Cu}}$ antisites [25]. The degree of ordering can be described by introducing a long-range order parameter S, which is 1 in the case of a perfectly ordered unit cell, as shown in figure 2.1a, and 0 in the case of total randomisation of Cu and Zn, as shown in figure 2.2 [31]. The value of S for a given CZTSe sample

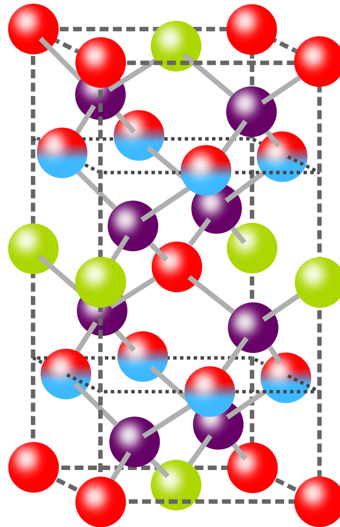

Figure 2.2.: Completely disordered CZTSe unit cell in the kesterite structure: $S = 0$. The color code is the same as in figure 2.1. The blue-red spheres represent the total randomisation of Cu and Zn. Courtesy of Germain Rey.

depends on its growth history. It was found by Scragg et al. that the transition between the ordered and the disordered state in the sulfide compound CZTS is a second order phase transition with a critical temperature T_C [32]. For temperatures $T < T_\mathrm{C}$ the

order parameter S takes on finite values in the equilibrium state and converges to 1 for $T \to 0\,\mathrm{K}$. For temperatures above the critical temperature it quickly decreases to 0. It needs to be stressed that the time, which is needed for S to reach its equilibrium value, depends on the temperature. The lower the temperature the longer this time is, as was demonstrated in [32]. At room temperature a sample can be regarded as virtually stable in terms of the ordering parameter.

Rey et al. observed an analogous behavior for CZTSe and determined its critical temperature to be $T_C \approx 200\,°\mathrm{C}$ [33]. Since CZTSe samples are generally fabricated at higher temperatures this means that they have a considerable degree of disorder. The most prominent effect of the $Cu_{Zn} + Zn_{Cu}$ antisites on the electronic structure is a reduction of the band gap with respect to the completely ordered structure. Rey et al. showed that subjecting a fully disordered CZTSe sample to an ordering procedure, which is a long-time annealing at temperatures below 200 °C, could increase the band gap by up to 110 meV [33]. Therefore, when comparing the band gap values of different CZTSe samples, it is necessary to take the growth process into account, since it is very likely to affect the ordering state.

2.1.3. Phase Diagram

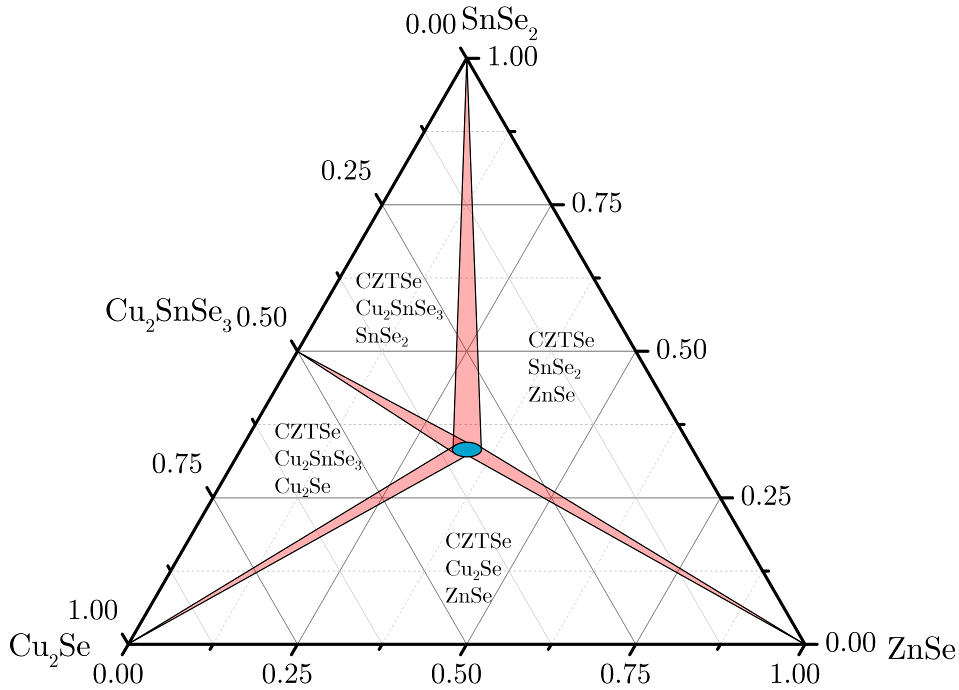

Figure 2.3.: Quasi-ternary phase diagram for CZTSe. The blue area represents the single phase existence region of CZTSe. In the red areas CZTSe co-exists with one of the respective secondary phases. Adapted from [34] and [35].

Phase diagrams are a useful tool for estimating the phase content of a sample based

on its elemental composition. Instead of studying the phase content of a CZTSe sample in the elemental Cu-Zn-Sn-Se system, Piskach et al. developed quasi-ternary phase diagram, which is based on the following decomposition reaction of CZTSe [34]:

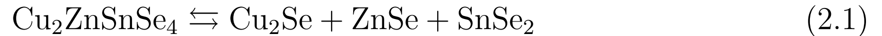

$$Cu_2ZnSnSe_4 \leftrightarrows Cu_2Se + ZnSe + SnSe_2 \tag{2.1}$$

In this expression a stoichiometric amount of selenium is assumend, meaning that no phases with differing Se-content, as CuSe or SnSe, can occur and that the system is in thermal equilibrium. With the Se-content fixed, the sample composition can be described in the quasi-ternary system Cu_2Se-ZnSe-$SnSe_2$.

An isothermal section of this system is depicted in figure 2.3. In this representation the pure CZTSe phase can exist in a small region in the center of the diagram, which is colored in blue. The size of the single phase existence region, as it is shown here, is not to scale. However, calculations indicate that it is not very large [36]. The red areas are the regions, in which CZTSe co-exists with one of the corresponding secondary phases Cu_2Se (copper selenide), Cu_2SnSe_3 (copper tin selenide), $SnSe_2$ (tin selenide) and ZnSe (zinc selenide). These areas are not to scale as well. In the remaining areas, which make up the majority of the phase diagram, CZTSe exists together with two additional secondary phases.

By determining a sample's elemental composition and plotting it in the quasi-ternary phase diagram, it is possible to estimate, if and which secondary phases might occur. However, it should be kept in mind that this phase diagram assumes a stoichiometric Se-content and that it was originally derived under thermal equilibrium conditions at a temperature of 670 K [34]. Therefore the existence or non-existence of any secondary phases, which is established based on the position in the phase diagram, should be treated with caution.

2.2. Basics of Molecular Beam Epitaxy of CZTSe thin films

2.2.1. Epitaxial Growth on GaAs

The term *epitaxy* describes the deposition of a crystalline layer onto a crystalline substrate. As a consequence the deposited layer features only one well defined orientation, which is determined by the crystal orientation of the substrate, and therefore does not exhibit any grain boundaries.

A prerequisite for epitaxial growth is that layer and substrate have similar lattice parameters. If the thickness of the deposited layer is much smaller than the thickness of the substrate [1] the lattice mismatch f can be defined as [37]:

$$f = \frac{a_S - a_L}{a_L} \tag{2.2}$$

[1] It will be shown later that this applies to the CZTSe films studied here. Their thickness of around 1 µm is considerably smaller than the substrate's thickness of 500 µm.

Here a_S and a_L are the lattice parameters of substrate and film respectively. If this so defined lattice mismatch is of the order of 1 % or smaller the layer may adopt the lattice parameter of the substrate and grow without any structural defects [37]. This is called *pseudomorphic* growth.

The adoption of the substrate's lattice parameter introduces either compressive or tensile strain in the layer, depending if f takes on negative or positive values. As soon as the thickness of the film reaches a critical value this strain will be released by the introduction of structural defects. From this *critical thickness* on the film will continue to grow with, or with a lattice parameter close to, its unstrained lattice parameter.

As it was mentioned in section 2.1.1, the lattice parameters of CZTSe in the kesterite structure are $a_{\mathrm{CZTSe}} = 5.695\,\text{Å}$ and $c_{\mathrm{CZTSe}} = 11.345\,\text{Å}$ [28]. One suitable substrate for the epitaxial growth of CZTSe is GaAs, which crystalizes in the zincblende structure with the lattice parameter $a_{\mathrm{GaAs}} = 5.65325\,\text{Å}$ [38].

Calculating the lattice mismatch according to equation 2.2 for the lattice parameter a_{CZTSe} and half the lattice parameter c_{CZTSe} yields:

$$f_{\mathrm{a}} = \frac{a_{\mathrm{GaAs}} - a_{\mathrm{CZTSe}}}{a_{\mathrm{CZTSe}}} = -7.3 \cdot 10^{-3} \tag{2.3}$$

$$f_{\mathrm{c}} = \frac{a_{\mathrm{GaAs}} - 0.5 \cdot c_{\mathrm{CZTSe}}}{0.5 \cdot c_{\mathrm{CZTSe}}} = -3.4 \cdot 10^{-3} \tag{2.4}$$

Both mismatches are smaller than 1 % and therefore both the a and the c lattice parameter are compatible with epitaxial growth on GaAs(001) substrates. In fact it has been shown that CZTSe can grow epitaxially on GaAs(001) with the c-axis parallel to the [001]-direction, which means the unit cell is ”standing”, and with the c-axis parallel to the [010]- and the [100]-direction, which corresponds to the unit cell ”lying” on the substrate [39].

2.2.2. The PVD System

Figure 2.4 shows a sketch of the PVD system, which was used to grow the CZTSe samples.

It consists of a growth chamber, which is evacuated to a base pressure of $\sim 10^{-8}$ torr by a turbo pump, and an additional liquid nitrogen cooling. For the evaporation of the raw materials four effusion cells for copper (Cu), zinc (Zn), tin (Sn) and tin selenide (SnSe) and one valved cracker source for selenium (Se) are used. The effusion cells are equipped with heated filaments at the bulk and at the tip of the source and a shutter system, which is able to close the sources individually.

The flux is determined by the bulk temperature of the source, while the tip is heated to avoid condensation. In case of the Se-source the flux is controlled by the bulk temperature and the position of the valve and is in the range of $0.5 - 1.0 \cdot 10^{-5}$ torr. The function of the cracker nozzle, which is set to considerably higher temperatures than the bulk, is to break up the Se_n rings (with n between 2 and 8) into mainly Se_2 molecules. This is

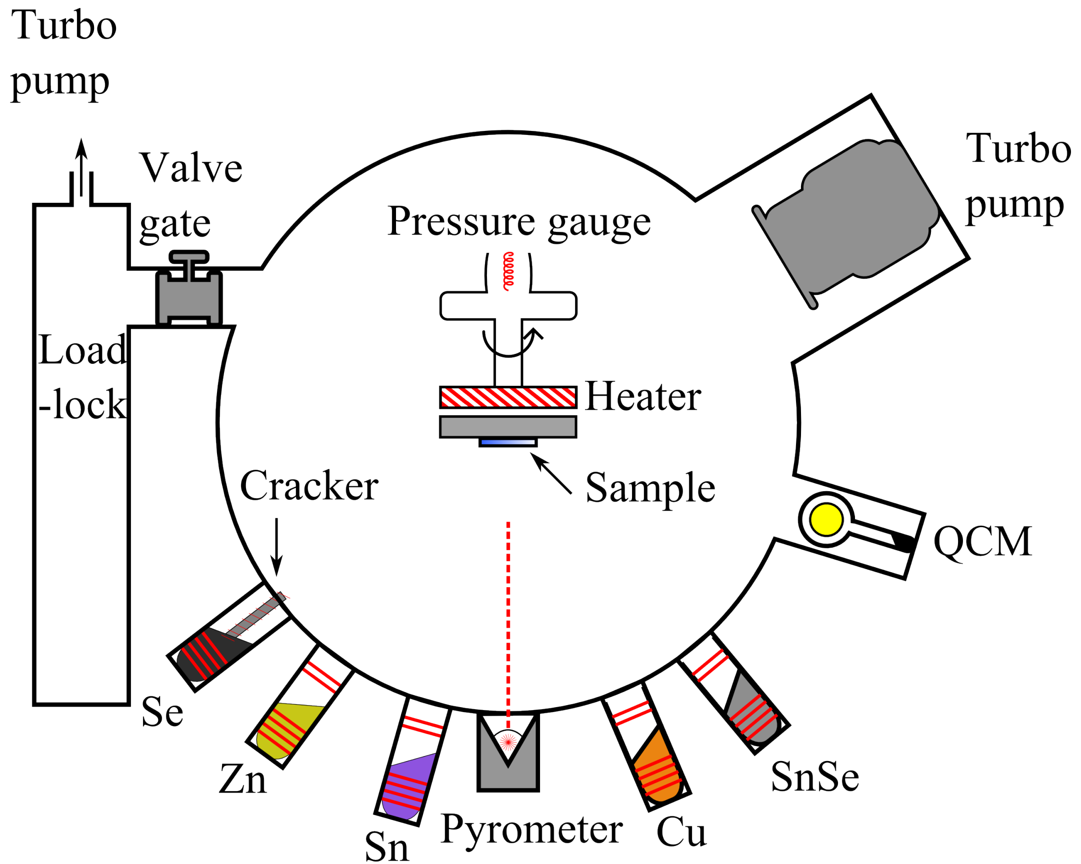

Figure 2.4.: Sketch of the PVD system.

done in order to increase the reactivity of the selenium, which benefits its incorporation into the sample [35].

The fluxes are monitored with a pressure gauge and a quartz crystal monitor (QCM) prior to the growth process.

The substrate, a quarter of an undoped GaAs-wafer, is mounted onto a rotating sample holder. The rotation aids in increasing the uniformity of the sample. The back of the sample holder consists of either a molybdenum plate or a Zn-doped GaAs-wafer, which is heated via thermal radiation from a heater located behind the sample holder. This additional backplate was necessary, since undoped GaAs has no free charge carries and consequently does not absorb photons with energies below its band gap. Therefore it cannot be heated efficiently with thermal radiation from the heater, but it needs to be heated by heat transport from the backplate.

The substrate temperature before growth is measured with a pyrometer, which is calibrated to GaAs and sensitive in the wavelength range of $0.90 - 0.97\,\mu\text{m}$ and in the temperature range of $400 - 1000\,^{\circ}\text{C}$.

2.2.3. Previous Growth of Epitaxial Thin Films

Previously Redinger et. al. used the PVD system described in the preceding section to deposit epitaxial thin films on Zn-doped GaAs-substrates, employing a multistage high temperature co-evaporation process [35]. This process was adapted from the process used by Repins et. al. to deposit polycrystalline CZTSe absorber layers, which yielded a total-area efficiency of 9.15 % in the finished device [13]. In the first stage of the process used by Redinger et. al. all five sources of the PVD are open. To measure the sample temperature they used a pyrometer calibrated to molybdenum coated glass, which was used for the growth of polycrystalline absorber layers. The heater was adjusted such that the sample temperature measured at the end of the growth process was about 450 °C. These high temperatures are needed to facilitate the formation of the CZTSe-phase.

The second stage acts as annealing stage. For this stage the Cu and the Zn source are closed, while the heater temperature is kept constant. This aims at improving the crystal quality. During the annealing stage the SnSe, the Sn and the Se-source are kept open to prevent the decomposition of CZTSe [40]:

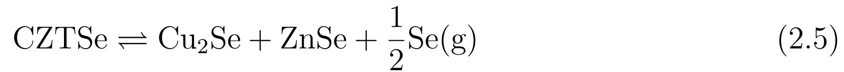

$$\mathrm{CZTSe} \rightleftharpoons \mathrm{Cu_2Se} + \mathrm{ZnSe} + \frac{1}{2}\mathrm{Se(g)} \quad (2.5)$$

It was shown that the film thickness does not increase substantially in this stage [35].

After the annealing stage the sample is cooled down under a Se-supply.

It was found that the sample composition is distributed parallel to the Cu_2SnSe_3-ZnSe tie-line in the quasi-ternary phase diagram, which is the line formed by the CZTSe-Cu_2SnSe_3 and the CZTSe-ZnSe existence regions (see figure 2.3). The composition can be shifted along this line by varying the Cu-flux during growth.

The samples were grown epitaxially, which was confirmed by XRD [35]. Only Cu-poor and Zn-rich samples showed a small polycrystalline inclusion but they were still highly oriented. Raman and EDX analysis showed the presence of the secondary phases ZnSe and Cu_2SnSe_3 grown epitaxially on top of the CZTSe. Especially a sample close to stoichiometry (Cu/(Zn+Sn) = 0.93 and Zn/Sn = 0.96) showed an inhomogeneous surface in the SEM micrograph with ZnSe patches on top.

2.3. Co-evaporation of CZTSe thin films

2.3.1. Growth Process

The samples studied in this work were grown with two different growth processes adapted from the process used by Redinger et al. [35]. The two processes are shown in figure 2.5. The upper part of the graphs shows the set-point temperature of the heater and the lower part shows the fluxes from the different sources as a function of time in arbitrary relative units, based on the pressure gauge readings.

The first type of process (figure 2.5a) is similar to the process from [35], since it contains the same three stages: the deposition stage during which all five sources (Cu,

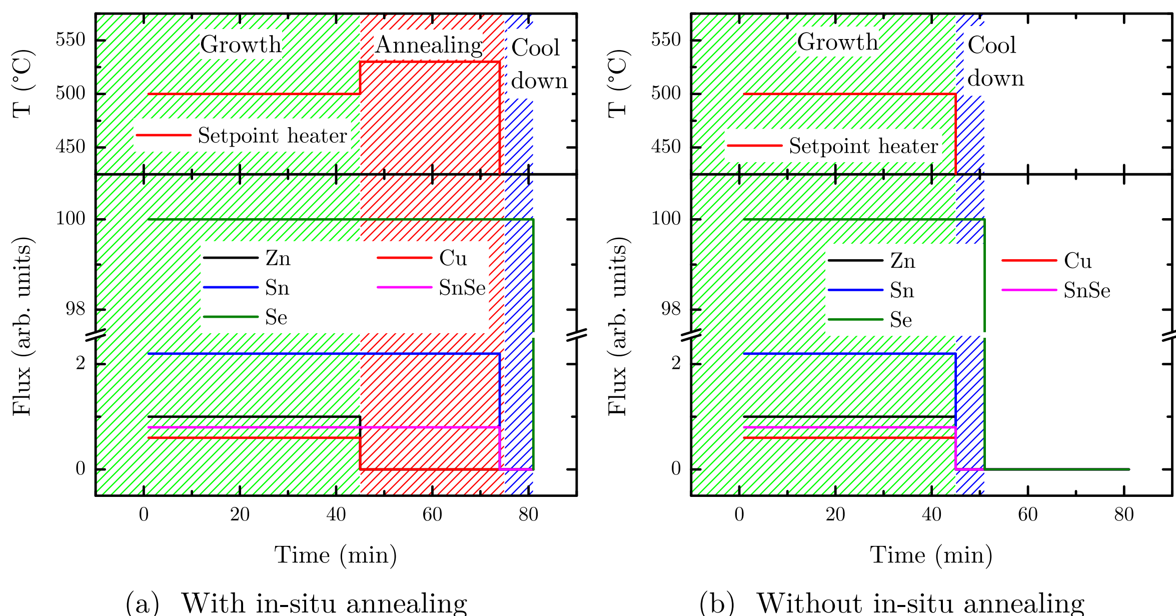

(a) With in-situ annealing

(b) Without in-situ annealing

Figure 2.5.: Sketch of the two different co-evaporation processes used in this work showing the times, during which the different sources were open. The growth process with the in-situ annealing stage is shown in figure a while figure b shows the growth process without annealing stage.

Zn, Sn, SnSe and Se) are open, the annealing stage, during which only Sn, Se and SnSe are evaporated to prevent the decomposition of CZTSe and the cooldown stage, during which the Se-source is open.

In the second type of process (figure 2.5b) the annealing stage is omitted and the deposition stage is followed directly by the cooldown stage.

The main difference to reference [35] is that the pyrometer, which was used in this work, was specifically designed to measure the temperature of GaAs wafers. Therefore the substrate temperature could be measured before the growth process started. The heater set-point was adjusted such that the substrate temperature before growth was in the range of approximately 440 °C to 460 °C. The exact value, with an uncertainty of about 3 °C coming from fluctuations of the pyrometer reading, was varied among the different samples.

In the annealing stage of the first type of process the temperature reading decreased as soon as the Cu and the Zn-source were closed. This can be attributed to a significant amount of heating by the Cu-source in particular, since it was operated at a bulk temperature of around 1000 °C. For this reason the heater temperature was increased in this stage in an attempt to bring the substrate temperature during growth and annealing stage to the same value.

The size of this temperature step, and if it was included, was varied amongst the different runs as well.

These two growth processes described here were used to grow a series of samples. In

the subsequent discussion these samples will be referred to as annealed samples if they were grown with the first type of process with the in-situ annealing stage. The samples grown with the second type of process, without the in-situ annealing, will be referred to as not annealed samples.

2.3.2. Ordering of CZTSe

As was shown in section 2.1.2, as grown CZTSe samples exhibit a varying degree of disorder, which can be reduced by annealing the sample at temperatures below the critical temperature T_C.

In this work two different ordering procedures were applied to two different samples to increase their degree of ordering. The first procedure, shown in figure 2.6b, consists of several steps with different dwell times at different temperatures. The dwell times and temperatures are: 80 min at 175 °C, 120 min at 150 °C, 600 min at 125 °C, 1200 min at 100 °C and 1200 min at 75 °C. In the other procedure, shown in figure 2.6b the sample is kept at 100 °C for 5000 min and is then cooled down to room temperature with a rate of −0.06 °C/min. In the following sections the former procedure will be referred to as ordering process 1, the latter procedure will be referred to as ordering process 2. Both procedures were performed in a tube furnace, which was evacuated after being purged with nitrogen.

Additionally a disordering procedure was applied to one not annealed, as grown sample. It consists of an annealing stage of 60 min under vacuum at a dwell temperature of 250 °C with a subsequent quenching by nitrogen. The sample, which was subjected to this procedure, will be referred to as disordered. An overview of the samples, and with which ordering or disordering procedure they were treated, is given in table 2.1 in section 2.4.1.

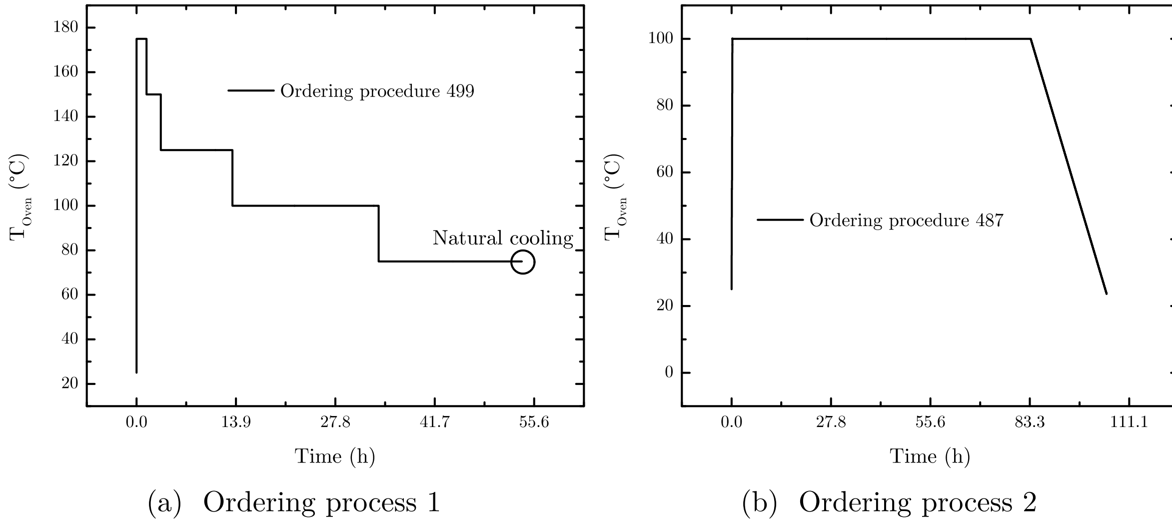

(a) Ordering process 1 (b) Ordering process 2

Figure 2.6.: Temperature profiles of the two ordering processes used in this work.

2.4. Characterization of the Thin Films

This section contains the basic compositional, structural and electric characterization of the samples, that were produced with the growth processes described previously. The detailed characterization using photoluminescence and ellipsometric spectroscopy is discussed in chapters 3 and 4.

2.4.1. Energy Dispersive X-ray Spectroscopy and Scanning Electron Microscopy

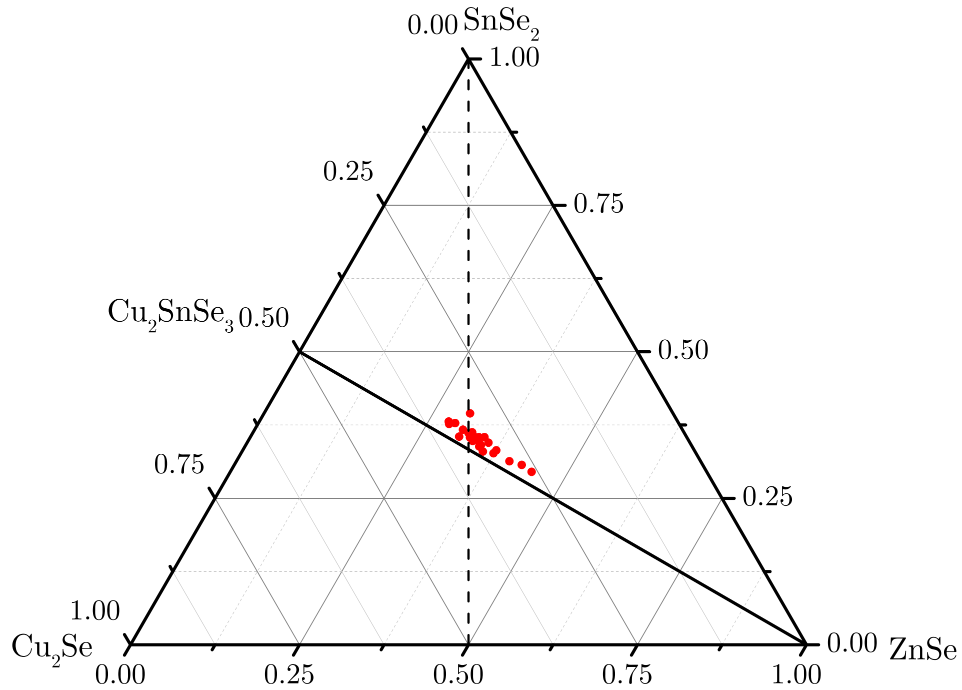

Figure 2.7.: Compositions of both the annealed and the not annealed samples plotted in the quasi-ternary phase diagram. The samples are distributed slightly above the Cu_2SnSe_3-ZnSe tie-line (solid line). The position is determined by the Cu-flux during growth. The dashed line acts as a guide for the eye and the intersect with the tie-line marks the stoichiometric region of CZTSe.

The elemental compositions of the samples were determined by energy dispersive X-ray spectroscopy (EDX) by Maxime Thevenin and Michele Melchiorre at the University of Luxembourg. The basic principle of this measurement technique is that a beam of high-energy electrons (on the order of 10 keV) is directed onto the sample. The electrons of the beam then excite inner shell electrons of atoms inside the sample. Upon deexcitation the atoms emit characteristic X-rays which can then be detected. By analyzing these X-rays it is possible to determine which elements are present in the sample [41].

For this work a scanning electron microscope equipped with a silicon drift detector and an acceleration voltage of 20 kV was used.

Figure 2.7 shows the elemental compositions, in terms of the atomic percentage, of both the annealed and the not annealed samples in the quasi-ternary phase diagram. In this representation the samples lie slightly above and parallel to the Cu_2SnSe_3-ZnSe tie-line, regardless of the growth process.

The position along this tie-line can be varied by solely varying the Cu-flux during the deposition stage, as has been shown previously [35]. This is a consequence of the fact that Cu is needed to incorporate Sn into the sample and that the growth takes places in an excess Sn environment.

In case of a high Cu-supply ($Cu/Zn > 2$) the excess Cu, which cannot form $Cu_2ZnSnSe_4$, will react to Cu_2SnSe_3. On the other hand if the Cu-supply is low ($Cu/Zn < 2$) there is excess Zn in the sample, which will form a ZnSe-phase. Therefore a change in the Cu-flux will change the ratios Zn/Sn and Cu/(Zn+Sn) which results in a position along the tie-line [35].

Micrographs of the sample surface and the cross section were taken in secondary electron configuration with a scintillator detector. The acceleration voltages used were 7 kV and 10 kV.

In the cross section view both the annealed and the not annealed samples do not exhibit any visible grain boundaries, independent of the exact growth conditions. This is shown exemplarily in figure 2.8.

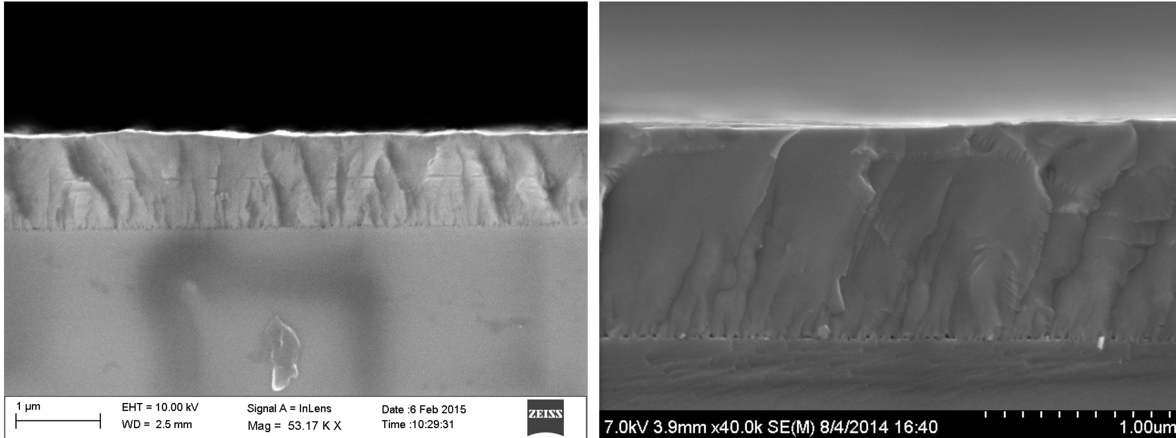

(a) Annealed sample.

(b) Not annealed.

Figure 2.8.: Cross section micrographs of one annealed and one not annealed sample. Both images do not exhibit visible grain boundaries. Note the different acceleration voltages. The micrograph of the annealed sample was taken by Shuyi Li at the University of Uppsala.

In the top view micrographs different morphologies can be observed. Some samples show a smooth surface without any visible grain boundaries but with a “hazy” layer on top. Figure 2.9 shows one example for each growth process.

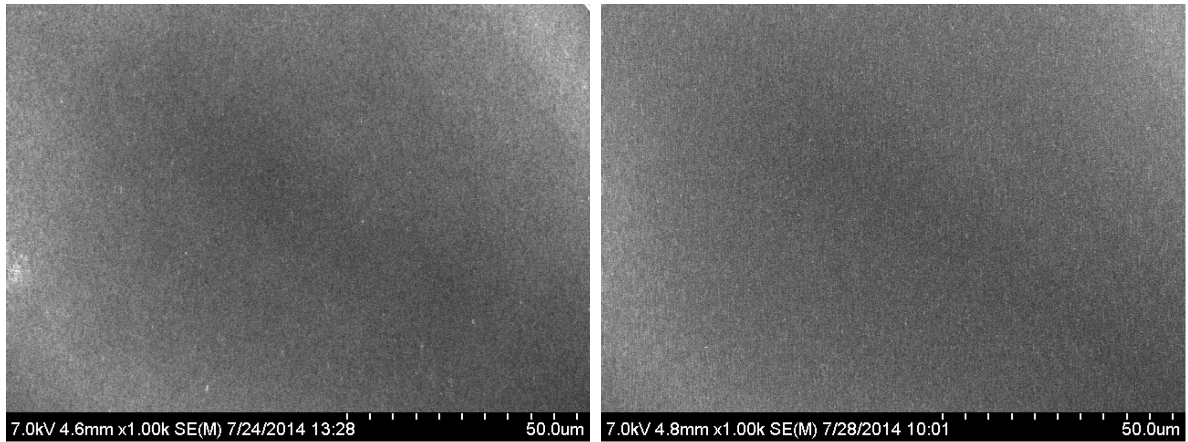

(a) Annealed sample. (b) Not annealed sample.

Figure 2.9.: Top view micrographs of one annealed and one not annealed sample. Both samples exhibit a smooth surface with a hazy layer on top.

Other samples exhibit an inhomogeneous surface as shown in figure 2.10. The sample shown in figure 2.8a has some apparently white areas on the surface. It has been shown that these areas are lowered with respect to the surrounding area and consist of ZnSe [42].

The top view in figure 2.8b shows that there is a structure of crystallites on the sample surface. Raman spectroscopy (see section 2.4.3) indicates that these crystallites contain copper selenide (CuSe) and ZnSe in addition to CZTSe.

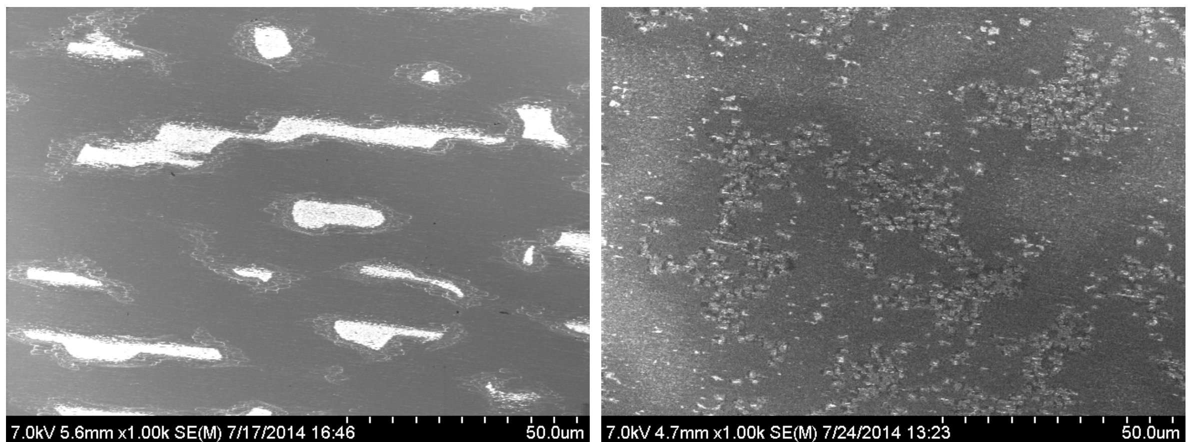

(a) Annealed sample with ZnSe patches on top. (b) Annealed sample with crystallites on the surface.

Figure 2.10.: Top view micrographs of samples with an inhomogeneous surface.

These surface inhomogeneities are only found in the annealed samples, which leads to the conclusion that they originate rather from the annealing stage than from the growth stage. However the occurrences of the inhomogeneous morphologies cannot be

correlated to particular process parameters like the flux of a certain source or the heater temperature. The reason for this is probably the fact that the heat transfer to the sample was random to a certain degree. This manifested itself in a visible change of the measured substrate temperature when the heater was kept at a constant temperature before the start of the growth process.

The sources also had an obvious influence on the substrate temperature, which was visible in form of an increase in the pyrometer reading as soon as the sources were opened at the beginning of the process. However this increase could not be correlated to the source temperatures.

Therefore the subsequent discussion is limited to the samples which showed a smooth surface in the micrographs, with the exception of the sample with the number 490, which is shown in figure 2.10b. For reference the metal ratios, as determined from the atomic percentages of the single elements, the substrate temperature T_{growth} at the beginning of the growth process and the increase of the heater temperature ΔT_{aneal} during the annealing stage of those samples are listed in table 2.1. The Se-content of these samples, which is not explicitly listed, was $52.5 - 53.3$ at.%. The table also states, if a piece of a sample was later treated with an ordering or a disordering procedure.

Table 2.1.: Compositions, as determined by EDX, substrate temperature before growth and temperature increase for the annealing stage of the samples, that are studied by spectroscopic ellipsometry and photoluminescence in the subsequent chapters.

Sample	Annealed	Cu/(Zn+Sn)	Zn/Sn	T_{growth} °C	ΔT_{aneal} °C	Treatment
486	yes	1.01	0.87	460	+50	-
487	yes	0.94	0.92	455	+50	ordered with proc. 1
490	yes	0.91	0.95	456	+60	-
497	yes	0.94	0.96	458	+40	-
499	no	0.91	0.89	458	-	ordered with proc. 1 and 2 disordered
503	no	0.91	0.94	454	-	-
506	no	0.91	0.96	452	-	-
508	no	0.85	1.03	452	-	-

2.4.2. X-ray Diffraction

The absence of visible grain boundaries is an indication for epitaxial growth of the samples, but not conclusive proof. A suitable tool to extract information about the crystal structure is X-ray diffraction (XRD).

The reflection of X-rays off a crystalline sample can be viewed as the reflection off the lattice planes, as shown in figure 2.11. The path difference between the reflected X-ray beams is then given as $2d_{\text{hkl}} \sin\theta$, where the angle of incidence θ is defined with respect to the lattice plane and d_{hkl} is the distance between two neighboring planes, which are

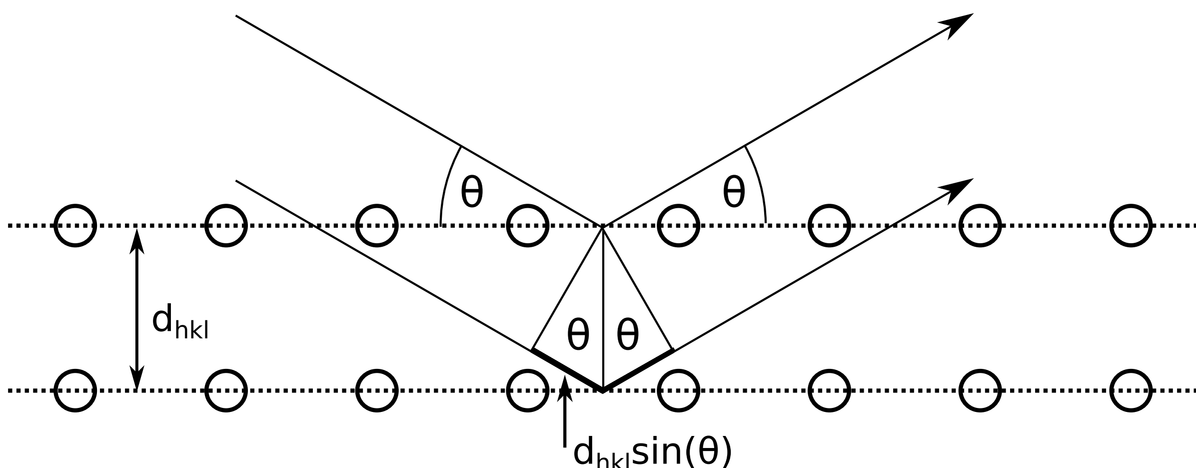

Figure 2.11.: Reflection of X-rays off two lattice planes described by the Miller indices h, k, l. The path difference between the two outgoing X-rays is $2d_{\text{hkl}} \sin\theta$.

defined by the Miller indices h, k and l. If this path difference is an integral multiple of the X-ray wavelength constructive interference of the outgoing beams occurs.

This behavior is described in Bragg's law, which relates the angle θ, at which constructive interference occurs, to the crystal structure (see for example [43]):

$$2d_{\text{hkl}} \sin\theta = n\lambda \tag{2.6}$$

Here λ is the X-ray wavelength and n is a positive integer.

An epitaxial sample, which is grown with one defined crystal orientation, contains only one set of Miller indices. Consequently it should only show X-ray reflections at angles corresponding to this set of indices and its multiples. Therefore measuring the angles, at which reflections occur, allows to draw conclusion about the crystal orientations, which are present in a sample.

In the present case the samples were grown on GaAs oriented in the [001]-direction, which means that only multiples of the (001)-reflection of CZTSe should be visible if the films are epitaxial. However, as was shown in section 2.2.1, CZTSe can grow with the c-axis parallel and perpendicular to the substrate surface. As a consequence of this also multiples of the (100)-reflection of CZTSe are possible.

The XRD measurements for this work were performed by Hiroki Kato on several annealed and not annealed samples of different compositions. The system, that was used, is equipped with a Cu X-ray source and a filter to remove the Cu Kβ line from the source. Therefore the X-rays consist mainly of Kα_1 and Kα_2 radiation. For the detection of the X-rays a NaI scintillation detector is used. The measurements of the samples were performed in θ-2θ scan mode.

Figure 2.12a depicts the X-ray diffractograms, normalized to the highest reflection, of two annealed and two not annealed samples of different compositions.

This plot shows that the samples qualitatively exhibit the same diffraction pattern, regardless of their composition and the growth process.

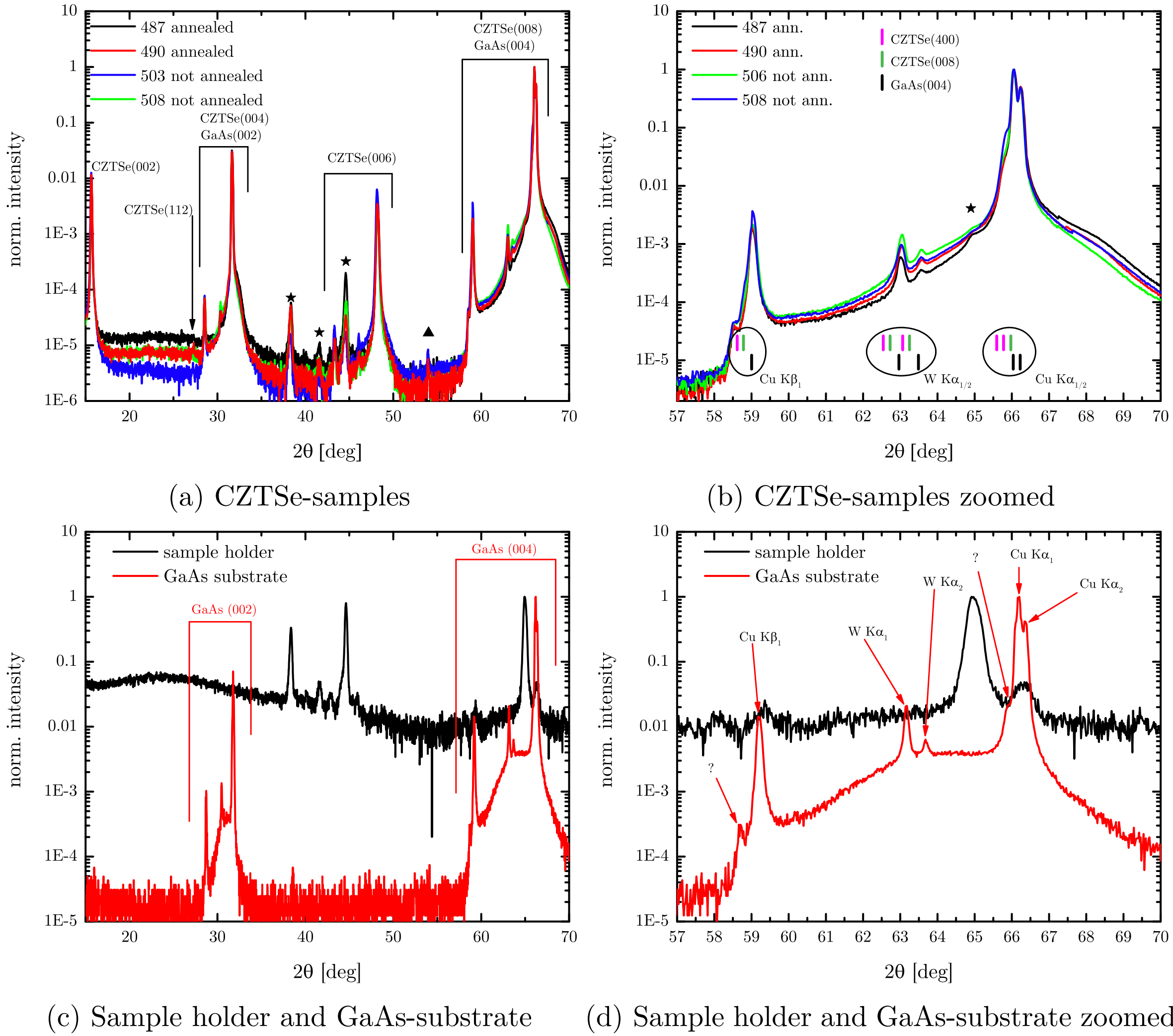

(a) CZTSe-samples

(b) CZTSe-samples zoomed

(c) Sample holder and GaAs-substrate

(d) Sample holder and GaAs-substrate zoomed

Figure 2.12.: X-ray diffraction patterns. Figure (a) shows two annealed and two not annealed samples with different compositions. The asterisks indicate reflections which are also visible in the diffractogram of the sample holder. The reflection labelled with the triangle might be an instrumental artifact. Figure (b) shows the magnification of the CZTSe(008) reflection. Figure (c) shows the diffraction patterns of the GaAs-substrate and the bare sample holder and figure (d) shows the magnification in the same scale as (b).

However, they also show a larger number of reflections than would be expected for epitaxially grown CZTSe, which are the (002), (004), (006) and (008)-reflection in the 2θ-range covered by this measurement [44].

In order to identify this variety of reflections the diffractogram of the sample holder was recorded (figure 2.12c). Clearly some of the reflections, that are observed in the CZTSe-samples, can be attributed to the sample holder. These reflections are labelled with an asterisk in figure 2.12a.

Figure 2.12c also shows the diffraction pattern of the bare GaAs-substrate. In this 2θ-range the (002) and the (004)-reflection of the GaAs should be visible [45].

But instead of the two Cu Kα-reflections [2] one can observe two patterns, which look similar to the ones seen in the CZTSe-samples. These patterns are actually the result of the reflection of X-rays with slightly different wavelengths off the same lattice planes. Therefore these patterns are bracketed together as GaAs(002) and GaAs(004).

To illustrate this figure 2.12d shows a zoom of the GaAs(004)-pattern. On this scale the Cu Kα_1 and the Cu Kα_2 line can be distinguished as the highest contribution. The two peaks at roughly $2\theta = 61.1\,^\circ$ and $2\theta = 61.7\,^\circ$ can be attributed to the W Kα_1 and the W Kα_2-line respectively. These lines are visible in the diffractogram, because the system is equipped with a tungsten filament, which leads to a tungsten contamination of the Cu-source. The peak at $2\theta = 59.2\,^\circ$ is due to the Cu Kβ_1-line, which is not completely removed despite the usage of a filter.

In addition to these lines there are two more peaks, labelled with ”?”. Their origin remains unclear but they are always visible, which makes them likely to originate from an impurity in the X-ray source.

From these considerations it can be concluded that for the most samples the diffraction patterns of the CZTSe-samples in figure 2.12a show only multiples of the (002)-reflection. In particular there is no significant signal at the position of the CZTSe (112)-reflection (indicated by the arrow), which has the highest intensity of all CZTSe-reflections.

Only sample 490 might have a small signal at the angle corresponding to the (112)-reflection. However, this sample showed some crystallites in the SEM top view, which might be the origin of this reflection (see figure 2.10b). Nonetheless, this sample is still highly oriented. This implies that the samples, which show a smooth surface in the SEM top view, are indeed epitaxial and do not contain any polycrystalline domains.

This leaves the reflection labelled with a triangle in figure 2.12a, which could not be attributed to a reflection of CZTSe or any other secondary phase that might be present in the sample. It is not visible in the reference measurements of the GaAs-substrate or the sample holder taken for this work. But it was previously observed in a GaAs-diffraction pattern recorded with the same machine [35]. It is therefore assumed that this reflection is an instrumental artifact.

Lastly figure 2.12b shows the magnification of the CZTSe (008) area. The bars indicate the expected positions for the GaAs (004), the CZTSe (008) and the CZTSe (400)-reflection for the different X-ray lines discussed in the previous paragraphs, taken from

[2] Actually two reflections are expected for each plane: the Cu Kα_1 and the Cu Kα_2-reflection. However, on the scale shown here they are too close together to be distinguishable.

[45] and [44]. The CZTSe (400)-reflections are listed here, because the unit cell can grow with the *c*-axis parallel to the substrate, as was discussed in section 2.2.1.

The reflections are at the positions, that correspond to GaAs. There are no peaks, which can exclusively be attributed to unstrained CZTSe by their position. This might imply that the CZTSe is strained throughout the whole thickness of the film.

However to draw a definitive conclusion from the peak position the data would need refining, which is beyond the scope of this work.

Nonetheless, it can be concluded from this discussion that both growth processes described in section 2.3.1 could successfully produce epitaxial samples without any visible grain boundaries.

2.4.3. Raman Spectroscopy

Raman spectroscopy is a suitable tool to study the phase composition of a sample. This measurement is based on the Raman effect, which describes the inelastic scattering of photons off matter. In the scattering process an incoming photon with the energy $\hbar\omega_\mathrm{i}$ is absorbed by an electron within the crystal. The absorption of the photon induces a polarization in the crystal, which oscillates with the frequency of the incoming photon. In the majority of the cases the polarization acts as a Hertzian dipole and emits a photon with the same energy as the photon, which was initially absorbed. This process is called Rayleigh scattering and is the dominating scattering process.

With a significantly lower probability Raman scattering can occur. In that case the polarization induced by the incoming photon is superimposed by the polarization, which is induced by a lattice vibration. Then it can be shown that the resulting polarization has additional components: one component, whose frequency is increased by the phonon energy (which is the quasiparticle of the lattice vibration) with respect to the initial photon frequency. The frequency of the other component is decreased by the phonon energy with respect to the initial photon energy. The former case corresponds to the annihilation of a phonon and is called Anti-Stokes scattering. The latter case, which corresponds to the creation of a phonon, is called Stokes scattering and is usually the component, that is measured in Raman spectroscopy [46]. The two different scattering mechanisms are depicted in figure 2.13.

The energy of the scattered photon can be expressed with respect to the energy of the incoming photon as:

$$\hbar\omega_\mathrm{f} = \hbar(\omega_\mathrm{i} \pm \Omega) \tag{2.7}$$

Here Ω denotes the phonon frequency. Since the phonon energy takes on discrete values, which are characteristic to each material, Raman scattering can be used to determine which phases are present in a sample.

It should be noted that the probability of Raman scattering is greatly increased if the energy of the incoming photon corresponds to an electronic transition of the material, that is studied. This *resonant Raman* scattering can be utilized to increase the detection

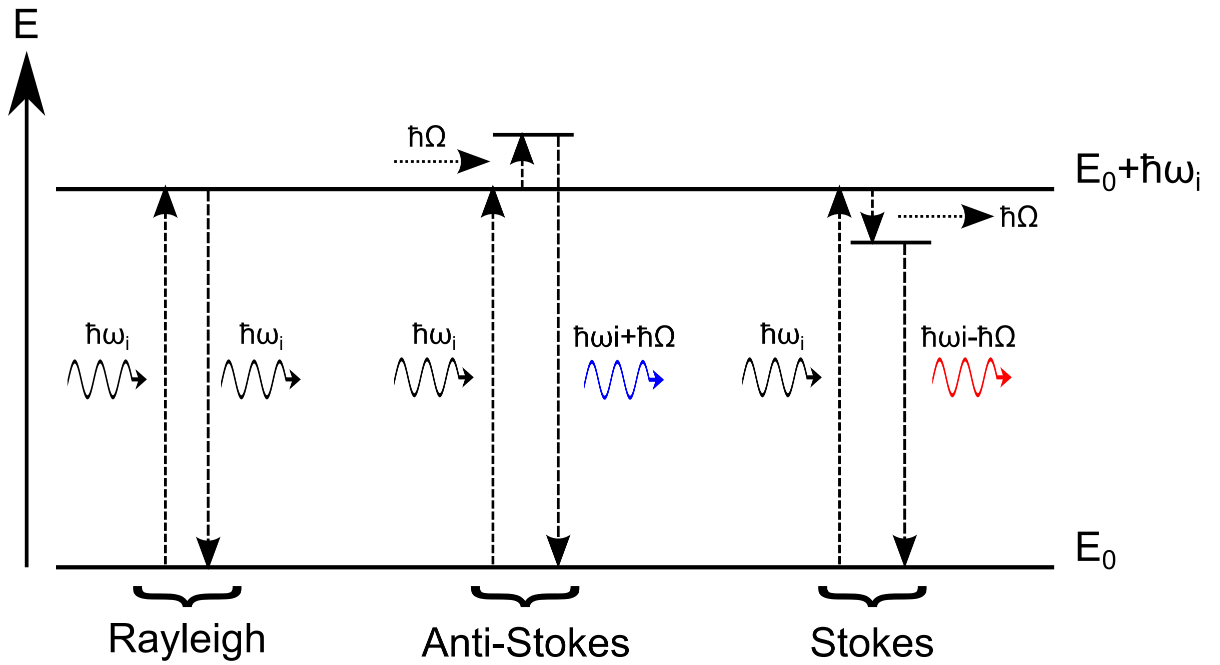

Figure 2.13.: Sketch of Rayleigh, Stokes and Anti-Stokes scattering. $\hbar\omega_{\mathrm{i}}$ denotes the photon energy and $\hbar\Omega$ is the phonon energy. In case of the Anti-Stokes scattering the energy of the outgoing photon is blue-shifted by the phonon energy. In case of the Stokes-scattering it is red-shifted by the phonon energy.

sensitivity for a certain phase by choosing an appropriate photon energy $\hbar\omega_\mathrm{i}$ [47].

The Raman spectroscopy in the present work was either performed with a home built setup at the University of Luxembourg or a commercial Raman microscope at the Luxembourg Institute of Science and Technology by Mads Weber.

The home built setup, which will be described in greater detail in chapter 4, uses the 514.5 nm and the 457.9 nm line of an argon-ion laser for the excitation of the sample and probes a spot of roughly 80 µm in diameter.

The commercial setup uses 532 nm and 442 nm laser lines and probes a spot of about 1 µm in diameter.

Several samples produced with the two different growth processes and varying compositions were screened by taking the Raman spectra with the two different excitation wavelengths, depending on the setup.

The shape of the resulting spectra correlates with the surface morphologies of the samples. Figure 2.14 shows the Raman spectra of the annealed sample 487 and the not annealed sample 503, which both showed a smooth surface in the SEM top view. Both samples were measured at two different spots using the 532 nm and the 442 nm laser line of the commercial setup. The intensity is plotted versus the Raman shift, which is the difference in inverse wavelength between the incoming and the scattered light, expressed in inverse centimeters. In this representation the ordinate values are independent of the excitation wavelength.

Figures 2.14a and 2.14b show the Raman spectra taken with the 532 nm laser line, normalized to the highest peak. In both cases all peaks can exclusively be attributed to CZTSe [48]. There is no visible signal from secondary phases. In case of the not annealed sample (figure 2.14b) the attribution of the peak at 250 cm^{-1} to CZTSe is not completely unambiguous because the mode of ZnSe, which is usually at 253 cm^{-1}[49], can be shifted towards lower wavenumbers due to strain or defective material and overlap with the CZTSe-signal in this region [50].

This ambiguity is resolved by the measurements with the 442 nm laser line, shown in figures 2.14c and 2.14d.

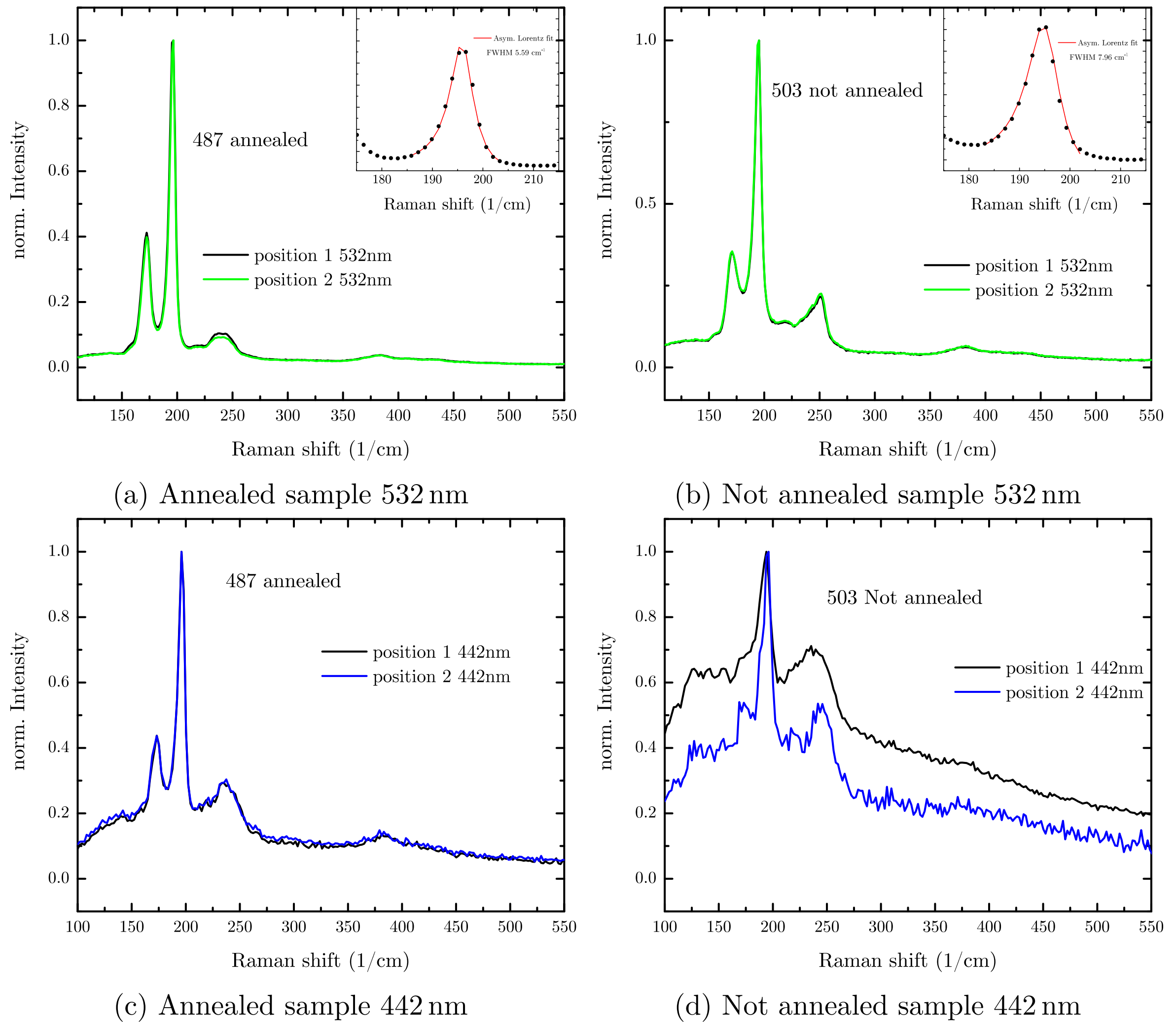

(a) Annealed sample 532 nm

(b) Not annealed sample 532 nm

(c) Annealed sample 442 nm

(d) Not annealed sample 442 nm

Figure 2.14.: Raman spectra of one annealed and one not annealed sample. Figure (a) and (b) each show spectra taken with an excitation wavelength of 532 nm at two different positions. Figure (c) and (d) show the spectra taken with an excitation wavelength of 442 nm at the same two positions.

Since this photon energy is close to the band gap of zinc selenide, which is roughly 2.8 eV [51], the Raman signal should be greatly enhanced due to resonance effects, as discussed above. The measurement does not show this clear enhancement at 253 cm^{-1} compared to the spectra taken with the 532 nm excitation. Furthermore a second order signal is expected for resonant Raman spectroscopy [52]. In the case of ZnSe this signal would be at 500 cm^{-1}, which is not visible in the spectra.

Comparing the Raman spectra of the annealed and the not annealed samples by fitting the highest Raman peak with an asymmetric Lorentzian function yields that this peak has a smaller full width at half maximum (FWHM) in the annealed sample. The fit is shown in the insets of the 532 nm spectra of figure 2.14. This leads to the conclusion that the annealing stage has a beneficial influence on the crystal quality.

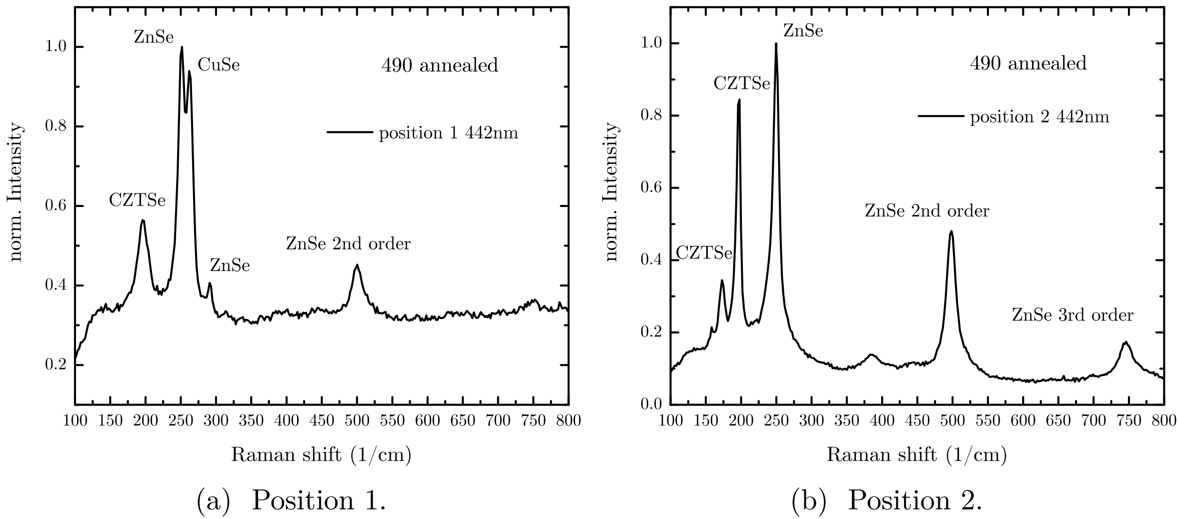

(a) Position 1.

(b) Position 2.

Figure 2.15.: Raman spectra taken on two points on a sample from figure 2.10b with an inhomogeneous surface morphology. Both spectra show a clear ZnSe signal at 250 cm^{-1} including second order and even third order in case of (b). The spectrum in (a) shows an additional CuSe-peak.

Figure 2.15 shows Raman spectra taken with the 442 nm-line on a sample with an inhomogeneous surface in the SEM top view. Both spots have a clear ZnSe-signal at 250 cm^{-1} and the second and, in case of figure 2.15b, even the third order is clearly visible. The spot in figure 2.15a shows an additional peak, which can be attributed to copper selenide (CuSe) [53].

In conclusion it was shown in this section that no secondary phases could be detected via Raman spectroscopy on the samples with a smooth surface according to SEM. It should however be emphasized that this does not preclude the existence of secondary phases in the bulk or at the substrate-interface, since Raman spectroscopy is a surface sensitive measurement technique.

2.4.4. X-ray Photoelectron Spectroscopy

For the correct analysis of the spectroscopic ellipsometry measurements (Chapter 3) it is essential to have as much information about the sample structure as possible. It is particularly crucial to have knowledge about any oxides that might have formed on the sample surface, since they can have a significant influence on the ellipsometric signal [54]. In principle the sample surface was already probed by Raman spectroscopy. However, if the amount of any phase on the surface is very small and it is not resonant with the exciting wavelength, then it might not give a detectable Raman signal. A more suitable tool to study the sample surface is X-ray photoelectron spectroscopy (XPS), which utilizes the photoelectric effect. During the measurement the sample is illuminated with X-rays with a sufficiently high energy to knock out electrons of their host atoms (Figure 2.16). The kinetic energy of the photoelectrons is then given by the difference between the photon energy $\hbar\omega$ and the electron's binding energy E_{B}, which is characteristic to each element. This makes it possible to determine the elemental constituents of the sample by measuring the emitted photoelectrons.

$$E_{\mathrm{kin}}^{\mathrm{e}} = \hbar\omega - E_{\mathrm{B}} \tag{2.8}$$

Furthermore the binding energy of the electrons depends not only on the element itself, but it also depends on the oxidation state of the atom. This means that the binding energies of one specific element in a chemical compound are generally different from it's elemental state. Therefore, XPS cannot only be used to determine the elemental constituents of a sample but also their oxidation state. This allows to draw conclusions about the chemical compound, in which they are present in the sample [55].

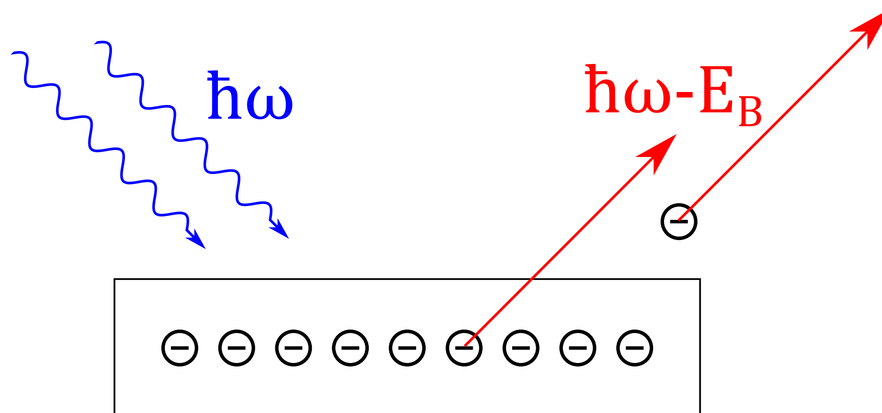

Figure 2.16.: Sketch of the photoelectric effect. The incoming photons with the energy $\hbar\omega$ cause the emission of photoelectrons from the sample. The kinetic energy of the photoelectrons is equal to the difference between the photon energy and the electron's binding energy E_{B}.

XPS measurements for this work were performed at the University of Uppsala with the help of Charlotte Platzer Björkman and Shuyi Li. The machine used was equipped with an Al Kα X-ray source. Survey scans, which probe a wide range of binding energies

with a low energy resolution, revealed a fundamental difference between annealed and not annealed samples.

(a) 487 annealed.

(b) 506 not annealed.

Figure 2.17.: XPS survey scans.

The survey scans of the annealed samples show mainly signals attributable to Zn, Cu, Se but very little Sn. Also observed are oxygen (O) and carbon (C), which are most likely present due to exposition of the samples to ambient atmosphere. An example is shown in figure 2.17a. The surface of the not annealed samples on the other hand exhibit mainly signals from Sn, Se, O and Cu, but not from Zn. This result is rather counter intuitive since the annealed samples were subjected to an additional annealing under a Sn- and Se-atmosphere, but they appear to have a Sn-depleted surface.

In addition to these surveys further scans were performed around the most prominent peaks from Cu, Zn and Sn with a higher energy resolution for one annealed and one not annealed sample. In case of the annealed sample 487 this yielded a binding energy of 1022.02 eV for the Zn $2p_3$ peak and 486.20 eV for the Sn $3d_{5/2}$ peak. For the not annealed

sample 506 it was found that the Sn $3d_{5/2}$ peak is at 486.77 eV, while there is no clear Zn signal. The respective plots are found in appendix A.1.

Table 2.2 lists the peak positions obtained from the detailed scans. The binding energy of Sn in the not annealed sample is in accordance with the binding energy of Sn in SnO_2 (tin oxide) [56]. On the other hand the binding energy of Zn in the annealed sample is in the range of binding energies for Zn in ZnO (zinc oxide) [55]. This indicates that the two different growth processes resulted in a different surface composition, and therefore in the formation of different oxide layers. On top of the annealed samples a ZnO layer and on top of the not annealed samples a SnO_2 layer has formed.

Table 2.2.: Maxima of the peaks obtained from the detailed scan around the most prominent emission energies for Cu, Zn, Sn and Se.

Sample	Annealed	$E(\mathrm{Cu2p_{3/2}})$	$E(\mathrm{Zn2p_3})$	$E(\mathrm{Sn3d_{5/2}})$	$E(\mathrm{Se3d_{5/2}})$
487	yes	932.19 eV	1022.02 eV	486.20 eV	54.50 eV
506	no	932.19 eV	not visible	486.77 eV	54.50 eV

2.4.5. Hall Measurements

Since the GaAs-substrates were undoped, it was possible to perform Hall measurements on the samples. For this work one of the annealed and one of the not annealed samples were studied with the van der Pauw method [57] by Florian Werner at the University of Luxembourg. For this a square piece of the sample with an edge length of approximately 5 mm was contacted with gold contacts on the corners as shown in figure 2.18. The sample was then placed in an magnetic field of up to 9 T perpendicular to the sample surface and an electric current was sent diagonally through the sample via two contacts. On the remaining two contacts the resulting Hall voltage was measured. By measuring the Hall voltage at varying magnetic fields it is possible to determine the sheet carrier density of the sample and thereby the overall carrier density.

In the present case, both samples were shown to be of p-type conductivity and the doping density could be estimated to be of the order of $N_\mathrm{p} = 10^{20}\,\mathrm{cm}^{-3}$. The effective density of the valence band states N_V can be estimated as [43]:

$$N_\mathrm{V} = 2\left(\frac{2\pi m_h^* k_\mathrm{B} T}{h^2}\right)^{\frac{3}{2}} \tag{2.9}$$

In this expression m_h^* is the effective hole mass. Persson calculated the effective hole and electron masses for CZTSe in the kesterite structure and found that the maximum value for the effective hole mass is $m_h^* = 0.33 m_0$, where m_0 is the rest mass of a free electron [27]. Inserting this value into equation 2.9 yields an effective density of states of $N_\mathrm{V} = 4.76\,10^{18}\mathrm{cm}^{-3}$ at 300 K, which is significantly lower than the doping density estimated by the Hall measurement. This indicates that the semiconductor is degenerate and that the Fermi-level lies below the valence band edge. This fact will be important for the interpretation of the photoluminescence measurements in chapter 4.

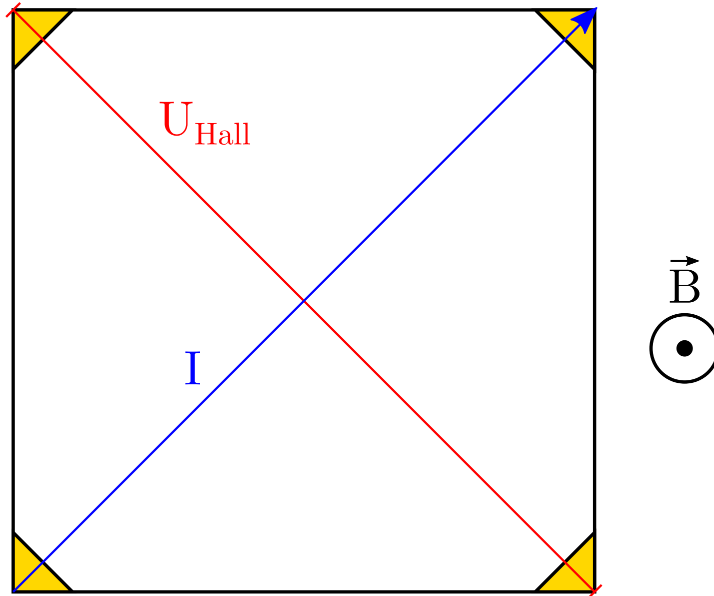

Figure 2.18.: Sketch of the measurement geometry used for the Hall measurements.

2.4.6. Conclusion

In this chapter it was shown that epitaxial CZTSe could be grown by molecular beam epitaxy by two different growth processes. The epitaxy of the samples was confirmed by the absence of visible grain boundaries in the SEM micrographs and by X-ray diffraction. Raman spectroscopy showed that both growth processes were able to produce samples without any detectable traces of secondary phases, which might be expected due to the sample position in the quasi-ternary diagram. It also showed that the in-situ annealing stage seemed to have a positive influence on the crystal quality. However, even though the samples are epitaxial and thereby suited to study the material properties without the influence of grain boundaries, Hall measurements indicate that they are most likely degenerate, which needs to be taken into account for the analysis of especially the photoluminescence measurements.

3. Spectroscopic Ellipsometry

In this chapter the spectroscopic ellipsometry measurements (SE) are presented. The first section describes the basic principle of SE. The second section deals with the measurement itself and the extraction of the dielectric function. The last sections contains the analysis of the dielectric functions and its discussion.

3.1. Principles of Ellipsometry

3.1.1. Polarization of Light

Since SE utilizes the polarization of light, this section is devoted to a summary of the polarization of light and its consequences for the interaction between light and matter.

A photon propagating in vacuum can be described as an electromagnetic wave satisfying the wave equation [58]:

$$\Delta \boldsymbol{E} = \frac{1}{c^2}\frac{\partial^2 \boldsymbol{E}}{\partial t^2} \tag{3.1}$$

Here $\boldsymbol{E}$ is the electric field vector and c is the speed of light. In vacuum it can be calculated from the vacuum permittivity ε_0 and the vacuum permeability constant μ_0 as $c = 1/\sqrt{\varepsilon_0\mu_0}$ [58]. If the photon propagates in matter, ε_0 and μ_0 need to be multiplied with the relative permittivity ε_r and the relative permeability μ_r. A solution for the wave equation 3.1 is a plane wave [58]

$$\boldsymbol{E}(\boldsymbol{r}, t) = \boldsymbol{E}_0 \exp\left[i(\boldsymbol{kr} - \omega t + \phi)\right] + \text{c.c.} \tag{3.2}$$

with the (in general complex) amplitude $\boldsymbol{E}_0$, the frequency ω, a phase ϕ and the wave vector $\boldsymbol{k}$. The wave vector points in the propagation direction of the wave and can be related to the wavelength λ as $|\boldsymbol{k}| = k = 2\pi/\lambda$. The abbreviation c.c. denotes the complex conjugate of the preceding expression and is usually skipped. However, it should be stressed that the electric field described by equation 3.2 is a real quantity. In case of a vanishing charge density the divergence of the electric field is zero, so $\nabla \cdot \boldsymbol{E} = 0$. Inserting the solution 3.2 into this expression yields $\boldsymbol{E} \cdot \boldsymbol{k} = 0$, which means that the component of the electric field pointing in the propagation direction of the wave is always zero. Consequently, the plane wave of equation 3.2 is a transverse wave. The magnetic field of the electromagnetic wave can be calculated from the negative curl of the electric field, resulting in [58]:

$$\boldsymbol{B} = \frac{1}{\omega}\left(\boldsymbol{k} \times \boldsymbol{E}\right) \tag{3.3}$$

In vacuum and in non-absorbing materials the magnetic field is oscillating perpendicular, but in phase, with respect to the electric field and also perpendicular to the propagation direction of the electromagnetic wave. Its strength is given by [58]:

$$|\boldsymbol{B}| = \frac{1}{c}|\boldsymbol{E}| \tag{3.4}$$

The interaction of electromagnetic waves with matter is mainly determined by the motion of electric charges, as electrons or atomic nuclei, which is induced by the wave's electric field. The magnetization, which is induced by the wave's magnetic field, can usually be neglected, since the the response of the magnetic momenta of electrons and nuclei is usually too slow to follow the oscillations of the magnetic field [59]. Therefore the description of an electromagnetic wave can be limited to the description of the electric component.

The term polarization describes the orientation of the electric field vector of an electromagnetic wave with respect to the propagation direction of the wave. The emission of photons from most naturally occurring sources of electromagnetic radiation is a statistical process. This means that the direction of the vector $\boldsymbol{E}_0$ and the phase ϕ generally are random for each photon. As a consequence the electric field vector of the radiation emitted by such a source, which is the superposition of the single electromagnetic waves, does not have a defined orientation. It is called unpolarized. On the other hand, if the radiation is polarized, the electric field vector has one defined orientation. It can conveniently be described by the Jones vector $\boldsymbol{J}$. An electromagnetic wave propagating in the z-direction can then be expressed as [58]:

$$\boldsymbol{E}(z,t) = \begin{pmatrix} E_\mathrm{p} e^{i\phi_\mathrm{p}} \\ E_\mathrm{s} e^{i\phi_\mathrm{s}} \\ 0 \end{pmatrix} \exp\left[i(kz - \omega t)\right] \equiv \boldsymbol{J} \exp\left[i(kz - \omega t)\right] \tag{3.5}$$

In this representation the electric field is split up into two components, which are perpendicular to each other, while the component in propagation direction is zero. In the discussion of the polarization of electromagnetic waves the latter is usually skipped. The choice for the two remaining coordinates is basically arbitrary. In experimental set-ups, studying reflection or refraction, they are usually defined by the plane of incidence (POI). The POI is spanned by the propagation vector $\boldsymbol{k}$ and the surface normal of the probed sample. E_p is the component parallel to the POI and E_s is the component perpendicular (s is derived from the German word *senkrecht* for perpendicular) to the POI. Both components have a phase given by ϕ_p and ϕ_s respectively, which are in general different from each other. The complete information about the polarization is contained in $\boldsymbol{J}$.

In the simplest case the phase difference $\Delta\phi = \phi_\mathrm{p} - \phi_\mathrm{s}$ between the two components is zero. Then the resulting electric field vector $\boldsymbol{E}$ always points in the same direction. This is called linear polarization. If $E_\mathrm{p} = E_\mathrm{s}$ and $\Delta\phi = \pm\pi/2$, the electric field $\boldsymbol{E}$ follows a helical trajectory. Since the projection of the trajectory onto a plane perpendicular to the propagation direction describes a circle, this is called circular polarization. The

most general form of polarization is the elliptical one. It occurs when $\Delta\phi = \pm\pi/2$ and $E_\mathrm{p} \neq E_\mathrm{s}$ or when $0 < \Delta\phi \neq \pm\pi/2$ for arbitrary values of E_p and E_s. In this case the projection of $\boldsymbol{E}$ has an elliptical shape. These three types of polarization are shown in figure 3.1, together with a possible Jones vector $\boldsymbol{J}$ describing them.

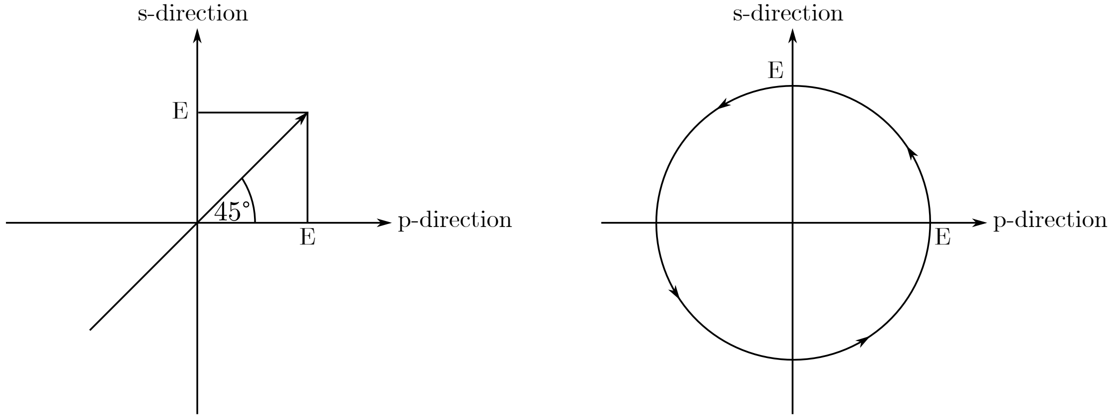

(a) Linear polarization. $\boldsymbol{J}_\mathrm{lin} = \frac{E}{\sqrt{2}}\begin{pmatrix}1 & 1\end{pmatrix}^\mathrm{T}$ (b) Circular polarization. $\boldsymbol{J}_\mathrm{circ} = \frac{E}{\sqrt{2}}\begin{pmatrix}1 & -i\end{pmatrix}^\mathrm{T}$

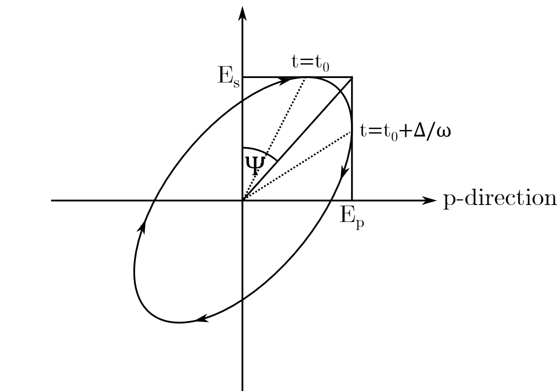

(c) Elliptical polarization.
$\boldsymbol{J}_\mathrm{circ} = \begin{pmatrix}\sin(\psi)\exp(i\Delta) & \cos(\psi)\end{pmatrix}^\mathrm{T}$,
with $\tan(\psi) = E_\mathrm{p}/E_\mathrm{s}$

Figure 3.1.: The three different polarization states with one possible Jones vector $\boldsymbol{J}$. Adapted from [59].

3.1.2. The Ellipsometric Parameters

When an electromagnetic wave, propagating in vacuum or a medium, hits the interface to a different medium, a part of the wave is reflected, while the other part is transmitted and continues propagating in the second medium. The amplitudes of the reflected and the transmitted wave can be calculated by using the Fresnel equations. The Fresnel equations describing the reflectance $\mathcal{R}$ of an electromagnetic wave propagating in vacuum

and impinging on a sample are [46]

$$\mathcal{R}_\mathrm{p} = |\tilde{r}_\mathrm{p}|^2 = \left| \frac{\tilde{n}^2 \cos\alpha - (\tilde{n}^2 - \sin^2\alpha)^{1/2}}{\tilde{n}^2 \cos\alpha + (\tilde{n}^2 - \sin^2\alpha)^{1/2}} \right|^2 \tag{3.6}$$

for the p-polarized component and

$$\mathcal{R}_\mathrm{s} = |\tilde{r}_\mathrm{s}|^2 = \left| \frac{\cos\alpha - (\tilde{n}^2 - \sin^2\alpha)^{1/2}}{\cos\alpha + (\tilde{n}^2 - \sin^2\alpha)^{1/2}} \right|^2 \tag{3.7}$$

for the s-polarized component. Here α is the angle of incidence, defined with respect to the surface normal, and $\tilde{n}$ is the complex refractive index of the sample. It can be defined as [60]:

$$\tilde{n}(\omega) = n(\omega) + i\kappa(\omega) \tag{3.8}$$

Here the real part n is usually referred to as the refractive index, which describes the speed of light in the corresponding medium with respect to the vacuum speed of light. The imaginary part κ is the attenuation coefficient describing the absorption within an absorbing medium. In general, both n and κ, and hence also $\tilde{n}$, depend on the frequency of the electromagnetic wave. The complex reflectivity $\tilde{r}$ is the ratio of the corresponding component of the Jones vector for the incoming (i) and the reflected (r) wave:

$$\tilde{r}_\mathrm{p/s} \equiv \frac{\tilde{E}^\mathrm{(r)}_\mathrm{p/s}}{\tilde{E}^\mathrm{(i)}_\mathrm{p/s}} \equiv \frac{E^\mathrm{(r)}_\mathrm{p/s} \exp(i\phi^\mathrm{(r)}_\mathrm{p/s})}{E^\mathrm{(i)}_\mathrm{p/s} \exp(i\phi^\mathrm{(i)}_\mathrm{p/s})} \tag{3.9}$$

As can be seen from equations 3.6 and 3.7, the behavior of the reflections depends on the polarization state of the wave, meaning that the amplitudes of E_p and E_s (see equation 3.5) change in different ways. Furthermore, a phase change occurs at the interface, which is also different for the p- and the s-polarized component. Mathematically the polarization change corresponds to the multiplication of the Jones vector with a Jones matrix, which transforms $\boldsymbol{J}$ into the new polarization state. As a result of the different behaviors of the two components, the polarization of an electromagnetic wave changes upon reflection off an interface. The change in polarization is the measured variable in ellipsometry in order to obtain information about $\tilde{n}$ of the sample. The name ellipsometry derives from the fact that the reflected electromagnetic radiation is usually elliptically polarized, which is the most general polarization state.

As was shown in the previous section, the information about the polarization state is contained in the Jones vector $\boldsymbol{J}$ of equation 3.5. Since the polarization only describes the direction of the electric field, but not the intensity of the wave (which is proportional to $|\boldsymbol{E}|^2$), the absolute values of E_p and E_s are not important. Only their ratio influences the direction of $\boldsymbol{E}$. Likewise, the absolute phase values ϕ_p and ϕ_s do not matter for the polarization but only the phase difference $\Delta\phi$. Therefore the polarization state is fully described by two real parameters, in this case the ratio of the amplitudes and the phase difference. In a similar way the change of polarization measured in ellipsometry is usually expressed in terms of the two ellipsometric parameters ψ and Δ [59]:

$$\tan\psi \exp(i\Delta) = \frac{\tilde{r}_\mathrm{p}}{\tilde{r}_\mathrm{s}} \tag{3.10}$$

Inserting the definition of the reflectivity $\tilde{r}$ from equation 3.9 and calculating the ratio shows that $\tan(\psi)$ can be identified with the change of the ratio of the p-polarized to the s-polarized component. The exponential function $\exp(i\Delta)$ describes the change in the phase difference between the p-polarized and the s-polarized component.

3.1.3. Dielectric Function and Joint Density of States

By measuring the polarization change of electromagnetic radiation upon reflection off a sample, ellipsometry is a suitable tool to determine the complex refractive index $\tilde{n}$ of the sample. Another way to express the refractive index is in terms of the complex dielectric function $\tilde{\varepsilon}$ [58]:

$$\tilde{n}(\omega)^2 = \tilde{\varepsilon}(\omega) = \varepsilon_1(\omega) + i\varepsilon_2(\omega) \tag{3.11}$$

In general the dielectric function describes the response, which is given by the electric displacement field $\boldsymbol{D}$, of a medium to an external electric field $\boldsymbol{E}$ [58]:

$$\boldsymbol{D} = \tilde{\varepsilon}\varepsilon_0\boldsymbol{E} \tag{3.12}$$

Here ε_0 is the (real) vacuum permittivity. The dielectric function in this expression needs to be complex, because the medium always needs a finite time to respond to the external field. If the fields are variable in time, this introduces a phase shift between $\boldsymbol{E}$ and $\boldsymbol{D}$, which is taken into account by the complexity of $\tilde{\varepsilon}$. Similar to the complex refractive index, the imaginary part ε_2 describes the absorption of radiation in the medium. The real and the imaginary part of $\tilde{\varepsilon}$ are related via the Kramers-Kronig relations [46]:

$$\varepsilon_1(\omega) - 1 = \frac{2}{\pi}\mathcal{P}\int_0^\infty \frac{\omega'\varepsilon_2(\omega')d\omega'}{\omega'^2 - \omega^2} \tag{3.13}$$

and

$$\varepsilon_2(\omega) = -\frac{2\omega}{\pi}\mathcal{P}\int_0^\infty \frac{\varepsilon_1(\omega')d\omega'}{\omega'^2 - \omega^2} \tag{3.14}$$

Unlike the attenuation coefficient κ, it can be directly linked to the electronic structure of the material. Yu and Cardona derived $\tilde{\varepsilon}$ for a semiconductor by calculating the probability of the transition of an electron from the valence band into the conduction band in the presence of electromagnetic radiation [46]. They showed that $\tilde{\varepsilon}$ is proportional to the joint density of states (JDOS) $D_\mathrm{j}(E_\mathrm{cv})$. The JDOS is the density of *pairs of states*, which are separated by the energy $E_\mathrm{cv} = E_\mathrm{c} - E_\mathrm{v}$, where $E_\mathrm{c/v}$ describe the corresponding states in the conduction- or valence band respectively. The JDOS can be calculated as [46]:

$$D_\mathrm{j}(E_\mathrm{cv}) = \frac{1}{4\pi^3}\int \frac{dS_{\boldsymbol{k}}}{|\nabla_{\boldsymbol{k}}(E_\mathrm{cv})|} \tag{3.15}$$

The integration is performed over the constant energy surface $S_{\boldsymbol{k}}$, which is the entirety of all wavevectors $\boldsymbol{k}$ with $E_\mathrm{cv}(\boldsymbol{k}) = \mathrm{const.}$ From this expression it can be seen that the JDOS has singularities at the points, where $\nabla_{\boldsymbol{k}}(E_\mathrm{cv})$ vanishes. It was found by Van

Hove that these correspond to critical points in the band structure, which are called Van Hove singularities [61]. Figure 3.2 shows an artificial three-dimensional band structure and the corresponding JDOS of a direct semiconductor with a simple cubic lattice. In the case of the simple cubic lattice, the Γ-point denotes the center of the Brillouin zone. The X-point is at the center of a face, the M-point is at the center of an edge and the L-point is at the corner. The band structure has its interband minimum at the Γ-point, its interband maximum at the L-point and saddle points at the X- and M-point. At the energies, which correspond to the difference between the two bands in figure 3.2a at those critical points, the JDOS shows singularities, i.e. is not differentiable [46].

Both parts ε_1 and ε_2 are related to the JDOS [46]:

$$\varepsilon_{1/2} \propto D_{\mathrm{j}}(E_{\mathrm{cv}}) \tag{3.16}$$

As a consequence of this, the Van Hove singularities are also reflected in the dielectric function. Therefore, it is possible to draw conclusions about the position of the critical points in the JDOS from an analysis of the dielectric function. This critical point analysis of the dielectric function will be discussed in greater detail in section 3.3.

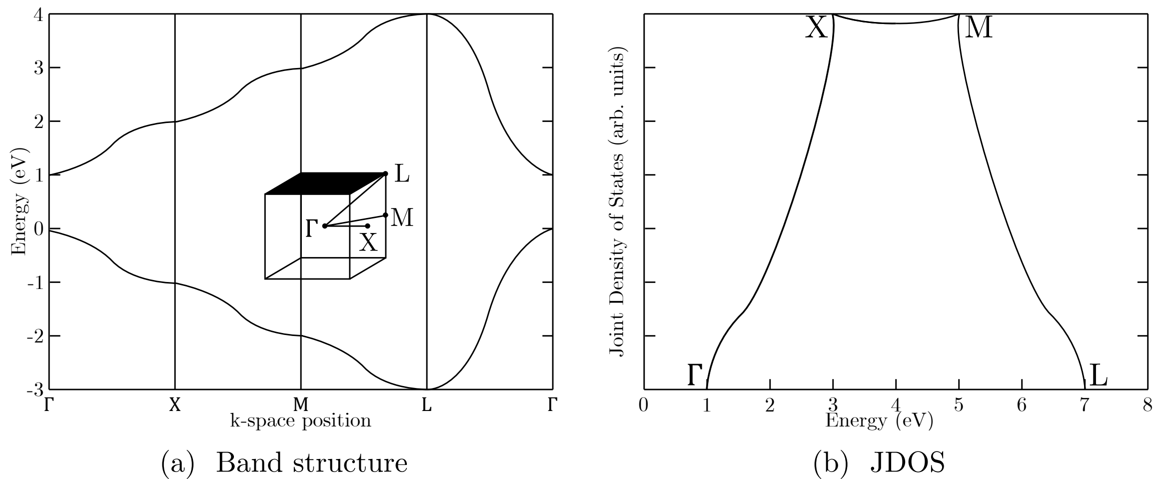

(a) Band structure (b) JDOS

Figure 3.2.: Artificial three-dimensional band structure and the corresponding JDOS. The JDOS has singularities at those energies, where the band structure has prominent features, like an interband minimum or maximum. The inset in 3.2a shows the Brillouin zone of the simple cubic unit cell. Adapted from [62].

3.2. Ellipsometry Measurements

3.2.1. Variable Angle Spectroscopic Ellipsometry

To obtain the dielectric function of the epitaxial CZTSe films in this work, they were measured by variable angle spectroscopic ellipsometry (VASE). The machine used was

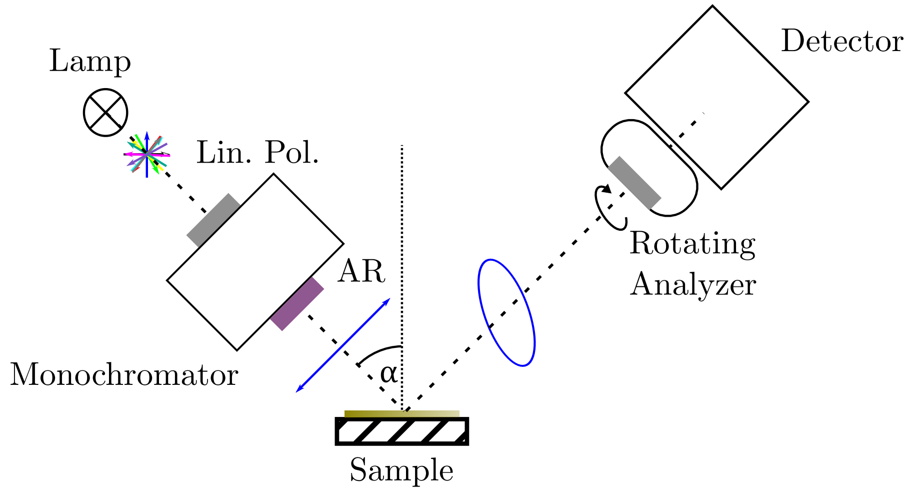

Figure 3.3.: Sketch of the VASE setup.

a commercial VASE setup. A sketch of the setup is shown in figure 3.3. It contains a light source, which produces polychromatic unpolarized light. The light then passes through a combination of a linear polarizer and a monochromator. The linear polarizer allows light of one specific polarization to pass. It is oriented in such a way, that the passing light has both a p- and a s-polarized component. The monochromator selects a specific wavelength. Then the, now monochromatic and linearly polarized, light is reflected off the sample and attains an elliptic polarization state. The reflected light is passed through a rotating analyzer, which is a continuously rotating polarization filter. By measuring the passing light intensity as a function of the orientation of the rotating analyzer with a detector, the polarization ellipse is tracked. Comparing the polarization states before and after the reflection off the sample yields the ellipsometric parameters ψ and Δ. Depending on the sample, it might happen that the reflected light is almost linearly polarized, in which case it is not possible to accurately determine ψ and Δ. To avoid this situation, the setup is additionally equipped with an auto retarder (AR), located behind the monochromator. The AR is a rotatable compensator, which can change the polarization direction of the incoming light by up to $90\,°$. It is automatically adjusted such, that the ellipsometric parameters can be measured with the highest accuracy possible.

The sample mount and the arm holding the rotating analyzer are rotatable. This allows varying the angle of incidence α. A variable angle is desirable because the uncertainty of the dielectric function is minimized near the pseudo Brewster angle, which is defined by $\Delta = 90\,°$. For semiconductors this is usually the case for angles of incidence of around $\alpha = 75\,°$ [63].

In this work three different angles of incidence were used for each sample, $65\,°$, $70\,°$ and $75\,°$. At each angle the wavelength range from 300 nm to 1700 nm was covered with a step size of 10 nm.

3.2.2. Modelling of the Absorber Layers

Figure 3.4 shows the set of ellipsometric parameters ψ and Δ, plotted versus the photon energy, measured at the three angles of incidence for one epitaxial sample.

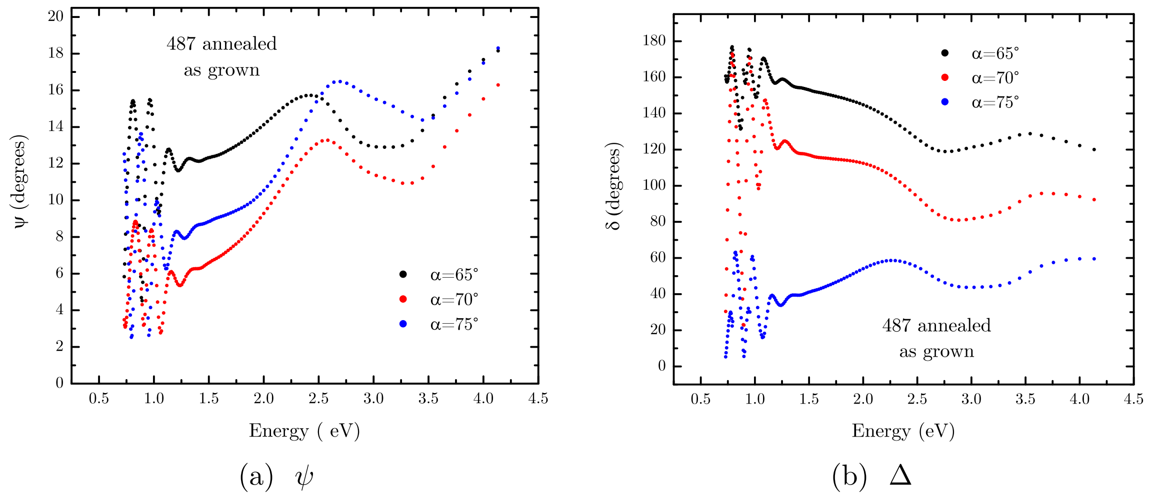

(a) ψ (b) Δ

Figure 3.4.: Measured ellipsometric parameters for the annealed, as grown sample 487.

The first step in the interpretation of these measurements is the conversion of the not directly physically significant ellipsometric parameters into a quantity, which is characteristic to the sample. It was shown in section 3.1.2 that ψ and Δ are related to the complex refractive index $\tilde{n}$ by the Fresnel equations 3.6 and 3.7. However, these equations are derived for a single interface between two media. Both ellipsometric parameters show oscillations for the low photon energies. These are interferences of the light reflected at the sample surface and the light reflected at the substrate-film interface. They are visible because the CZTSe-films are not fully absorbing in this energy range. This interface induces another change in the polarization, in addition to the interface between the ambient and the sample surface. Furthermore, it was shown by the XPS measurements (section 2.4.4) that the samples have a ZnO or a SnO_2 layer on the surface. It can also be assumed that an oxide layer formed on top of the GaAs-substrates, since they were exposed to air before the growth process. These oxide layers result in additional interfaces, which themselves induce a change in the polarization. This means that the measured ellipsometric parameters are influenced by all refractive indices of the different materials. Therefore a simple inversion of the Fresnel equations is not possible.

To disentangle the different layers and determine the properties of the CZTSe-layer, it is necessary to construct a model describing the complete sample and then fit it to the experimental data [64]. For this purpose the WVASE software by the company J.A. Woollam was used. It allows the modelling of complex samples consisting of different layers with different optical properties. The model can be fitted to a VASE measurement by adjusting the desired parameters, like thickness or dielectric function, of the different layers and minimising the mean-squared error (MSE) [54], using a Levenberg-Marquardt

algorithm [65]:

$$MSE = \sqrt{\frac{1}{2N-M}\sum_{i=1}^{N}\left[\left(\frac{\psi_i^{\mathrm{mod}}-\psi_i^{\mathrm{exp}}}{\sigma_{\psi,i}^{\mathrm{exp}}}\right)^2+\left(\frac{\Delta_i^{\mathrm{mod}}-\Delta_i^{\mathrm{exp}}}{\sigma_{\Delta,i}^{\mathrm{exp}}}\right)^2\right]} \tag{3.17}$$

Here N is number of measurement points, in this case the different photon energies, at which a (ψ, Δ) pair was obtained, M is the number of variable parameters in the model, $(\psi_i^{\mathrm{exp}}, \Delta_i^{\mathrm{exp}})$ are the measured ellipsometric parameters and σ_i^{exp} is the standard deviation of the respective ellipsometric parameter, as it was determined by the measurement routine. The pairs $(\psi_i^{\mathrm{mod}}, \Delta_i^{\mathrm{mod}})$ are calculated from the model parameters. Details about this conversion of the optical properties of a complex sample into ellipsometric parameters can be found in [64] and [54].

The layer structure of the model used to describe the epitaxial samples in this work is shown in figure 3.5. It consists of four or five layers: The GaAs-substrate, the GaAs-oxide

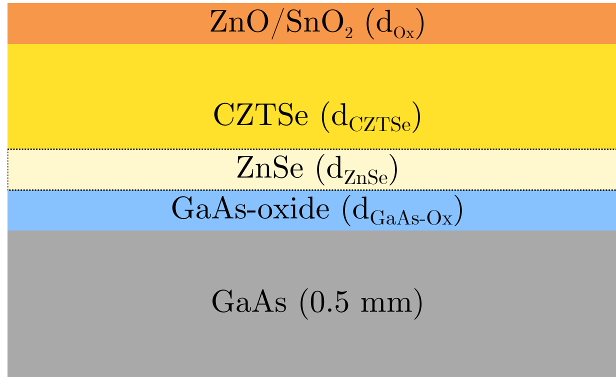

Figure 3.5.: Layer structure of the model, which was fitted to the ellipsometric data. The ZnO layer was used for the annealed samples, the SnO layer for the not annealed samples.

layer, the CZTSe-layer and the surface oxide layer. Based on the XPS measurements, the surface layer was set as ZnO for the annealed samples and as SnO_2 for the not annealed samples. The inclusion of these surface oxide layers was of particular importance, because the fitting of the model to the data was not possible without them. Additionally, a slightly modified model, with a ZnSe- below the CZTSe-layer, was used. This layer was included because Redinger et al. found that in the initial stage of the co-evaporation of CZTSe at first a ZnSe-layer is formed [66]. Since their process is similar to the processes used in this work, the inclusion of this layer is justified, even though it was not directly detected.

During the fitting of the model to the experimental data the thickness of the GaAs-substrate was kept constant at 0.5 mm, according to the specifications provided by the supplier. The thicknesses of the other layers were allowed to vary within certain boundaries:

To estimate the thickness of the oxide layer on the substrate, a VASE measurement was performed on a bare piece of GaAs, that had been exposed to air. A model consisting of

a GaAs-substrate with a fixed thickness of 0.5 mm, as was specified by the supplier, with a GaAs-oxide layer was fitted to the data. The dielectric functions of GaAs and GaAs-oxide were taken from the default materials library, which was supplied together with the WVASE software by J.A. Woollam. The dielectric function for the GaAs-oxide was based on a model dielectric function for native oxides on compound semiconductors, derived by Zollner [67]. The exact type of oxide was not specified. The dielectric functions of both GaAs and its oxide layer were kept fixed during the fit. The only free parameter was the thickness of the GaAs-oxide. The fit, shown in figure 3.6, resulted in a thickness of 2.7 nm for the oxide-layer with a MSE of 5.9, which indicates a very good agreement between the model and the experimental data. This is in accordance with the findings of Torkhov et al., who found an oxide thickness, consisting of a mixture of Ga_2O_3 and As_2O_3, of approximately 3 nm on epitaxial GaAs under normal conditions [68]. Therefore the best-fit thickness of the GaAs-oxide layer in the complete stack was constrained to not significantly exceed 3 nm.

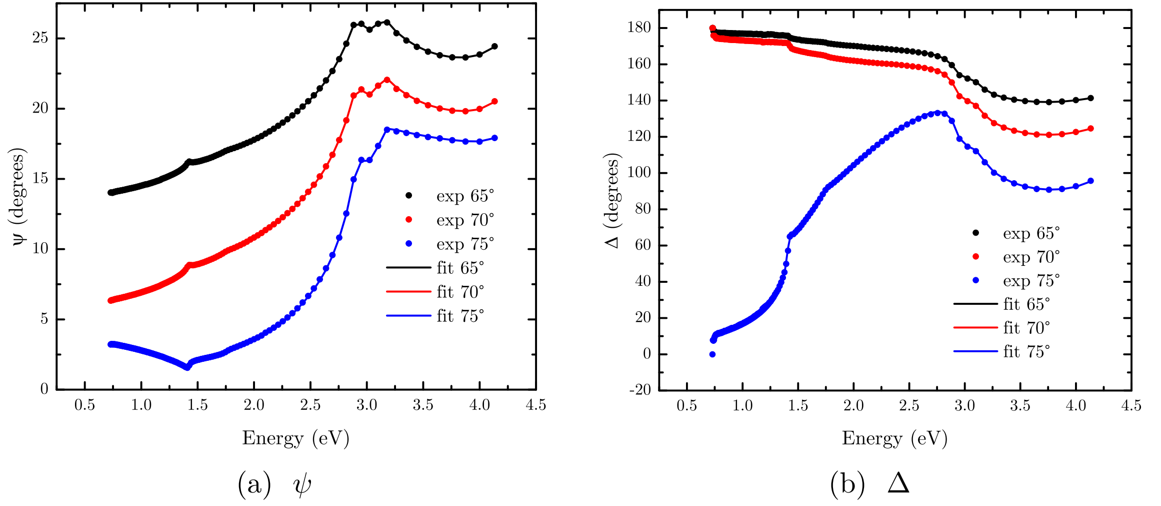

(a) ψ (b) Δ

Figure 3.6.: Fits of the ellipsometric parameters of the bare GaAs-substrate.

If the ZnSe-layer was included, its thickness was determined by the best fit to the experimental data. This resulted in thicknesses of $10 - 20$ nm for this layer, which is considerably thinner than the thickness observed by Redinger et al. [66]. They observed ZnSe in distances of up to 300 nm from the substrate. However, in their case the ZnSe grew in form of blocks and not as a continuous layer. For the epitaxial samples, there was no information about the shape of the potential ZnSe inclusion. Since it was modeled as a continuous, flat layer in this work, it should be regarded as an effective layer. If this continuous layer was to describe an inhomogeneous structure, as found by Redinger et al., it can be assumed that its thickness can be smaller than the height of the ZnSe columns. Therefore no additional constraints were made regarding the thickness of this layer.

The thickness of the CZTSe-layer combined with the thickness of the surface oxide or, in the cases with the additional ZnSe-layer, the thickness of the CZTSe- and the ZnSe-

layer combined with the thickness of the surface oxide was required to be compatible with the thickness determined from the SEM cross sections within ±30 nm. Within the scope of this work, no measurement was performed, which could give an accurate estimation of thickness of the surface oxide layer. Therefore the constraints for the oxide layer thickness needed to be estimated by other means. It was found by Zuo et al. that the native ZnO-layer, which forms on polycrystalline Zn, can have thicknesses of up to more than 10 nm [69]. Based on their measurements, the thickness of the ZnO-layer was kept variable, but the fit was discarded, if the best-fit thickness significantly exceeded 10 nm. For the tin oxide layer a similar procedure was used.

The dielectric functions of all layers, except for the CZTSe-layer, were taken from the default materials library, which was supplied together with the WVASE software by J.A. Woollam. They were set as constant during the fitting. The dielectric function of the CZTSe-layer was modelled using several oscillators. An oscillator is a complex function of the energy, whose real and imaginary part need to satisfy the Kramers-Kronig relations 3.13 and 3.14 in order to potentially describe a dielectric function [54]. The term oscillator is derived from the fact, that $\tilde{\varepsilon}$ can be expressed as a sum of classical, charged, harmonic oscillators, see for example [46]. The oscillators used for the CZTSe-layers were of the parametric semiconductor model (PSEMI) type. The PSEMI oscillator was developed at J.A. Woollam to especially describe the dielectric function of semiconductors. It consists of four polynomial spline functions, which are controlled by seven variable parameters. More details and a mathematical description of the PSEMI oscillator can be found in [54]. To describe one CZTSe-layer, three PSEMI oscillators were used and all seven parameters of each oscillator were set as variable.

In summary only the dielectric function of the CZTSe-layers and, within reasonable boundaries, the thicknesses of all layers, with the exception of the GaAs substrate, were free parameters during the fit. An overview of the fitting parameters is given in table 3.1. In this way, the fit allows the determination of $\tilde{\varepsilon}$ of the CZTSe-layer.

Table 3.1.: Summary of the fit parameters in the model, which was used to fit the ellipsometric data.

Layer	Thickness	Dielectric function
GaAs	fixed to 0.5 mm	from database, fixed
GaAs-oxide	variable, upper limit 3 nm	from database, fixed
ZnSe	free	from database, fixed
CZTSe	variable, constrained by SEM thickness	3 PSEMI oscillators with 21 free parameters
ZnO	variable, not significantly thicker than 10 nm	from database, fixed
SnO_2	variable, not significantly thicker than 10 nm	from database, fixed

3.3. Critical Point Analysis

In this section the dielectric functions of the CZTSe-layers of those samples, which could be fitted using the models described in the previous section with reasonable thicknesses, will be analyzed. Apart from a good agreement between the model and the data, the extracted dielectric functions should be physically meaningful as well. To check, whether the dielectric functions are physical, figure 3.7 shows a zoom on the region of the onset of ε_2. From this plot, it can be seen that not all curves decrease to zero at low energies.

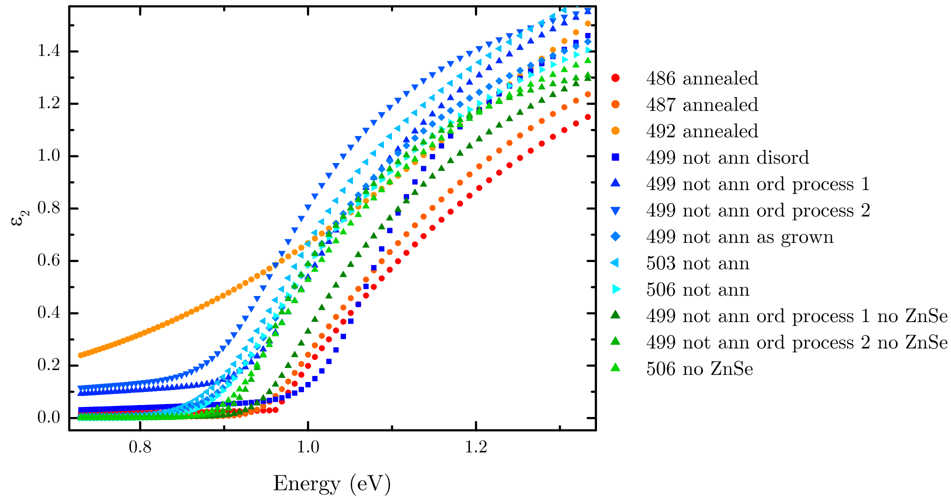

Figure 3.7.: Zoom on the onset of ε_2.

Since ε_2 can be related to the absorptivity of the sample, it is clear that it should be zero at those energies, where there are no allowed states, i.e. below the band gap energy or, in the case of tail states, below the energetic distance between valence and conduction band tails. It will be shown in chapter 4 that the room temperature photoluminescence emission of the samples is at energies of $0.85 - 0.93\,\mathrm{eV}$. Under the assumption that the photoluminescence comes from the lowest energetic states possible, which are the tail states, as will be shown in chapter 4 as well, it follows that ε_2 should not significantly deviate from zero below those energies. Therefore the following models are discarded for the subsequent discussion: 492, 499 ordered process 1 with ZnSe and 499 ordered process 2 with ZnSe.

Figures 3.8, 3.9 and 3.10 show the remaining physical dielectric functions of the CZTSe-layers of those samples, which could be fitted using the models described in the previous section with reasonable thicknesses. The corresponding thicknesses and the MSE are listed in table 3.2 and the plots of the fits can be found in appendix A.2.

From the figures it is clear that the general shape of $\tilde{\varepsilon}$ is similar for all the different models, that were used. According to the MSE values in table 3.2 and the fits in appendix A.2, the description of the not annealed samples by their respective model is generally better than the description of the annealed samples. Looking at the fits, it is clear that the description of the experimental data in the energy range above roughly

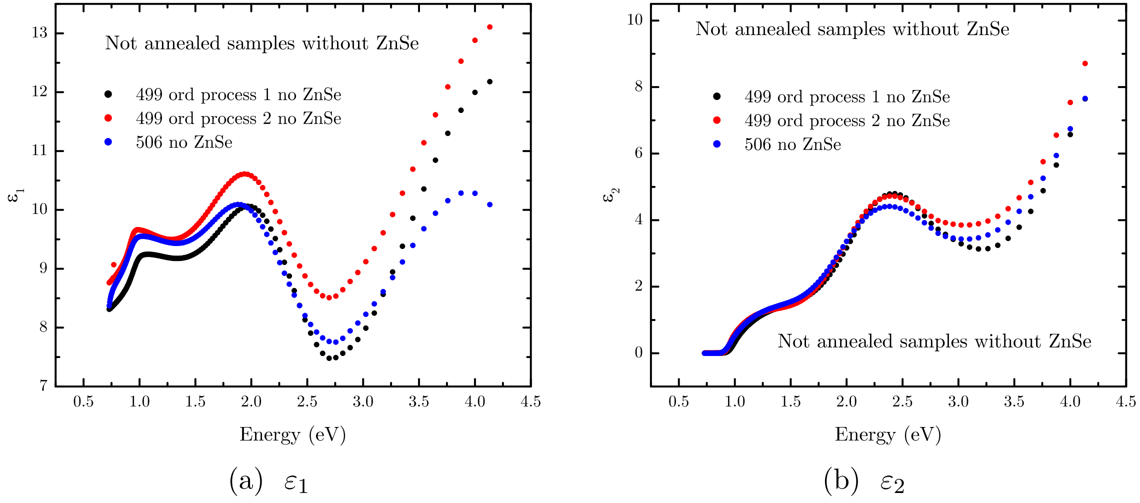

(a) ε_1 (b) ε_2

Figure 3.8.: Dielectric functions of the not annealed samples, without the inclusion of the additional ZnSe-layer in the model.

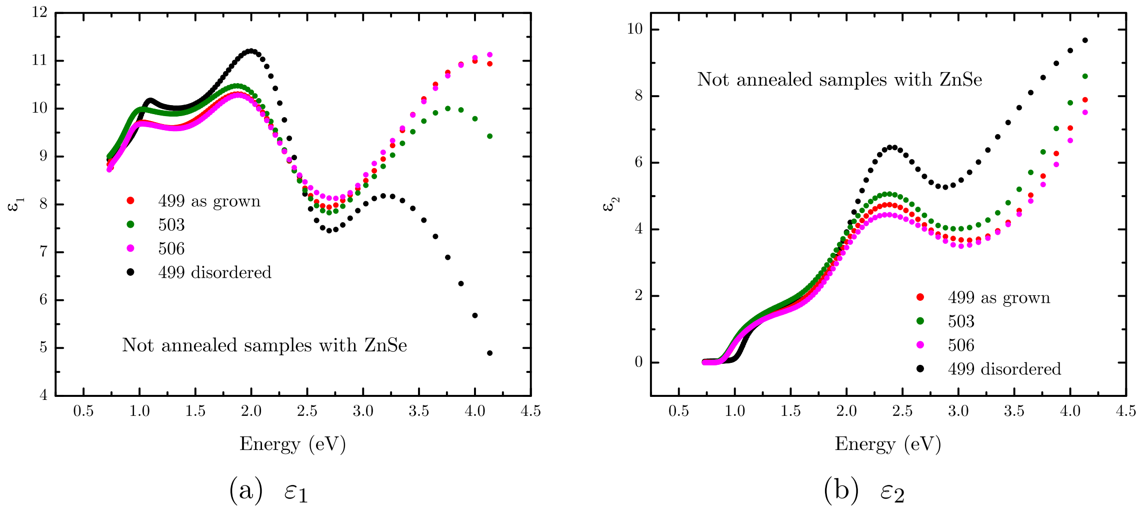

(a) ε_1 (b) ε_2

Figure 3.9.: Dielectric functions of the not annealed samples, with the additional ZnSe-layer in the model.

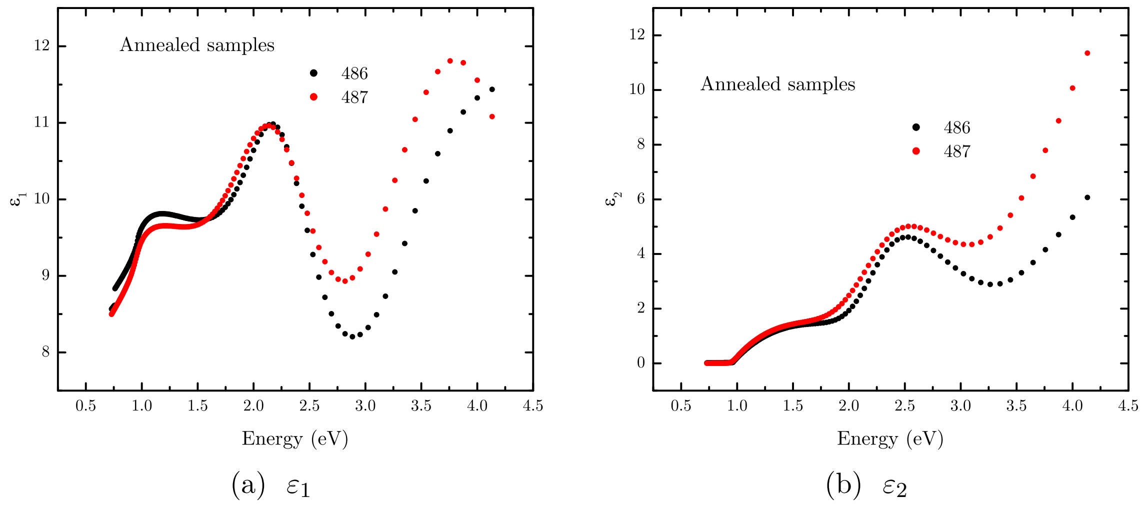

(a) ε_1 (b) ε_2

Figure 3.10.: Dielectric functions of the annealed samples, with the additional ZnSe-layer in the model.

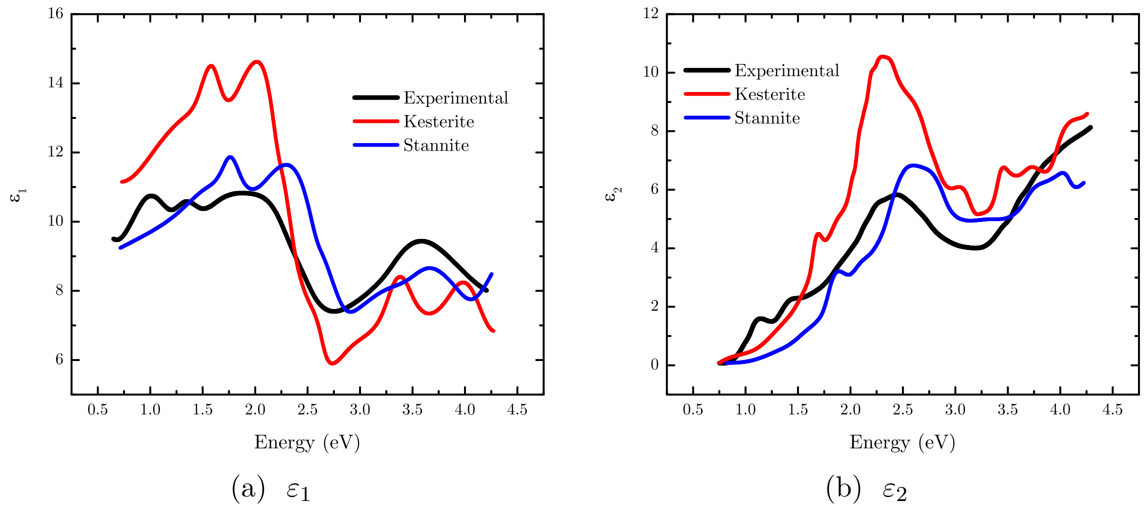

(a) ε_1 (b) ε_2

Figure 3.11.: Dielectric function of CZTSe as determined by Choi et al. The black line represents the dielectric function determined by spectroscopic ellipsometry on a co-evaporated polycrystalline CZTSe-film. The red and the blue lines are the dielectric functions for CZTSe in the kesterite and the stannite configuration respectively, calculated with a GW approximation. Adapted from [70] and [71].

1.2 eV, where the oscillations due to interference effects are decreasing, is better in case of the not annealed samples compared to the annealed samples. It was observed that the ZnO-layer in the annealed samples mainly affected the high energy part of the fit, which can be explained by the fact, that the ZnO was modeled with a bandgap of 3.2 eV. The poorer agreement between the fit and the data around 1.2 eV might then indicate, that the model is not perfectly suitable for the description of the annealed samples. One reason for this might be that, due to the increased heater temperature during the annealing stage, a part of the CZTSe has decomposed and formed an additional layer, which is not contained in the model.

To compare the measurements to the literature and theoretical predictions, figure 3.11 shows the dielectric function of a co-evaporated polycrystalline CZTSe-film, deposited on Mo-coated soda-lime glass, as determined by Choi et al. [70] with spectroscopic ellipsometry. The plot also shows the dielectric function for CZTSe in both the kesterite and the stannite structure, calculated by Zhao et al. using a GW approximation [71].

The general shape of $\tilde{\varepsilon}$ of the polycrystalline film is similar to that of the epitaxial samples, with the exception of the disordered piece of sample 499 (figure 3.9). However, the maximum in ε_1 at 1 eV is as high as the maximum at 2 eV in the polycrystalline film. In the epitaxial samples the 2 eV maximum is generally higher than the 1 eV maximum. Furthermore the polycrystalline film has an additional maximum around 1.2 eV, which is not observed in the epitaxial samples. Comparing the experimental data to the theoretical calculation shows, that the position of the maximum around 2 eV in ε_1 is better described by the kesterite structure, even though the values of ε_1 are closer to the stannite structure.

In the case of ε_2, there is also good agreement between the epitaxial samples and the polycrystalline film. The polycrystalline again shows a structure around 1.2 eV, which is not visible in the epitaxial samples. The position of the maximum around 2.5 eV in ε_2 is better described by the kesterite structure as well.

The not annealed sample 506 (figure 3.12) was the only sample, which could be fitted with both models, with and without the additional ZnSe-layer. In this case the model with the ZnSe-layer results in the better fit of the data, as can be seen from the MSE values in table 3.2. Since the best fit thicknesses for the CZTSe and the ZnSe-layer have reasonable values, this is an indication that the model containing the additional ZnSe-layer might indeed describe the samples more accurately. If an inappropriate layer was included in the model, its best fit thickness would be likely to be either zero or unreasonably large. The comparison of $\tilde{\varepsilon}$ obtained with the two models for sample 506, is shown in figure 3.12. From this plot it can be seen that the apparent changes in the dielectric function, which are due to the inclusion of the ZnSe-layer, are rather small.

In order to quantify and to better compare the different dielectric functions, their critical points can be further analyzed. It was shown section 3.1.3 that Van Hove singularities in the JDOS are reflected in the dielectric function. Under the assumption that the bands follow a parabolic dispersion curve in the vicinity of these critical points, the dielectric function as a function of energy E can be described by the following expression

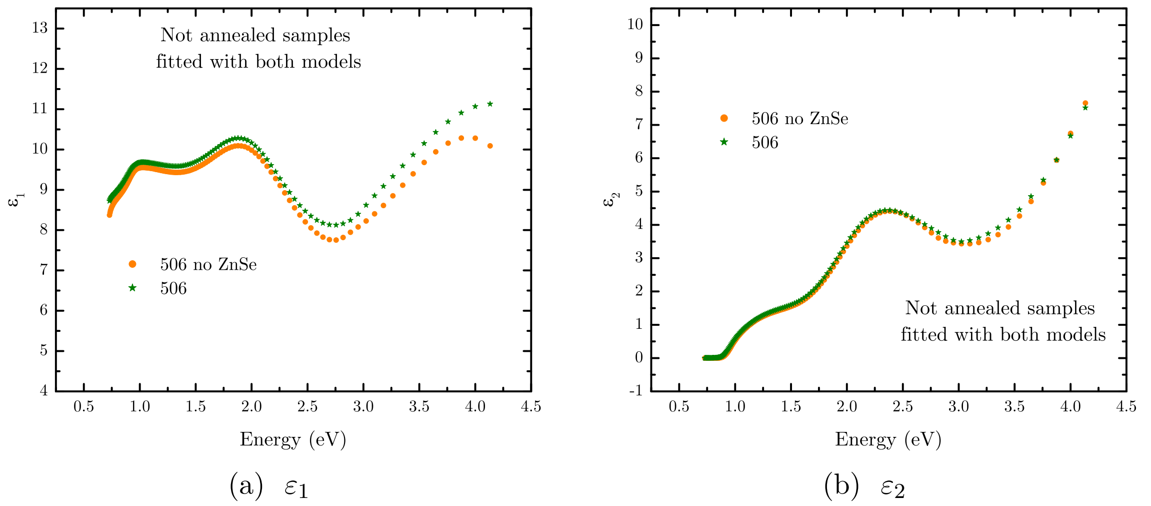

(a) ε_1

(b) ε_2

Figure 3.12.: Comparison of the dielectric functions obtained for the not annealed samples, that were fitted with and without the additional ZnSe-layer.

Table 3.2.: Thicknesses d and MSE obtained from the best fits. For comparison the thickness determined from the SEM cross sections d_{SEM} is also given.

Sample	Annealed	$d_{GaAs\text{-}Ox}$/[nm]	d_{ZnSe}/[nm]	d_{CZTSe}/[nm]	Surface oxide	$d_{Surf.\ Ox.}$/[nm]	MSE	d_{SEM}/[nm]
499 as grown	no	2.41	14.42	1080.80	SnO_2	7.86	9.51	1119
499 disord.	no	1.96	0.00	1075.68	SnO_2	3.31	12.42	1119
503	no	2.70	23.33	1040.50	SnO_2	5.19	18.80	1049
506	no	2.44	11.81	1189.39	SnO_2	7.96	23.03	1236
499 ord. proc. 1 no ZnSe	no	2.46	-	1156.44	SnO_2	10.62	9.32	1119
499 ord. proc. 2 no ZnSe	no	2.81	-	1116.65	SnO_2	8.99	15.14	1119
506 no ZnSe	no	2.44	-	1231.85	SnO_2	8.32	29.87	1236
486	yes	2.69	17.28	1012.51	ZnO	13.75	121.8	1057
487 as grown	yes	2.56	24.89	1052.21	ZnO	10.69	36.52	1108

[72]:

$$\tilde{\varepsilon}(E) = C - Ae^{i\phi}(E - E_{\text{cp}} + i\Gamma)^n \tag{3.18}$$

Here C is a constant, E_{cp} is the energy value of the critical point, A is an amplitude, which contains the matrix element of the transition, and Γ is a broadening parameter. The parameter n can take on the values 0.5, 0, -0.5 and -1, for a three-, a two-, a one-dimensional critical point or for an excitonic transition respectively. These values for n reflect the energy dependence of the underlying density of states $D(E)$, which is $D(E) \propto \sqrt{E}$ for a three-dimensional system, $D(E) = \text{const}$ for a two-dimensional system and $D(E) \propto 1/\sqrt{E}$ for a one-dimensional system (see for example [43]). The exitonic transition is described by a Lorentzian line shape, which is represented by setting $n = -1$ in equation 3.18 [73].

The value of phase factor ϕ depends on the nature of the critical point: In case of a three-dimensional band structure $\phi = 0\,^\circ$ for a minimum, $\phi = 90\,^\circ$ or $\phi = 180\,^\circ$ for a saddle point and $\phi = 270\,^\circ$ for a maximum. In the two-dimensional case $\phi = 0\,^\circ$ for a maximum, $\phi = 90\,^\circ$ for a saddle point and $\phi = 180\,^\circ$ for a maximum. In the one-dimensional case $\phi = 270\,^\circ$ for a minimum and $\phi = 0\,^\circ$ for a maximum [64]. If ϕ assumes values, which are not integer multiples of $\pi/2$, this indicates the mixing of two critical points [74].

Instead of directly fitting the dielectric function, it is preferable to fit the second derivative of $\tilde{\varepsilon}$ with the second derivative of equation 3.18:

$$\frac{\partial^2 \tilde{\varepsilon}}{\partial E^2} = \begin{cases} n(n-1) \cdot Ae^{i\phi}(E - E_{\text{cp}} + i\Gamma)^{n-2}, & n \neq 0 \\ Ae^{i\phi}(E - E_{\text{cp}} + i\Gamma)^{-2}, & n = 0 \end{cases} \tag{3.19}$$

The advantage of using the second derivative is that it is more sensitive to critical point structures. [74]. In the ideal case, the second derivative is non-zero only around critical points. This makes it easier to resolve critical point structures in $\frac{\partial^2 \tilde{\varepsilon}}{\partial E^2}$, which might not be as apparent in $\tilde{\varepsilon}$.

In order to fit these expression, the derivatives $\frac{\partial^2 \tilde{\varepsilon}_1}{\partial E^2}$ and $\frac{\partial^2 \tilde{\varepsilon}_2}{\partial E^2}$ were calculated numerically. Then equation 3.19 was fitted simultaneously to both the real and the imaginary part of the second derivative of $\tilde{\varepsilon}$ around the CP features.

The three-, the two- and the one-dimensional expressions of equation 3.19 were used to fit the dielectric function. A critical point in a semiconductor with an otherwise three-dimensional band might be better described with the two- or one-dimensional function, if the effective mass is very large in two or one dimensions, compared to the other effective masses [64]. Persson found, by using a relativistic full-potential linearized augmented plane wave method, that the transverse masses $m_{\text{v}}^{\perp}$ of the uppermost valence band, with respect to the (001) direction, are considerably larger than the longitudinal mass $m_{\text{v}}^{\parallel}$ ($m_{\text{v}}^{\perp}/m_{\text{v}}^{\parallel} = 3.67$) at the Γ-point [27]. Therefore the lower dimensional functions were included as well.

For the fit, the parameter n was set to the fixed values of 0.5, 0, -0.5 or -1, for the respective dimension of equation 3.19. This means that every critical point was fitted

multiple times with all possible combinations of n and ϕ. The parameters A, Γ and E_{cp} were required to be positive, but were freely fitted otherwise. The phase angle ϕ was freely fitted.

Table 3.3 shows the critical point energies E_{cp} extracted from the best fit and the corresponding parameter n for all physical dielectric functions. The phase angle ϕ assumed values close to $0\,^\circ$ in all cases, which indicates that there is no influence of intermixing between critical points on the fits. Therefore it is not listed here.

Table 3.3.: Critical point energies and the corresponding dimensionality parameter n from the best fit.

Sample	Annealed	ZnSe-layer	E_{cp} [meV]	n
486	yes	yes	0.962 ± 0.001	0.5
			2.246 ± 0.010	-1
			2.742 ± 0.045	-1
487 as grown	yes	yes	0.957 ± 0.001	0.5
			2.068 ± 0.014	-1
			3.040 ± 0.040	-1
499 as grown	no	yes	0.929 ± 0.001	-0.5
			1.930 ± 0.021	-1
499 disordered	no	yes	1.056 ± 0.001	-0.5
			2.161 ± 0.011	-1
			2.566 ± 0.017	-1
503	no	no	0.933 ± 0.001	-0.5
			2.006 ± 0.019	-1
506	no	yes	0.920 ± 0.001	0
			1.875 ± 0.017	-1
			2.613 ± 0.051	-1
499 ordered process 1 no ZnSe	no	no	0.968 ± 0.001	-0.5
			2.202 ± 0.014	-1
499 ordered process 2 no ZnSe	no	no	0.934 ± 0.001	0
			2.007 ± 0.016	-1
506 no ZnSe	no	no	0.930 ± 0.001	0
			1.947 ± 0.017	-1
			2.578 ± 0.060	-1

3.3.1. Discussion

The first thing to note is that for some samples three critical points could be fitted, while for the remaining samples only the two lowest critical points could be extracted. The reason for this is that the high energy part of $\frac{\partial^2 \tilde{\varepsilon}}{\partial E^2}$ of the latter samples exhibits a kink, which makes a reasonable fitting in this range impossible. In general the uncertainty of

the highest critical point position is larger, than for the lower critical points. The fits of the derivative spectra are shown in appendix A.3.

From table 3.3 it can be seen that the energies of the first critical points, which can be identified with the fundamental band gap, are larger in the annealed samples. Apparently the in-situ annealing step during the growth leads to an increase of the band gaps. Comparing the band gaps of the as grown piece of sample 499 to the ordered pieces shows, that the ordering process 1 leads to an increase of the band gap of almost 40 meV, while the band gap of the piece, treated with the ordering process 2, does not drastically change. Based on this observation it can be argued that the ordering process 1 is more efficient in removing $Cu_{Zn} + Zn_{Cu}$ antisites, than the ordering process 2.

One rather counter-intuitive result is, that the disordered piece of sample 499 shows the highest band gap of all samples. This is unexpected because a disordering procedure should lead to a smaller band gap, if the sample is not in a completely disordered state after the growth anyway (see section 2.3.2). Since this sample was grown without the annealing stage, a possible explanation for this is, that the dwell temperature of 250 °C during the disordering has an additional annealing effect on the crystal, apart from increasing the density of $Cu_{Zn} + Zn_{Cu}$ antisites. Another indication for this effect is that the maximum of the photoluminescence emission of the disordered piece of 499 is at higher energies, than that of the as grown piece, as will be shown in the next chapter.

With the exception of the disordered piece of 499, the band gaps are smaller than the expected fundamental band gap of 1 eV [27]. There are several possible origins for this discrepancy. Since the lattice constants of the GaAs-substrate and CZTSe are slightly different, as was shown in section 2.2, the CZTSe-films are likely to contain strain, which generally alters the band gap of a semiconductor (see for example [75]). Furthermore it is known that a high doping density leads to a narrowing of the band gap, compared to the undoped material [76]. Another factor contributing to the low band gap might be the influence of tail states. It will be discussed in the next chapter, that a high level of doping leads to a fluctuating band structure, which in turn leads to the existence of tail states within the band gap. These tail states might lead to a decrease of the band gap, as it is measured by ellipsometry.

The best fits of the band gaps of the annealed samples were obtained with the three-dimensional band structure ($n = 0.5$), while the band gaps of the not annealed samples are best described by either the one-dimensional ($n = -0.5$) or the two-dimensional ($n = 0$) band-structure. The description of the band gap of the not annealed samples with $n = -0.5$ coincides with the previously stated calculation, that the transverse effective hole masses, with respect to the (001) direction, in the uppermost valence band of CZTSe are larger than the longitudinal mass at the Γ-point. This might lead to an effective lower-dimensional band structure [64]. However, the differences between the effective masses is less than on order of magnitude. This is in agreement with the fact, that the fits of the band gap with the higher-dimensional variations of equation 3.19 were only slightly worse, than the best fit. In the same way, the best fits of the band gaps of the annealed samples with $n = 0.5$ are only slightly better, than the fits with the one- or the two-dimensional line shape. If the mass difference was significantly larger,

the fit was likely to strongly prefer the one- or the two-dimensional form of equation 3.19. The difference in the band gap energy between the best fit and the other band structures was roughly $2 - 3\,\text{meV}$.

The energies of the higher critical points are correlated with the band gap energies. The larger the band gap the higher the energies of the higher critical points, which means that the annealing stage induces a shift of the band structure as a whole. The exception to this is the disordered piece of the sample 499, which has the lowest energy of its third critical point among those samples, for which three critical points could be fitted.

The energies found here are lower compared to the critical point energies reported by Choi et al. [70] at 2.4 eV and 3.5 eV and by Hirate et al. [77] at 2.4 eV and 3.8 eV. In their publication Choi et al. also determined the critical point energies of the dielectric functions, which were calculated by Zhao et al. for CZTSe in both the stannite and the kesterite structure [71]. They reported values of 2.34 eV and 3.52 eV for the two critical points above the band gap of the kesterite structure, and 2.57 eV and 4.00 eV for the stannite structure. These values are considerably higher then the critical point energies of the epitaxial samples as well and therefore it is not possible to conclude, whether the epitaxial growth might stabilize the stannite structure or not.

It could be argued that this discrepancy in the higher critical points is caused by the same mechanisms, which also cause the decrease of the band gap. At least it was shown by Kuball et al. that a high level of doping in GaAs decreases the energy of higher critical points as well as the band gap [78].

The best fits of the higher critical points were all obtained with the excitonic line shape ($n = -1$), which is in accordance with the observations made by Choi et al. [70]. The difference in E_{CP} for the higher critical points between the best fit and the remaining variations of equation 3.19 were up to 30 meV.

In conclusion it was shown that the dielectric function of the epitaxial CZTSe-samples could be extracted from spectroscopic ellipsometry measurements. By fitting the second derivative of $\tilde{\varepsilon}$ around critical point structures with an analytical expression (equation 3.19), the fundamental band gap and the energies of the higher critical points could be determined. It was found that the band gap and the higher critical points of the annealed samples are slightly higher than that of the not annealed samples. Furthermore it was found that the disordering procedure, which was used in this work, seems to have an additional annealing effect on the not annealed samples, next to increasing the density of $\text{Cu}_{\text{Zn}} + \text{Zn}_{\text{Cu}}$ antisites. It was observed that the ordering procedure not only increases the fundamental band gap, but also the energies of the higher critical points. Generally the extracted band gaps and critical point energies are lower than the values reported in literature, which can be explained by stress in the epitaxial samples and a high level of doping.

4. Photoluminescence

This chapter deals with the photoluminescence (PL) measurements on the epitaxial CZTSe samples and the conclusions, that can be drawn about the involved states. In the first section the theoretical background of PL is presented, especially in semiconductors with a fluctuating band structure. The measurements are shown in the subsequent section.

4.1. Principles of Photoluminescence

The term photoluminescence describes the emission of light from a sample after it has been excited with photons. In a semiconductor this excitation occurs when a photon of sufficient energy is absorbed by an electron in the valence band. The electron is then lifted into the conduction band, leaving a positively charged hole in the valence band. In a PL experiment the energy of the exciting photons is usually considerably higher than the band gap of the semiconductor and consequently, the excited charge carriers are located deep within their respective band right after the absorption of the photon. In the next step, the charge carriers rapidly lose energy through interactions with the lattice. In the simple case of a semiconductor with flat bands (see figure 4.1) this interaction continues until they have reached a quasi-equilibrium distribution around the band edges. In this state, which is reached roughly $\Delta t \approx 10^{-12}\,\mathrm{s}$ after the excitation, the charge carrier distribution can be described by two quasi-Fermi levels, one for the electrons in the conduction band and one for the holes in the valence band [79].

In the last step, an electron from the conduction band can recombine with a hole in the valence band under the emission of a photon. The energy of the emitted photon is determined by the energy difference between the two recombining charge carriers. Since the time scale for radiative recombination is usually in the order of $10^{-9}\,\mathrm{s}$ to $10^{-6}\,\mathrm{s}$ [73] and thereby much slower than the thermalization of the charge carriers, the recombination always occurs from the quasi-equilibrium state independent of the initial photon energy (provided it is higher than the band gap).

This gives rise to the band-to-band (BB) transition, whose spectral shape follows Planck's generalized law [79]:

$$I_{\mathrm{PL}}^{\mathrm{BB}}(E) \propto \frac{A(E)E^2}{\exp\left(\frac{E-\Delta F}{k_{\mathrm{B}}T}\right) - 1} \tag{4.1}$$

Here $A(E)$ denotes the absorptivity of the semiconductor. The low energy flank of the emission is governed by the absorptivity, which contains the regular energy dependence

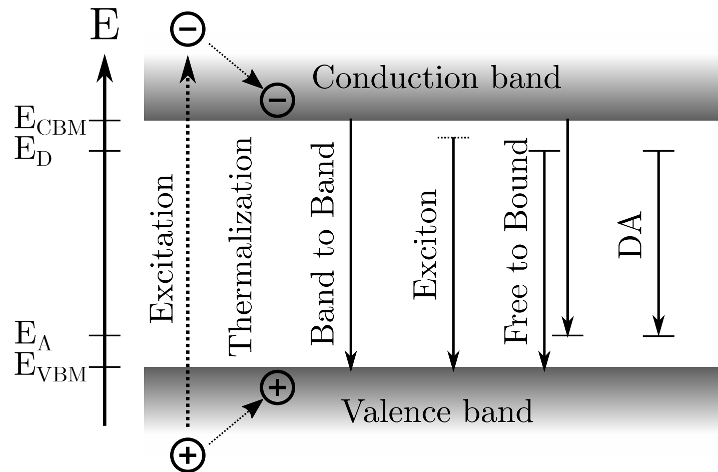

Figure 4.1.: Processes during a PL experiment in a semiconductor with flat bands. The charger carriers, that are created through the absorption of a photon thermalize to the band edges or into defect states, from where they recombine radiatively via the different recombination channels. E_{CBM} and E_{VBM} denote the energy of the conduction band minimum and the valence band maximum respectively, E_D and E_A are the energies of the donor and acceptor states. Based on [80].

of the density of states (DOS), and any additional tail states, which contribute to the absorption. The high energy side follows a Boltzmann-distribution, where the quasi-Fermi level splitting ΔF is the energetic difference between the two quasi-Fermi levels describing the electron and the hole distributions. This particular spectral shape reflects the fact that the radiative recombination occurs out of a quasi-equilibrium [79].

At low temperatures an electron hole pair can be bound together by their Coulomb interaction and form an exciton. The energy of the excitonic emission is diminished by the Coulomb energy between the two carriers with respect to the BB transition [80].

If the semiconductor contains additional states, due to dopant atoms or native defects, within the band gap, these states can contribute to the PL emission as well. An electron recombining from a donor state with a free hole in the valence band, or a free electron recombining with a hole in an acceptor state gives rise to the free-to-bound transition. Furthermore, an electron in a donor state can recombine with a hole in an acceptor state, which results in the donor-acceptor (DA) transition [80].

All these recombination channels are depicted in figure 4.1. They will not be discussed in greater detail, because it will be shown in the following section that the epitaxial samples cannot be described with these transitions, which are found in semiconductors with flat bands. However, this short overview was given anyway, because it might aid in the discussion of the recombination channels in a semiconductor with non flat bands.

4.2. Photoluminescence in a Semiconductor with a Fluctuating Band Structure

4.2.1. Density of States of a Heavily Doped Semiconductor

The semiconductor discussed in the previous section has a flat band structure, meaning the the conduction band minimum and the valence band maximum are at constant energies throughout the crystal and their density of states shows a square root dependency on the energy. Adding a small amount of dopant atoms creates localized defect states close to the conduction or the valence band while leaving the flat band structure undistorted in the first approximation.

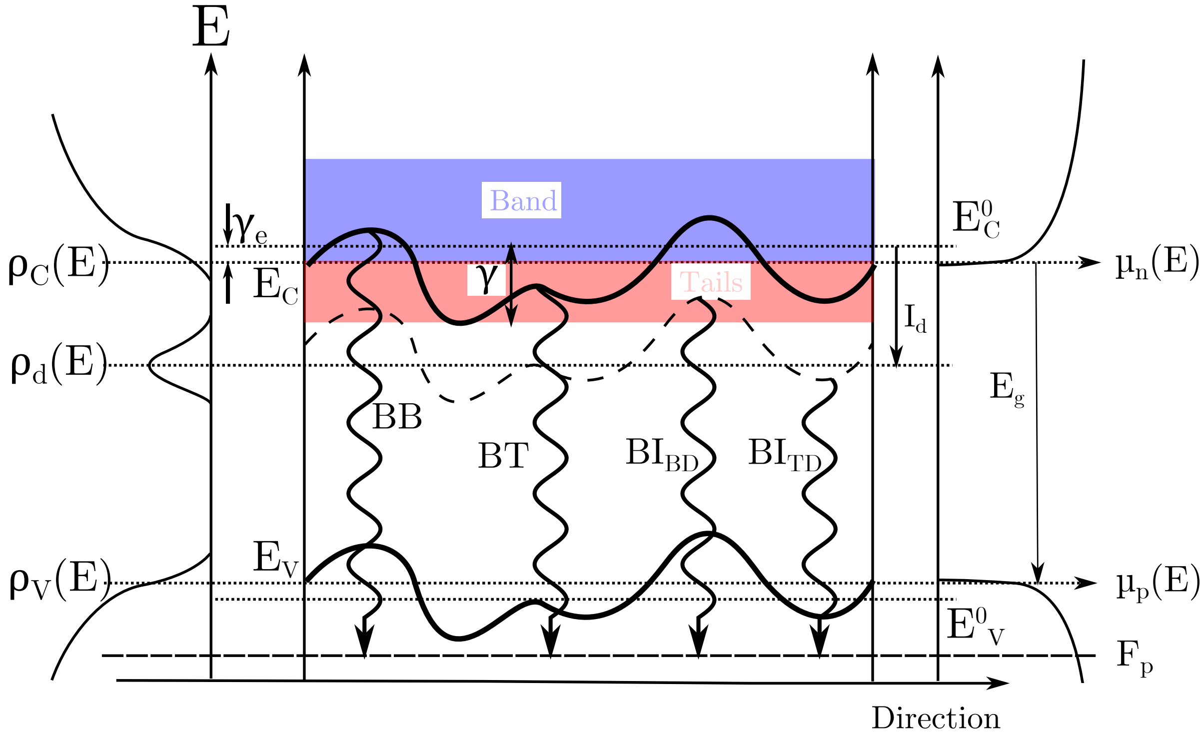

Figure 4.2.: Band structure of a heavily doped, degenerate p-type semiconductor. The left part shows the densities of states (DOS) ρ. The middle part shows the fluctuating band edges and one fluctuating, localized donor level. The right part shows the carrier mobility μ and the percolation levels E_{C} and E_{V}, at which the mobility decreases to zero. The wavy lines represent the BB, BT and BI transition. The Fermi-level F_{p} indicates the energy in the valence band, into which the majority of electrons recombine. Based on [81].

This does not apply any longer in the case of heavy doping. If the doping is high enough that the heavy doping condition [81],

$$N_{\mathrm{imp}} a_{\mathrm{imp}}^3 > 1, \tag{4.2}$$

is fulfilled, then the defect levels are so close to each other that their wave functions overlap and a defect band is formed. In this expression N_{imp} is the density of dopant atoms or native defects, which lead to the doping and which are summarized as impurity in this context, and a_{imp} is the Bohr radius of an impurity site. Depending on whether the impurity atoms act as donors or as acceptors, this band merges with the conduction or the valence band [82]. As a consequence of this merging, the additional charge carriers from the defect level can move freely in the band, which leaves the impurity sites ionized. The electrostatic interaction of the charge carriers in the band with the impurity ions leads to a deviation of the parabolic dispersion relation $E(k)$ for a free electron gas. A result of this is the existence of extended tail states [82]. Furthermore the impurities are distributed randomly throughout the crystal at high concentrations. Therefore the electric field from the ionized impurity atoms is not constant in space. Consequently the interaction between charge carriers and impurity ions is not constant in space as well. This leads to a fluctuating band structure as shown in figure 4.2 with the average fluctuation depth γ.

A consequence of such an aperiodic potential is the formation of states, for which the charge carrier mobility decreases to zero because the overlap with the neighboring states vanishes [83]. These states will be referred to as localized tail states in this work, while the states with non-vanishing carrier mobility will be called band states. The former are marked in red in figure 4.2 and the latter are marked in blue.

The existence of these localized states has implications for the radiative recombination channels. For their discussion, which is based on [81] in large parts, a degenerate p-type semiconductor is assumed, which fulfills the heavy doping condition (equation 4.2) for acceptors. The value of the impurity density, for which the heavy doping condition is fulfilled, depends on the Bohr radius, which in turn is inversely proportional to the effective charge carrier mass [81, 84]. This means that the higher the effective mass, the higher the impurity density required to fulfill the heavy doping condition. Levanyuk and Osipov [81] state that n-type InSb is heavily doped from impurity concentrations of $N_{\mathrm{imp}}^{\mathrm{InSb}} \geqslant 10^{14}\,\mathrm{cm}^{-3}$ on. Using the effective electron mass at the Γ-point of $m_{\mathrm{c}}^{InSb} = 0.014 m_0$ [85], with m_0 being the electron rest mass, and equation 4.2, the critical impurity density N^{c}, from which on the semiconductor can be regarded as heavily doped, can be related to the effective mass by:

$$N^{\mathrm{C}} = \mathrm{C} \cdot m_{\mathrm{eff}}^{3} \tag{4.3}$$

The constant C can be calculated from the aforementioned parameters of InSb as $\mathrm{C} \approx 3 \cdot 10^{11}\,\mathrm{cm} \cdot \mathrm{keV}^{-3}$. For this an electron rest mass of $m_0 = 511\,\mathrm{keV}$, from [86] in natural units, was used. Under the assumption that the only variable parameter in the calculation of the Bohr radius is the effective mass, this constant can also be used to estimate the critical doping density for p-type CZTSe. The effective hole mass of CZTSe at the Γ-point can be calculated from the two transverse and the longitudinal mass obtained by Persson [27] (see section 3.3) as $m_{\mathrm{v}}^{\mathrm{eff}} = 2/3 \cdot m_{\mathrm{v}}^{\perp} + 1/3 \cdot m_{\mathrm{v}}^{\parallel} = 0.25 \cdot m_0$. With this the critical doping density of p-type CZTSe can be estimated to $N_{\mathrm{CZTSe}}^{\mathrm{C}} \approx 6 \cdot 10^{17}\,\mathrm{cm}^{-3}$.

Due to the degeneracy the Fermi-level F_{p} lies in the valence band, below the localized valence band tail states. Therefore the majority of holes, that contribute to the emission

in a PL experiment, stems from free band states near the Fermi-level. As a consequence, the emission depends only on the conduction band tail states while the influence of the valence band tail can be ignored.

In practice, all heavily doped are compensated to a certain degree, so they also contain also dopants of the minority carrier type [81]. If, in the case of a degenerate p-type semiconductor, the heavy doping condition also applies for donors, $N_\mathrm{d} a_\mathrm{e}^3 > 1$ with the donor density N_d and the Bohr radius of a donor a_e, but $N_\mathrm{d} < N_\mathrm{a}$, then the donor states form a band as well, which merges with the conduction band. The PL emission in this case can then show band-to-band (BB) transitions, which are the recombinations of free holes with free electrons, and band-to-tail (BT) transitions, which are the recombinations of free holes with electrons trapped in the localized tail states of the conduction band.

If the heavy doping condition is not fulfilled ($N_\mathrm{d} a_\mathrm{e}^3 \ll 1$) the donor states do not overlap to a band. Instead they form a level of localized defect states, which is distorted through electrostatic interaction with the randomly distributed acceptors, similar to the distortion of the band edges. If then the ionization energy I_d of the defect level is larger than the average fluctuation depth, $I_\mathrm{d} > \gamma$, the DOS has a local maximum at I_d, which can be described as [81]

$$\rho_\mathrm{d}(E_\mathrm{e}) = \frac{N_\mathrm{d}}{\sqrt{2\pi}\gamma} \exp\left[-\frac{(E_\mathrm{C}^0 - E_\mathrm{e} - I_\mathrm{d})^2}{2\gamma^2}\right], \tag{4.4}$$

where E_C^0 is the energy of the unperturbed conduction band. In this situation a free hole can recombine with an electron trapped in the defect level. This process is called band-to-impurity (BI) transition.

These three recombination channels will be discussed in greater detail in the following sections.

4.2.2. Band to Band Transitions

Since the thermal relaxation of free charge carriers after excitation is much shorter than the radiative recombination time, the distribution of holes and electrons in the band states is in a quasi-equilibrium before they recombine. Therefore they can be described by quasi-Fermi levels f_n and f_p for electrons and holes. In the present case the degeneracy of the semiconductor needs to be taken into account. It can be shown that the spectral shape of the BB emission I_BB in a degenerate semiconductor is given by equation (1.18a) in [81]:

$$\begin{aligned} I_\mathrm{BB}(E) \propto E^2\sqrt{E - E_\mathrm{G}} \cdot &\left[\exp\left(\frac{E_\mathrm{C} - f_\mathrm{n}}{k_\mathrm{B}T} + \frac{m^*(E - E_\mathrm{G})}{m_\mathrm{e} k_\mathrm{B} T}\right)\right]^{-1} \\ \times &\left[\exp\left(\frac{f_\mathrm{p} - E_\mathrm{V}}{k_\mathrm{B}T} + \frac{m^*(E - E_\mathrm{G})}{m_\mathrm{h} k_\mathrm{B} T}\right)\right]^{-1} \end{aligned} \tag{4.5}$$

with the effective electron and hole masses m_e and m_h and their reduced mass $m^* = m_\mathrm{e} m_\mathrm{h} \cdot (m_\mathrm{e} + m_\mathrm{h})^{-1}$.

4.2.3. Band to Tail Transitions

Unlike the band states, the distribution of electrons in the localized tail states cannot generally be described with a quasi-Fermi level. This is because the localization of the electrons prevents them from reaching a quasi-equilibrium.

To understand the behavior of the PL emission involving tail states, the tail states can be divided into *trapping* and *recombination* centers. The trapping centers are characterized by the fact that the time for thermal release into the free band states of a charge carrier is smaller than the time for radiative recombination. This means that the carrier distribution within these states is in a quasi-equilibrium but they do not contribute to the PL emission, because they thermalize into the free band states before they can recombine radiatively. The recombination centers satisfy the opposite condition, which is that the probability for radiative recombination is larger than the probability of thermal release. Therefore the carriers in these states contribute to the PL emission, but their distribution is generally not in a quasi-equilibrium.

Under steady state conditions, the trapping centers of the conduction band tails are separated from the recombination centers by the *demarcation* energy ε_e, which can be calculated as (adapted from equation (2.6a) in [81] such, that ε_e is defined with respect to the conduction percolation level E_C):

$$\varepsilon_\mathrm{e} \propto E_\mathrm{C} - k_\mathrm{B}T \ln\left(\frac{N_\mathrm{C}}{n+\theta p}\right) \tag{4.6}$$

Here N_C is the effective density of free band states in the conduction band and n and p are the total electron and hole densities respectively. The coefficient θ is calculated as $\theta = C_\mathrm{RR}/C_\mathrm{EC}$, where C_RR describes the probability of the radiative recombination of a free hole with an electron in a localized tail states and C_EC describes the capture of a free electron by a localized tail state [81]. It should be stressed that only radiative recombination is considered for the definition of the demarcation level. Non-radiative recombination is not taken into account.

Equation 4.6 describes the fact that at 0 K all tail states act as recombination centers, because there is no thermal energy to elevate electrons into the free band states. With increasing temperature, the shallower tail states begin to be thermally emptied and the demarcation level is shifted downwards in direction of the band gap center. At the same time, an increase in the charge carrier density causes ε_e to be shifted upwards because the probability of radiative recombination increases with n and p, i.e. θ increases.

As a consequence, a BT transition shows a red-shift at low temperatures with increasing temperature and the slope is determined by $\ln\left(N_\mathrm{C}/(n+\theta p)\right)$. With increasing excitation, and thereby charge carrier density, at a fixed temperature a blue-shift is expected, because more and more shallower tail states are turned into recombination centers.

For the behavior of the BT transition at elevated temperature there are two cases, which need to be treated separately:

If excitation intensity and doping level are sufficiently low, i.e. $n + \theta p$ is small, (but the doping level is still high enough to fulfill the heavy doping condition), the slope of

the shift of $\varepsilon_\mathrm{e}(T)$ with increasing temperature is so steep, that, at a certain temperature T_1, the demarcation energy lies within those tail states, which cannot be approached by a free hole. The reason for this behavior is that under these conditions, the kinetic energy of a free hole is so low that the potential of a deep tail state represents a barrier for the hole. From this temperature on the BT transition can only occur via tunneling. It can be shown that a further increase in temperature leads to a blue-shift of the emission, which turns into a red-shift again at a higher temperatures T_2, as it is shown in figure 4.3a (equation (2.15) in [81]). This can be explained in the following manner. At first an increase in temperature leads to a higher tunnel probability into the shallower recombination centers. This results in the blue-shift with increasing temperature from T_1 on. From T_2 on, the thermal emptying of the shallow recombination centers outweighs the higher tunneling probability with increasing temperature. Therefore, the emission exhibits a red-shift with increasing temperature from this point on.

At the temperature T_1, the electron distribution in the remaining recombination centers has reached a quasi-equilibrium form. From this point on, the maximum energy of the emission ceases to depend on the charge carrier density up to very high values of the excitation intensity, from which on it will exhibit a blue-shift with increasing excitation intensity (figure 4.3b). The rate of the excitation intensity, from which on the blue-shift is observed, increases with increasing temperature. The reason for this behavior is that, as soon as the quasi-equilibrium distribution within the recombination centers is reached, the probability of occupancy of the shallow states close to the demarcation energy is low. A further increase of the excitation intensity shifts ε_e upwards, but this becomes only visible when the shallower recombination centers are occupied. This situation is comparable to a BB transition, for which an increase in the quasi-Fermi level splitting with increasing excitation intensity does not change the PL peak position [87].

In the case of high doping and high excitation rates, when $n + \theta p$ is large, the slope of $\varepsilon(T)$ is so shallow that the demarcation level lies within the tail states, which can be freely approached by a free hole, at all temperatures. The expression θp can be estimated to be smaller than $10^{16}\,\mathrm{cm}^{-3}$ [81]. Furthermore, at high excitation rates the recombination is dominated by the non-radiative Auger recombination. Therefore the denominator $n+\theta p$ in equation 4.6 is limited. The resulting red-shift with increasing temperature is less pronounced than in the low excitation and low doping case. It continues until the carrier distribution in the tail states has reached a quasi-equilibrium form at a temperature T_3, which is higher than the temperature T_1. From this temperature on, a further increase in temperature results in an increasing uniformity of the carrier distribution. As a result of this, the shallower localized states begin to contribute more to the emission, which results in a blue-shift with increasing temperature from T_3 on. It can be shown that the energy E_m of the states with the highest occupancy can be calculated as (adapted from [81]):

$$E_\mathrm{m} \propto E_\mathrm{C} - \gamma^2/k_\mathrm{B}T \tag{4.7}$$

From T_3 on, the dependency of the maximum energy of the emission on the excitation intensity vanishes, as in the case of the low carrier density. For the same reasons, the

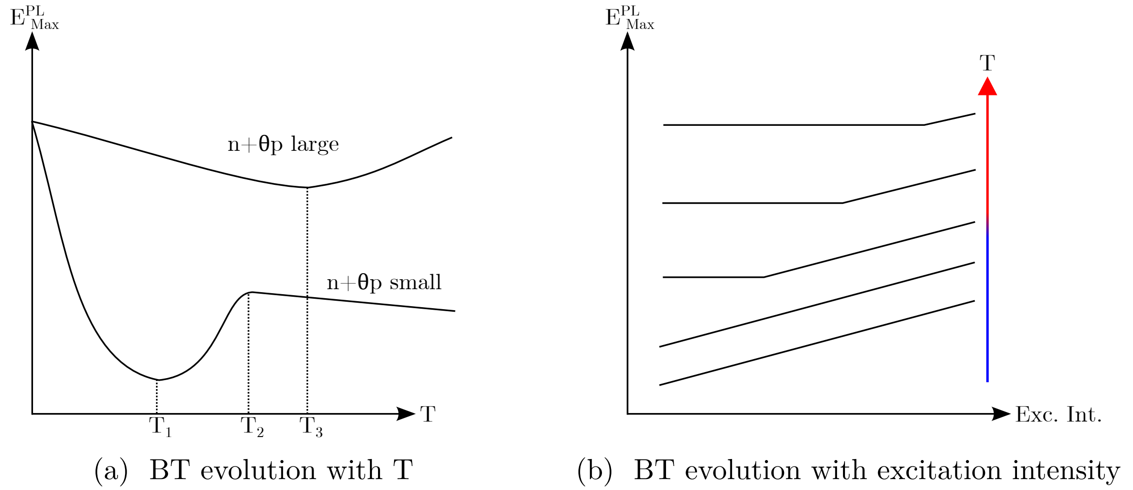

(a) BT evolution with T

(b) BT evolution with excitation intensity

Figure 4.3.: Qualitative behavior of the maximum of the PL emission of band-to-tail transitions with temperature and excitation intensity.

position of the maximum remains constant with increasing excitation intensity until it begins to blue-shift at high charge carrier densities.

The different types of behavior of the BT transition under varying experimental conditions are summarized in table 4.1 and depicted in figure 4.3.

Table 4.1.: Qualitative behavior of band-to-tail transitions under different experimental conditions.

$n + \theta p$	T range	T dependence	Exc. dependence
small	low: $T < T_1$	red-shift	blue-shift
	intermed.: $T_1 < T < T_2$	blue-shift	const., blue-shift for high exc.
	high: $T > T_2$	red-shift	const., blue-shift for even higher exc.
large	low: $T < T_3$	red-shift	blue-shift
	high: $T > T_3$	blue-shift	const., blue-shift for high exc.

4.2.4. Band to Impurity Transitions

In a PL experiment with an excitation energy higher than the band gap the filling of a localized defect level is a two step process. In the first step after the excitation, the generated charge carriers thermalize to the band edge. In the second step, the thermalized carriers are captured by a defect state at the same position. Therefore, the defect levels can be divided into two different types: The *tail defect* (TD) states and the *band defect* (BD) states. The TD states are those defect states, which are located at the site of a localized tail state and are filled by capturing carriers, that are localized in the tail states. The BD states on the other hand are located at the site of a free band state and are filled by capturing free carriers from the band states.

At low temperatures and low rates of excitation, all electrons thermalize into localized tail states. For this reason only the TD states can be filled and the BI transition consists solely of BI_{TD} transitions, which are the recombinations of free holes with electrons trapped in the localized tail states. In this case, the maximum of the emission is determined by the ionization energy of the defect level [81]:

$$E_{m}^{BI} = (E_{g} + E_{V}^{0} - F_{p}) - I_{d} \tag{4.8}$$

In this regime, the low energy side of the emission is characterized by the fluctuation depth γ [81]:

$$I_{BI}^{low\ T}(E) \propto \exp\left(-\frac{E^2}{\gamma^2}\right); \quad \text{for } E < E_{m}^{BI} \tag{4.9}$$

As soon as either excitation intensity or temperature become high enough that the free band becomes occupied, the BD states begin to be filled. This results in a blue-shift of the maximum energy and a broadening of the emission with increasing temperature or excitation intensity, because then the BI_{BD} transitions (the recombination of free holes with electrons in the BD states) become visible. The blue-shift with the broadening continues until all BD states are filled. From that point on, the shape and the position of the emission remain unchanged with further increase of either excitation intensity or temperature.

In conclusion, the behavior of the BI transition is characterized by a blue-shift and a broadening of the emission in a small range of excitation intensities or temperatures. This behavior is shown in figure 4.4. It can be shown that the energy, by which the maximum of the BI emission is shifted, is equal to the quantity γ_{e}, which is the difference between the percolation level and the unperturbed conduction band edge, so [81]

$$\gamma_{e} = E_{C} - E_{C}^{0}. \tag{4.10}$$

4.2.5. Conclusion

This section gave a brief summary of different recombination channels in a semiconductor with a fluctuating band structure and showed that their behavior is significantly different from the ones, that are observed in a semiconductor with flat bands (see for example [80]). These transitions are shown in figure 4.2. The discussion was limited to the case of a degenerate semiconductor, because Hall measurements (section 2.4.5) indicate that this is the correct description for the epitaxial samples. In case of a non degenerate semiconductor one would also have to take the localized tail states of the valence band into account. Then the PL could also show BT transitions from the conduction band into the valence tail states, tail-to-tail transitions and tail-to-impurity transitions. However, since these are probably not important for the epitaxial samples they were omitted in the discussion. Details about them can be found in reference [81].

The discussion here focused on a fluctuating band structure caused by the presence of randomly distributed ionized defect clusters. Since the key prerequisite of this discussion, the existence of localized tail states, is an inherent feature of a random potential,

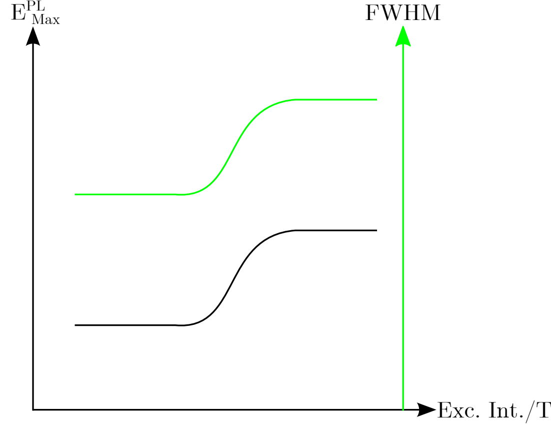

Figure 4.4.: Qualitative behavior of the maximum of the PL emission and the full width at half maximum (FWHM) of band-to-impurity transitions with temperature and excitation intensity.

the PL in a semiconductor with intrinsic band gap fluctuations should behave at least qualitatively in the same way as described above. One difference between the two cases is the different nature of the underlying potentials. This may lead to to a different shape of the DOS. In the case of a disordered system, as for example, with a potential with short-range correlations the resulting tail states may be described by an exponential form [88]. The fluctuating band structure in a heavily doped semiconductor on the other hand is caused by the Coulomb potential of ionized defect atoms, which is a long-range potential. This long-range correlation may exclude simple exponential band tailing [82].

However, the main difference is that the fluctuations due to charged defect clusters can be screened by free charge carriers, while the intrinsic band gap fluctuations cannot. This implies that the DOS of a heavily doped semiconductor depends on the charge carrier density and thereby on the excitation rate. According to Shklovskii and Efros, this screening can be approximated by a linear screening theory [89]. They show that the Coulomb-potential $\phi(r)$ of a localized charge in a degenerate electron gas, which is a good approximation for a heavily doped semiconductor, is screened as a function of the distance r in the following manner:

$$\phi(r) \propto \frac{e}{r} \exp\left(-\frac{r}{r_0}\right) \tag{4.11}$$

Here r_0 is the Thomas-Fermi screening radius for a degenerate electron gas, which depends on the electron density n as [89]

$$r_0 \propto a^{-1} \cdot n^{-1/6}, \tag{4.12}$$

with the Bohr radius a of the localized charge. Equation 4.11 indicates that the potential $\phi(r)$ is essentially screened out at a distance r_0. This means that the average fluctuation depth γ depends on the distribution of charged impurities within a sphere of the radius

r_0. It can be shown that they are correlated as $\gamma \propto \sqrt{r_0}$ [81]. Combining this with the correlation of the screening radius with the electron density (equation 4.12) yields:

$$\gamma \propto n^{-1/12} \tag{4.13}$$

This describes the dependency of the rms fluctuation depth on the charge carrier concentration. Transferring this to the epitaxial CZTSe-samples, the electron density n needs to be exchanged by the hole concentration p, since the majority of impurities are acceptors.

It should be noted that the screening radius r_0 decreases with increasing charge carrier density (equation 4.13). Therefore it can happen at sufficiently high doping densities, that r_0 becomes so small, due to the charge carriers coming from the doping, that the electrostatic fluctuations of the bands are completely screened. This issue will be addressed in the experimental section.

Besides the model presented here, which is based on the existence of localized tail states, another model was proposed by Yu [90], to describe the PL emission in semiconductors with fluctuating bands. In this model, Yu describes that the inherently flat band structure of a highly doped, compensated semiconductor is distorted due to electrostatic interactions with charged acceptors and donors. Since these charged defect sites are not distributed homogeneously in space, the semiconductor exhibits a fluctuating band structure, similar to the structure presented in the previous sections. The acceptor and the donor level follow the fluctuations of valence and conduction band respectively. The PL emission in this systems originates from the recombination of electrons, which are captured by the donor levels, with holes, which are captured by the acceptor levels. Yu argues that, at low temperatures, the cross section of the capture of a free charge carrier by the defect sites is smaller for those defects, that lie energetically deeper in the band gap. With increasing temperature, the different capture cross sections at different potentials begin to level out, and therefore the deeper defect sites begin to contribute more and more to the emission. As a consequence this emission, which was named “quasi-donor-acceptor-pair emission” by Yu, exhibits a red-shift with increasing temperature.

The evolution of the PL with increasing excitation intensity in such a system is described by Siebentritt [80]. An increasing excitation intensity leads to a higher density of free charge carriers, which in turn leads to more charged defect sites capturing a charge carrier. By capturing a charge carrier, the defect site is neutralized and therefore cannot distribute to the distortion of the band structure anymore. This leads to a flattening out of the fluctuations, which results in a blue-shift of the emission. This effect is augmented by the fact, that the fluctuations are also screened by the free charge carriers in the bands. Therefore, such a system exhibits a distinct blue-shift in the order of 10 meV per decade of excitation with increasing excitation intensity, which continues, until all charged defect sites are either neutralized or screened and the undistorted band structure is restored.

However, this model was not applied to the epitaxial samples in this work, because, as will be shown in the next sections, a blue-shift of that magnitude was not observed

in any sample. Furthermore the high net doping density indicates, that the degree of compensation in the epitaxial samples is rather small.

4.3. Photoluminescence Measurements on Epitaxial CZTSe Thin Films

4.3.1. PL Setup

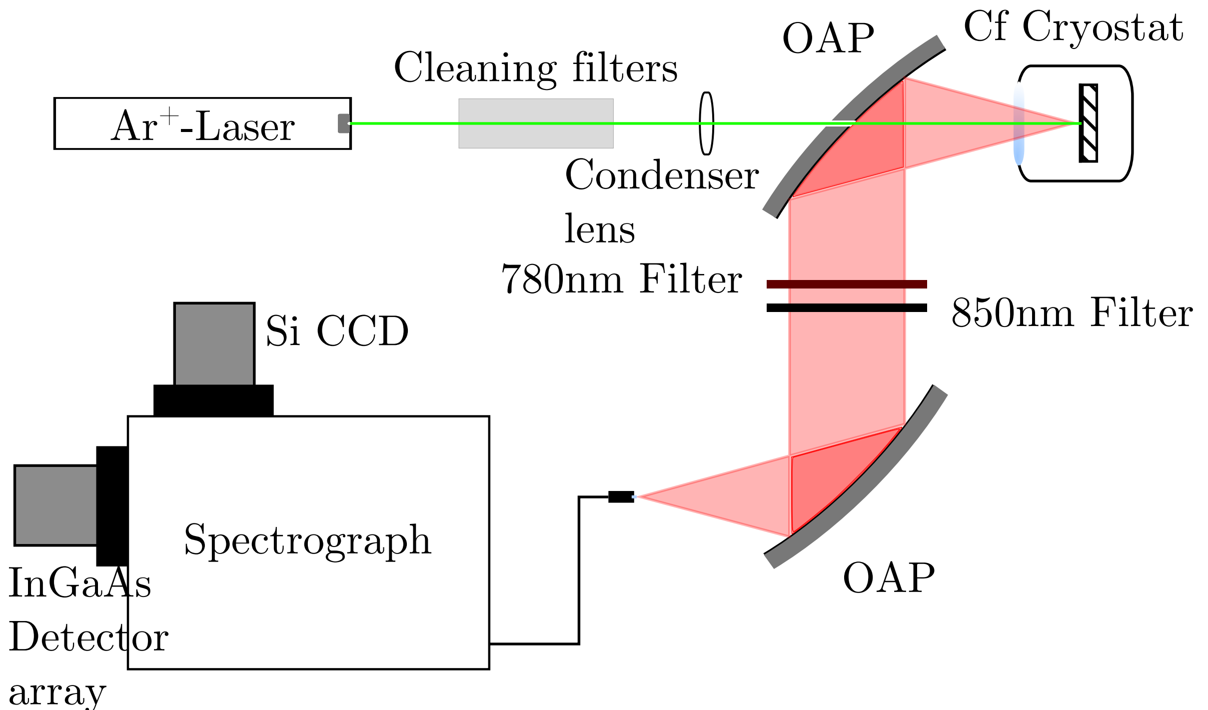

Figure 4.5.: Sketch of the PL setup.

Figure 4.5 shows a sketch of the setup, that was used to measure the PL emission of the epitaxial samples. For the excitation of the sample the 514.5 nm line of an Argon-ion laser is used. The laser light is cleaned by a set of filters to remove any parasitic emission from the plasma. The light is then focused with a condenser lens with a focal length of $f = 15$ cm, which results in a spot size of roughly 40 µm in radius as determined with a CMOS camera. The sample itself is mounted on a sample holder inside a continuous flow cryostat, which can be cooled to a temperature of 4.2 K with liquid helium. The PL signal from the sample is collected with an aluminium coated off axis parabolic (OAP) mirror and then guided through two color glass filters cutting off at 780 nm and 850 nm. In principle one filter is sufficient to completely remove the laser light from the signal. However, it was observed that the color glass filters produced a signal themselves at their cutoff wavelength, when illuminated by laser light. Therefore, the second color glass filter with the higher cutoff wavelength is used to remove any signal coming from

the first filter. The cleaned up signal is collected with a second OAP mirror and focused onto a glass fiber, which guides the light into an spectrograph. The spectrograph is equipped with several different diffractions gratings to spectrally resolve the light. In this work a grating with 100 lines/mm, blazed at 780 nm, was used. The spectrally resolved light is detected via an InGaAs array detector and a Si CCD camera.

At this point, the signal is still afflicted with non-idealities of the setup, as wavelength dependent response functions of the detectors or wavelength dependent transmission or reflection of the mirrors, the filters and the fiber. To obtain the true PL signal a halogen lamp with a known emission spectrum was measured with the setup. By comparing the measured spectrum with the true spectrum, a correction function was calculated. This correction function was then applied to the measured spectra to remove any setup-related artifacts.

4.3.2. Measurements

The PL emission of the samples was recorded at varying temperatures and varying excitation intensities. The minimum laser output power used in this work was 1 mW. With a laser sport size of 40 μm in radius and taking into account that roughly 60 % of the intensity are removed by the optical elements before the sample, this corresponds to a power density of roughly $8\,\mathrm{W/cm^2}$ on the sample. The power density scales linearly with the laser power.

To interpret the results of a PL measurement, it can be helpful to have an estimate of the density of generated charge carriers, which can then be compared to the doping concentration. The density of the generated charge carriers G can be estimated as:

$$G = \Phi \cdot \alpha \cdot \tau \tag{4.14}$$

Here Φ is the photon flux, α is the absorption coefficient and τ is the carrier life-time. The estimation is valid under the assumption that every absorbed photon creates an electron-hole pair, which does not move after its creation. The photon flux can be calculated from the power density on the sample. The absorption coefficient at a certain wavelength can be extracted from the dielectric function obtained by ellipsometry. The carrier life-time can be estimated by time-resolved photoluminescence, which was carried out by Mario Lang at the Karlsruhe Institute of Technology on some of the samples. This yielded an upper value for the carrier life-time of 1 ns. Using $\alpha \approx 10^6\,\mathrm{cm^{-1}}$, estimated from the dielectric function $\tilde{\varepsilon}$, results in $G \approx 10^{16}\,\mathrm{cm^{-3}}$ for the lowest excitation intensity at room temperature.

The PL behavior with increasing temperature differs significantly between the not annealed and the annealed samples. Furthermore, among the annealed samples two different types of behavior were observed. Among the not annealed samples, the disordered piece of 499 showed a different behavior.

In the following, the PL results of the annealed and the regular not annealed samples are presented separately by showing one example for each different type of behavior.

The interpretation of the measurement results are given in the subsequent section. The remaining samples are shown in appendix A.4 and the disordered piece of 499 will be discussed separately in section 4.3.5.

Not Annealed Samples

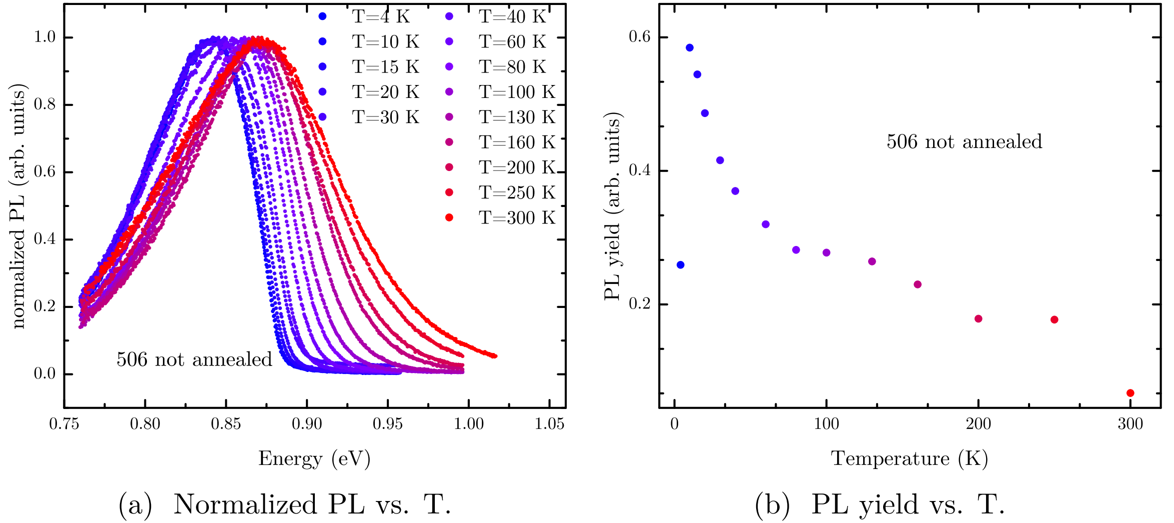

(a) Normalized PL vs. T.

(b) PL yield vs. T.

Figure 4.6.: Evolution of the PL of a not annealed sample with temperature. The spectra were taken at the same excitation intensity.

Figure 4.6a shows the evolution of the normalized PL signal of one not annealed sample with temperature. Each spectrum was recorded at the same excitation intensity. The evolution of the yield, obtained by integration, of the same spectra is shown in figure 4.6b and can be divided into two parts with different slopes: The first one ranging from the lowest temperature (excluding the point at 4 K) to 60 K and the second one, with a smaller slope, ranging from 60 K to 300 K. The PL emission exhibits a broadening of both the low and the high energy side and a blue-shift with increasing temperature between 40 K and 130 K. To quantify the broadening of the low energy side of the emission, it was fitted with [81]:

$$I_{\mathrm{PL}}(E) \propto \exp\left(-\frac{(E-E_0)^2}{2\gamma^2}\right) \tag{4.15}$$

This formula is originally used to describe the low energy side of the PL emission of a strongly compensated semiconductor governed by deep potential fluctuations at low excitation intensities. In that case γ is the average depth of the potential fluctuations and E_0 is the energy of the transition in the unperturbed semiconductor. It also describes the low energy side of a BI transition at low temperatures and excitation rates and of BT transitions [81]. However for the moment, before the emission is assigned to any recombination channel, γ is merely used as a means of quantification for the low energy side. The evolution of γ with increasing temperature is shown in figure 4.7, together

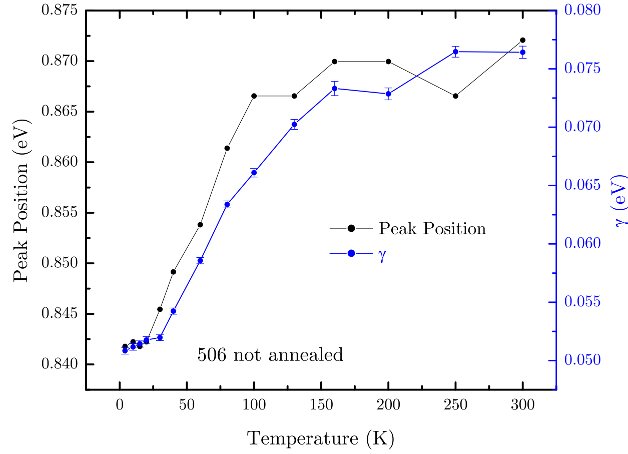

Figure 4.7.: Peak position and γ in dependence of the temperature for the not annealed sample.

with the position of the PL maximum. These two quantities show a clear correlation.

Figure 4.8a shows normalized PL spectra taken at 4 K and varying excitation intensities. From this plot it is visible that there is no significant change in shape or position of the emission with increasing excitation intensity. This behavior was observed at all temperatures, at which the sample was measured with different excitation intensities.

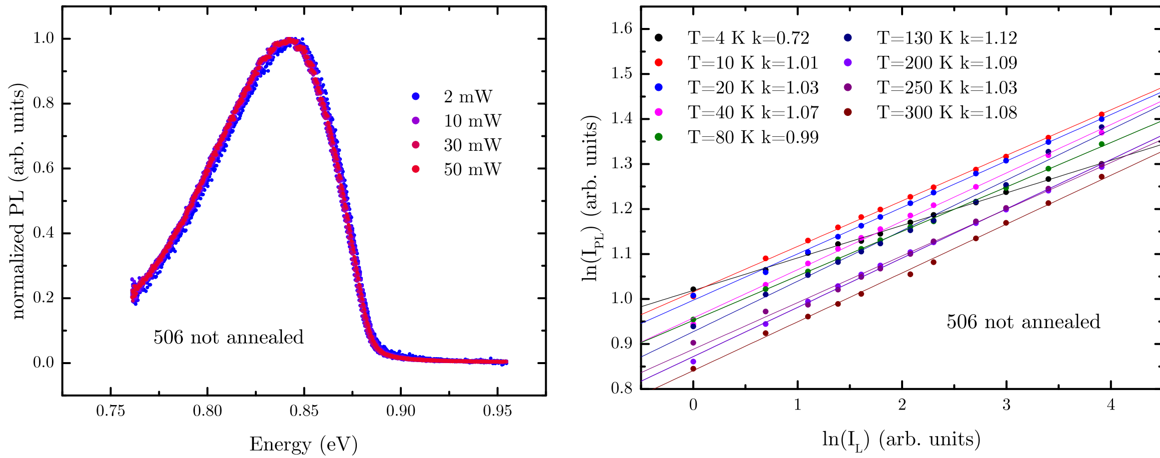

(a) Normalized spectra at $T = 10\,\mathrm{K}$ at different excitation intensities.

(b) K-values for different temperatures.

Figure 4.8.: Evolution of the PL of the not annealed sample with excitation intensity.

The intensity I_{PL} of the PL emission can in general be related to the excitation intensity I_{L} by a power law [80]:

$$I_{\mathrm{PL}} \propto I_{\mathrm{L}}^{k} \tag{4.16}$$

A plot of the natural logarithm of I_{PL} versus the natural logarithm of I_{L} is depicted in figure 4.8b. In this representation, the exponent k, or k-value, from equation 4.16 can

be extracted simply as the slope of a linear fit. As can be seen from figure 4.8b I_{PL} and I_{L} correlate linearly, except for the lowest temperature, at which $k = 0.72$. The fact that the PL emission increases slower with increasing excitation at $T = 4\,\mathrm{K}$ explains, why the corresponding data point in figure 4.6b does not follow the trend. A possible reason for this behavior is discussed in section 4.3.3.
In summary, the PL of the not annealed samples shows a blue-shift and a broadening of both the low and the high energy side with increasing temperature. With increasing excitation intensity, the peak position and the peak shape remain unchanged at all temperatures.

Annealed Samples

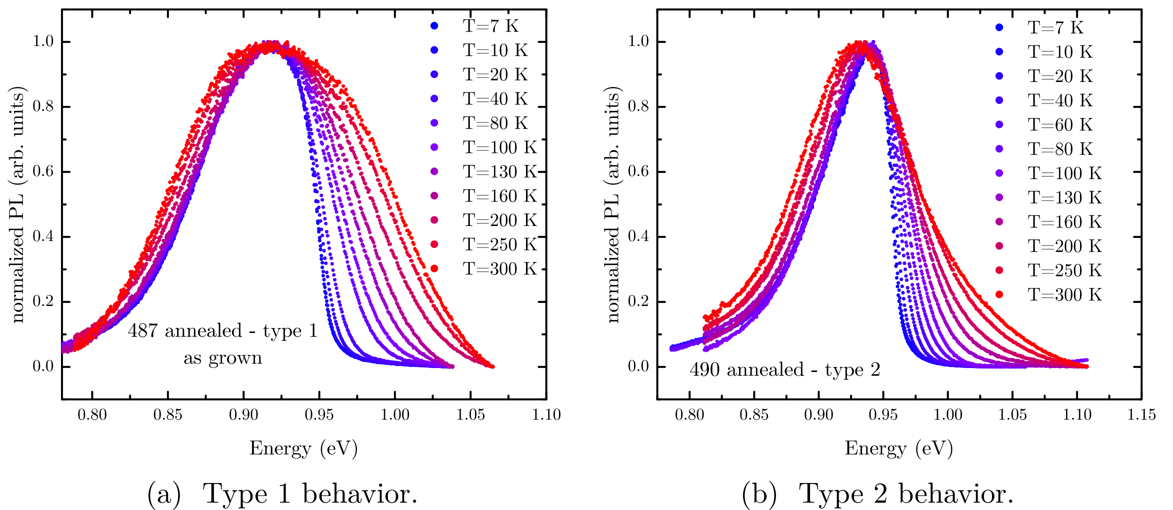

(a) Type 1 behavior.

(b) Type 2 behavior.

Figure 4.9.: Evolution of the PL shape with increasing temperature for two annealed samples showing different behaviors.

The evolution of the normalized PL emission with temperature is shown in figure 4.9. As mentioned above there are two different behaviors. The first one, labelled type 1 (figure 4.9a), shows a distinct broadening, beyond the expected thermal broadening, of the high energy side with increasing temperature. This broadening is not observed in the other samples, labelled type 2 (figure 4.9b). The low temperature emission of the type 2 sample is at slightly higher energies than that of the type 1 sample. There is not such a significant broadening of the low energy side or a large blue-shift with increasing temperature, as observed in the not annealed samples. Instead, both types of samples feature a small red-shift, which is visible as a shift of the low energy side towards lower energies.

Figure 4.10 shows the evolution of γ and the peak position with temperature for the two annealed samples. Note that the scales for both quantities are smaller compared to figure 4.7. At low temperatures the type 1 sample exhibits a small blue-shift of the emission, while γ increases slightly as well. At higher temperatures the blue-shift turns

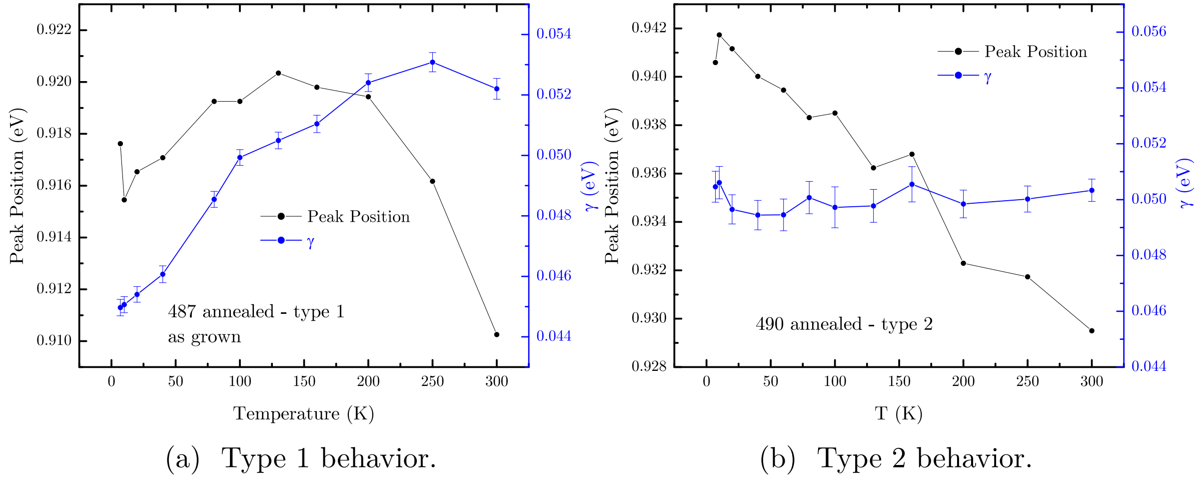

(a) Type 1 behavior. (b) Type 2 behavior.

Figure 4.10.: Peak position and γ in dependence of the temperature for the two annealed samples.

into a red-shift and γ begins to level off. In the type 2 sample only a red-shift is observed and γ remains virtually constant at all temperatures.

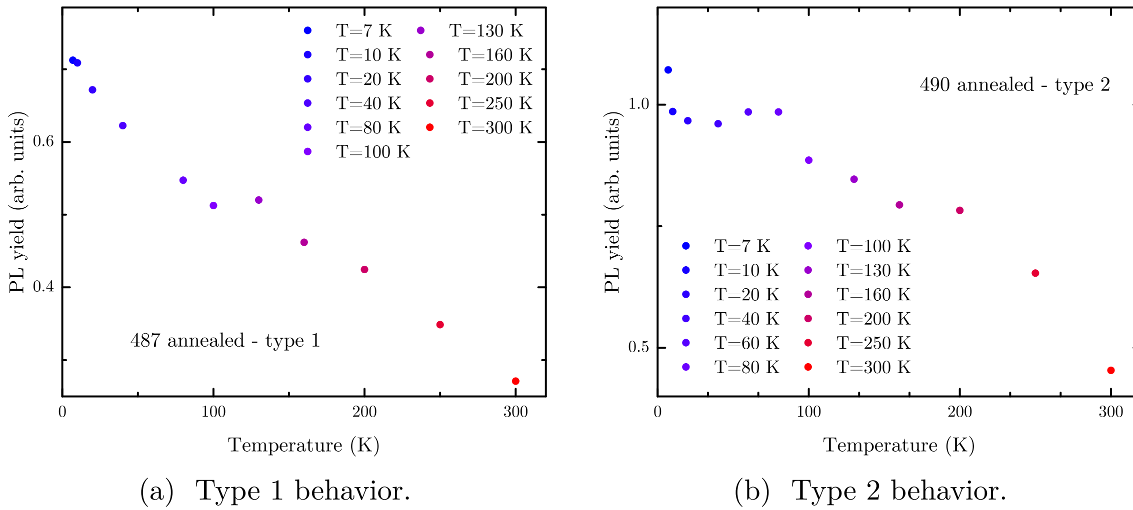

(a) Type 1 behavior. (b) Type 2 behavior.

Figure 4.11.: Evolution of the PL yield with increasing temperature for the annealed samples.

The evolution of the PL yield with temperature, shown in figure 4.11, is different from the not annealed samples as well. It decreases roughly linearly over the whole temperature range, as opposed to the stronger decrease at low temperatures in the not annealed samples. The total amount, by which the yield decreases from low temperatures to room temperature, is smaller in the annealed samples as well.

With increasing excitation intensity the PL yield grows linearly, which is reflected by k-values close to 1 for all probed temperatures, as shown in figure 4.12. As for the not annealed samples there is no visible change in the shape of the emission with increasing

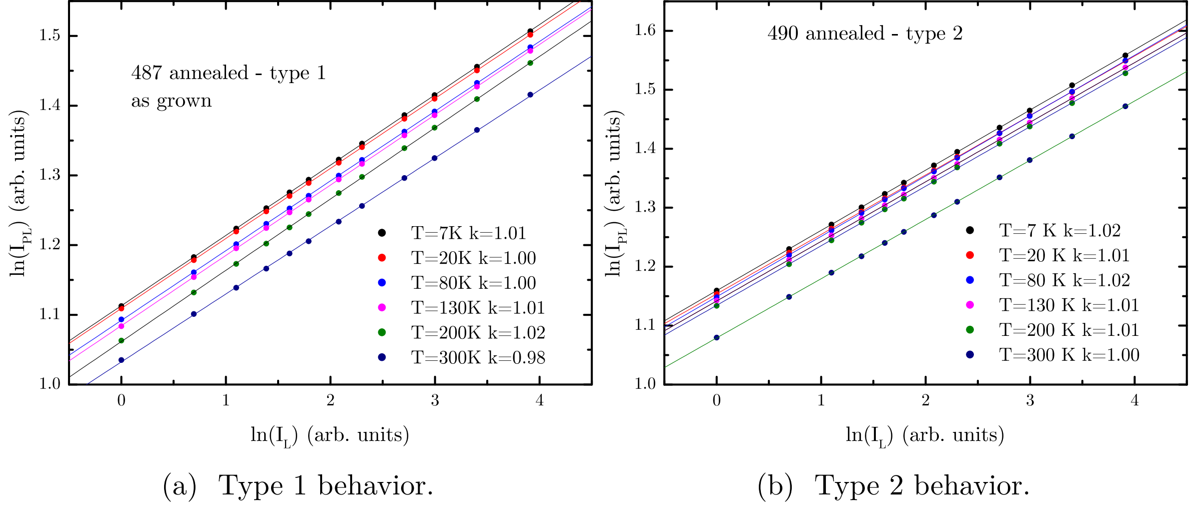

(a) Type 1 behavior.

(b) Type 2 behavior.

Figure 4.12.: K-values for the two annealed samples.

excitation.

4.3.3. Interpretation

The first step in the interpretation of the measurements is the attribution of the PL emission to a recombination channel. As was shown in section 2.4.5, Hall measurements determined the doping of one not annealed and one annealed sample to be p-type and the doping density to be of the order of $10^{20}\,\mathrm{cm}^{-3}$. The effective DOS of the valence band of CZTSe can be estimated by inserting the effective hole mass of the valence band into equation 2.9. Using an effective hole of $m_{\mathrm{v}}^{\mathrm{eff}} = 0.25 \cdot m_0$, as was calculated in section 4.2.1, yields an effective DOS of the valence band of $N_{\mathrm{V}} = 3.1 \cdot 10^{18}\,\mathrm{cm}^{-3}$ at 300 K. This value is lower than the doping level, which implies that the semiconductor is degenerate. In this case, the position of the Fermi-level F_{p} with respect to the valence band edge E_{V} can be estimated [91]:

$$\mu_p = E_{\mathrm{V}} - F_{\mathrm{p}} \approx k_{\mathrm{B}} T \left[\ln\left(\frac{p}{N_{\mathrm{V}}}\right) + 2^{-2/3}\left(\frac{p}{N_{\mathrm{V}}}\right) \right] \tag{4.17}$$

For $p > N_{\mathrm{V}}$ the difference μ_p is clearly positive. Using $p = 1 \cdot 10^{19}\,\mathrm{cm}^{-3}$, which is one order of magnitude below the doping level extracted from the Hall measurements, yields $\mu_p \approx 60\,\mathrm{meV}$. Based on this value, it can be assumed that F_{p} lies within the delocalized band states of the valence band. This justifies ignoring the influence of valence band tail states in the case of a fluctuating band structure, because the majority of the holes contributing to the PL emission originates from the free valence band states. Under the assumption that this applies to all the samples, the PL emission can be assigned in the following manner:

The not annealed samples show a BI transition in a fluctuating band structure at all temperatures. This attribution is made based on the blue-shift of the emission in

a confined temperature range, which is accompanied by an increase of γ in the same temperature range. The blue-shift is then due to a gradual filling of the BD states (see section 4.2.4) with increasing temperature. The broadening of the peak and especially the broadening of the low energy side reflects the fact that the range of states contributing to the PL emission increases, when the BD states are being made accessible through thermal energy. Both the blue-shift and the broadening level off at the same temperature, when all BD states are made accessible. This leveling off is characteristic for a BI transition.

Table 4.2.: Comparison of PL maximum and band gap determined by ellipsometry at room temperature for annealed and not annealed samples.

Sample	Annealed	$E_{\mathrm{PL}}^{\mathrm{max}}$ [meV]	$E_{\mathrm{G}}^{\mathrm{Ellips}}$ [meV]	ΔE_{PL} [meV]	PL behavior
499 as grown	no	859	929	70	-
499 ord. proc. 1	no	896	968	72	-
499 ord. proc. 2	no	878	934	56	-
503	no	862	933	71	-
506	no	872	920	48	-
486	yes	921	962	39	type 1
487 as grown	yes	910	957	47	type 1
487 ord. pro. 1	yes	984	-	-	type 1
490	yes	930	-	-	type 2
497	yes	911	-	-	type 2

The PL emission of the type 1 annealed samples shows a blue-shift and an increase of γ at low temperatures with increasing temperature as well. However, the increase of both quantities is smaller than in the case of the not annealed samples. Furthermore the emission at room temperature is at higher energies compared to the not annealed samples. The comparison of the PL maximum with the band gap $E_{\mathrm{G}}^{\mathrm{Ellips}}$, determined by ellipsometry, which is listed in table 4.2, shows that the difference ΔE_{PL} between these two quantities is generally slightly larger in the not annealed samples, except for the not annealed sample 506. The band gap $E_{\mathrm{G}}^{\mathrm{Ellips}}$, that was used for the calculation of ΔE_{PL} for sample 506, was taken from the model with the additional ZnSe-layer. The fact, that ΔE_{PL} is slightly larger in the not annealed samples and that the PL behaves in a different manner indicates, that the PL in the annealed samples does not originate from a BI transition. Instead it can, at low temperatures, be attributed to a BT transition in the type 1 samples, for which the carrier distribution is in a quasi-equilibrium and therefore it does not show a change in the peak shape with increasing excitation intensity. This implies that the temperature T_3 (see section 4.2.3) is smaller than 4 K for these samples. At elevated temperatures an additional BB transition becomes visible. The blue-shift at low temperatures can then be due to the inherent blue-shift of a BT transition or it can be due to the emerging BB peak. However, the fact that γ increases with the temperature as well indicates that the blue-shift is rather a result of the BB transition since it means that the range of states, that contribute to the emission, is growing.

This broadening of the low energy side would not be expected for a sole BT transition. The red-shift, which is observed at higher temperatures, can be explained by thermal narrowing of the band gap. It can be seen from the evolution of the low energy side in figure 4.9a that the red-shift becomes significant for temperatures above 130 K. This is in qualitative agreement with the temperature dependence of the band gap of CZTSe studied by Choi et al. with temperature dependent spectroscopic ellipsometry [92].

In the type 2 annealed samples, only a red-shift is observed while γ remains unchanged with increasing temperature. Based on these two observations, a BI-transition in these samples can be ruled out. Furthermore, there is no distinct broadening of the peak with increasing temperature, which indicates, that no second peak emerges at higher temperatures, as it is the case in the type 1 annealed samples. If the PL emission in these samples was due to a BT-transition, the fact that the peak shape does not change with increasing excitation intensity at all temperatures, indicates that the carrier distribution in the tails would be in a quasi-equilibrium, meaning that $T_3 < 4\,\mathrm{K}$ also for these samples. In this situation a blue-shift would be expected for a BT-transition with increasing temperature. However, only a red-shift is observed and the PL emission is therefore attributed to a sole BB transition. This attribution is further corroborated by the fact, that at low temperature the maximum of the emission is at higher energies, than in the type 2 annealed samples. The red-shift with increasing temperature in the type 1 annealed samples can then again be attributed to the thermal narrowing of the band gap.

The identification of the recombination channels responsible for the PL emission allows the extraction of more information about the samples. The most apparent statement to be made is that the PL of the not annealed samples shows the influence of a localized impurity level. This level is not observable in the annealed samples meaning that it is in some way influenced by the annealing stage during the growth process.

As explained in section 4.2.4, the low energy side of a BI transition at low temperatures and low rates of excitation, when only the TD states contribute to the emission, is determined by γ. This means that the value for γ obtained by fitting the low energy side can be used as a measure for the depth of the potential fluctuations. The results from the fit at the respective lowest measurement temperature are listed in table 4.3. The slightly zinc rich sample 506 (see table 2.1) has a γ of 51 meV at 4 K, while the sample 499, which is closer to stoichiometry shows $\gamma = 44\,\mathrm{meV}$ at the same temperature.

It is interesting to note that this value does not change, after this sample was subjected to the ordering procedure 1, while there is a significant increase in γ for the annealed sample 487 after being treated with the ordering procedure 2, as will be shown later. This point will be discussed in section 4.3.5.

The low temperature emission of the not annealed samples can also be used to estimate the ionization energy I_d of the defect DOS (see figure 4.2) by using equation 4.8. The exact values of Eg, which is the band gap defined by the percolation levels, at low temperatures is unknown. Therefore only an estimation for the ionization energy can be given based on the band gap determined by ellipsometry. This results in $I_\mathrm{d} \approx 100\,\mathrm{meV}$. Chen et al. studied lattice defects in CZTSe and reported two donor levels with ionization energies of around 100 meV, which are the $\mathrm{Zn_{Cu}}$ antisite and the $\mathrm{Cu_i}$ interstitial

[93]. As was described in section 2.3.2 annealing of CZTSe above the critical temperature of 200 °C increases the amount of $Cu_{Zn} + Zn_{Cu}$ antisites. Since the temperature during the growth stage is already much higher than this critical temperature, the additional annealing stage should, if anything, increase their density even further. The fact that the impurity level is not observed in the annealed samples suggests that it is not related to the Zn_{Cu} antisite. Instead it might be attributed to the Cu_i, which are removed by annealing under an excess Sn and Se atmosphere. However, this attribution should be treated with a lot of caution, since the majority of the samples is Cu-poor.

Lastly, the energy difference γ_e between the undistorted conduction band edge and the percolation level is equal to the magnitude of the blue-shift with increasing temperature of the BI-transition in the not annealed samples [81]. It was determined by calculating the difference between the maximum energy of the PL emission before and after the blue-shift of the not annealed samples. These results are listed in table 4.3 as well. It is worth noting that γ_e seems to correlate with with the fluctuation depth γ. This behavior is expected, because a larger γ indicates that the DOS penetrates deeper into the band gap and consequently, the percolation level lies at lower energies.

Table 4.3.: Average fluctuation depth γ determined at the lowest measurement temperature and γ_e for the not annealed samples.

Sample	Annealed	γ [meV]	γ_e [meV]
499 as grown	no	44	17
499 ord. proc. 1	no	44	20
506	no	51	30
487 as grown	yes	45	-
487 ord. proc. 2	yes	75	-
497	yes	54	-

In case of the type 1 annealed samples, that show a BT transition, the low energy side can also be fitted to determine γ. This works under the assumption that the BB transition does not have a significant influence on the slope at low temperatures. The fits yielded values between 45 meV and 54 meV for the as grown type 1 annealed samples (table 4.3), which is comparable to the not annealed samples. As mentioned earlier, the ordered piece of the type 1 annealed sample is an exception to this trend. Based on the values of γ, it appears that the annealing stage does not have an influence on the mechanism, that causes the fluctuating band structure.

Further information about the samples can be extracted from the observation that the k-value (equation 4.16) is 1 for all samples at every temperature, with the exception of the not annealed sample 506 at $T = 4\,\text{K}$. Figure 4.13 shows a simple system, containing a valence and a conduction band, which might also include tail states. The valence band already contains a certain amount of charge carriers described by the carrier density p_0. When the system is excited with light of a sufficiently high energy, additional charge carriers are generated in the bands, which are described with the charge carrier densities

n and p for electrons and holes in the conduction and valence band respectively. Under the assumption that every absorbed photon generates a electron-hole pair and that the light is absorbed completely, the generation rate G is proportional to the excitation intensity I_{exc}. At the same time the generated charge carriers will recombine radiatively giving rise to luminescence. Its intensity I_{PL} is proportional to the product of the total charge carrier densities in the two bands. Based on this, the rate equation, which describes the change in the carrier density with time for the conduction band, can be formulated as

$$\frac{dn}{dt} = G - C \cdot n(p + p_0), \tag{4.18}$$

where C is a proportionality constant, that contains the carrier life-time. Under steady-state conditions the carrier concentration remains constant with time, meaning that $\frac{dn}{dt} = 0$. Then equation 4.18 becomes:

$$I_{\text{PL}} \propto C \cdot n(p + p_0) = G \tag{4.19}$$

Since the PL intensity is proportional to the product of the total charge carrier densities, it is also proportional to the generation rate G and thereby to the excitation intensity I_{exc}. In other words, this two band system shows a k-value of 1.

In similar calculations it can be shown that the k-value decreases to 0.5 when one of the participating states is saturated (see [94] or [95]). In the same manner it can be shown that the k-value of the band-band transition drawn in figure 4.13 increases to 1.5, when an intermediate energy level, which is filled by capturing carriers from one of the two bands without thermal re-emission, is introduced in between the bands. As soon as this intermediate state is completely occupied, the k-value of the band-band transition goes back to 1.

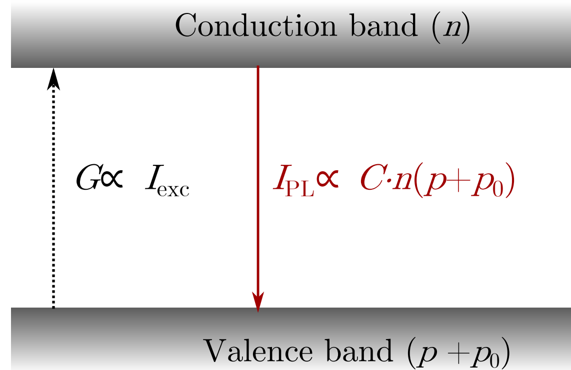

Figure 4.13.: System consisting of two bands with a doping charge carrier density p_0 in the valence band.

Transferring this to the measurements, it is clear that the PL emission comes from transitions between two states, which are not saturated, on both the annealed and the

not annealed samples. This implies that there is no visible influence of an intermediate state on the PL, which captures charge carriers from the involved states. This is in agreement with the findings of Weiss et al [96]., who studied the impact of different annealing procedures on the electronic structure of CZTSe. They found that samples, grown with a sequential process, exhibited a deep defect distribution within the band gap, while samples grown with a co-evaporation process similar to the ones used in this work, did not show this mid-gap defect level.

The k-value of around 0.7 for the not annealed sample at the lowest measurement temperature can be explained by the fact that one type of the participating states, probably the impurity states, gets close to saturation, because the rate of non-radiative recombination is sufficiently low at this temperature.

4.3.4. The Cause of the Fluctuating Band Structure

The PL measurement of the epitaxial CZTSe samples, presented in the previous sections, could successfully be described by a model containing a fluctuating band structure with localized tail states. Now the question arises, what the underlying cause of the fluctuating band structure is. It was shown in section 4.2.5 that, if the fluctuations were caused by randomly distributed charged defect clusters, they could be screened by additionally generated charge carriers with increasing excitation intensity. However, in the measurements presented so far no screening effects were observed. There are two possible reasons for this. The first one is that the observed fluctuating band structure is caused by band gap fluctuations, which cannot be screened by free charger carriers. The second reason is that the fluctuations are in fact caused by charged defect clusters but the excitation intensity, and consequently the density of the generated charge carriers, is so low, that a screening cannot be observed over the whole range of excitation intensities, which were used here.

Regarding the second option, it can be argued that the density of generated charge carriers at room temperature for the lowest excitation intensity is already roughly $10^{16}\,\mathrm{cm}^{-3}$ (see section 4.3.2) compared to a doping density of around $10^{20}\,\mathrm{cm}^{-3}$, as estimated based on the Hall measurements. At low temperatures the density of generated charge carriers is expected to be higher, because the carrier lifetime is higher as well at low temperatures [21]. Since the excitation intensity was increased by at least one order of magnitude it seems likely that any screening effects should be observable. Furthermore, one of the annealed samples (497), which exhibited a type 1 behavior in the first measurement, showed a small excitation dependency at low temperatures when re-measured. Figure 4.14a shows the normalized intensity series of this sample at 5 K. Now, the PL emission is more similar to a type 2 behavior and the low energy side becomes steeper and shifts towards higher energies with increasing excitation intensity[1]. The main part of the emission is then due to a BB transition while the varying low energy part can be attributed to a BT transition. Figure 4.14b shows the evolution of γ, obtained by fitting

[1]Note the increased range of intensity range compared to the previously shown measurements. The change in the peak shape is however visible from the lowest intensities on.

the low energy side of the PL emission, versus the laser power. This evolution was fitted with the function

$$\gamma = A \cdot I_{\text{exc}}^{-1/12}, \tag{4.20}$$

where A is an amplitude and I_{exc} is the excitation intensity. This formula reflects the dependency of the fluctuation depth on the charge carrier density in the case of screening (see equation 4.13) under the assumption, that $p \propto I_{\text{exc}}$ and that the dark carrier density can be neglected. The fitted curve is shown in figure 4.14b as well and it shows that γ in this case follows the expected dependency reasonably well, taking into account that the low energy side is influenced by the BB transition and that there are most probably free charge carriers, coming from the doping, present. Two conclusions can be drawn

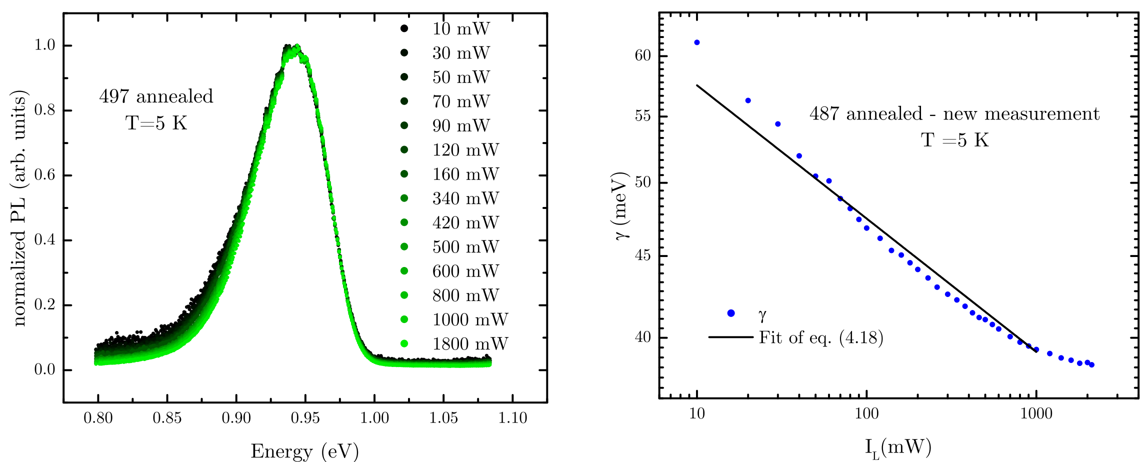

(a) Normalized PL for varying excitation intensities.

(b) γ versus excitation intensity and fit of equation 4.20.

Figure 4.14.: Excitation dependent PL in the annealed sample 497. The roughness of the PL spectra is an artifact from the correction function.

from this result. The first one is that this sample clearly shows the influence of potential fluctuations caused by randomly distributed charges. This is based on the reasonable description of the decrease of the low energy side with increasing excitation intensity by equation 4.20. The second conclusion is, that it is at least plausible to assume that, if there were any screening effects on the fluctuating band structure, they should be observable under the experimental conditions of this work. This means, by implication, that the samples, which do not exhibit any screening effects in the PL emission, are likely to be governed by band gap fluctuations. However, it should be noted that this does not exclude the existence of charged defect clusters. The high doping density implies, that they actually exist in the epitaxial samples. But at the same time, the high doping density and the absence of any screening effects with increasing excitation intensity suggest, that they are completely screened.

4.3.5. The Effect of the Ordering Procedures

There were two experimental indications that the ordering and the disordering procedures, as they were used in this work, appeared to have other effects on the epitaxial samples, besides the increasing or decreasing of the band gap.

In the first case, it was observed that the piece of the not annealed sample 499, which was treated with the disordering procedure, showed the highest band gap of all samples, as determined by ellipsometry (see table 3.3). This is contrary to what might be expected, when only the reduction of the density of the $Cu_{Zn} + Zn_{Cu}$ antisites due to the disordering is considered. Then the sample should have either the same band gap as the as grown piece or an even lower band gap. The former case would be expected, if the as grown sample was already completely disordered due to the high growth temperature. If the as grown sample was not completely disordered, the latter case, so a smaller band gap, would be expected.

The PL emission of this sample was also significantly different from all other samples, that were studied. Figure 4.15a shows the evolution of the normalized PL emission with temperature. The spectra were taken at the same excitation intensity. It can be seen, that the PL emission shows a red-shift with increasing temperatures at first. This red-shift turns into a blue-shift at elevated temperatures and at high temperatures a second peak at higher energies emerges. The second peak is at considerably higher energies, than the PL emission of the other not annealed samples at all temperatures. For clarity the evolution of the peak position of the low energy peak is plotted versus temperature in figure 4.15b. Furthermore, the low energy peak exhibits a blue-shift with increasing

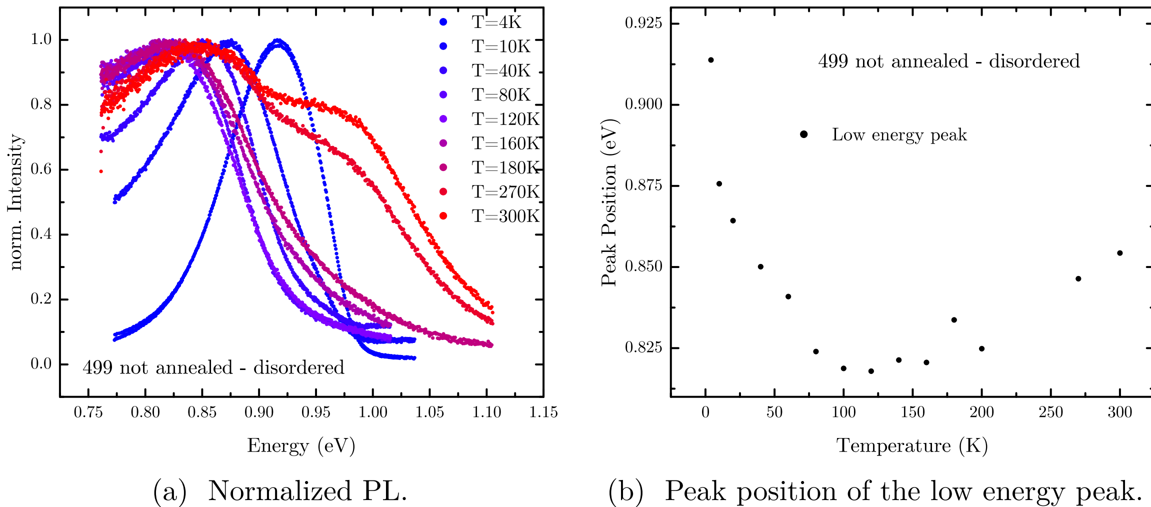

(a) Normalized PL. (b) Peak position of the low energy peak.

Figure 4.15.: Evolution of the PL emission of the not annealed disordered sample 499 with temperature.

excitation intensity, at least at low temperatures. This is shown for two temperatures in figure 4.16. At higher temperatures the low energy peak might be influenced by the high energy peak. Since the high energy peak is increasing at a higher rate, with increasing excitation intensity, than the low energy peak, it is not clear if the low energy

peak is still genuinely blue-shifting or if the change in its position is due to the growing influence of the high energy peak (figure 4.16b). This behavior is drastically different

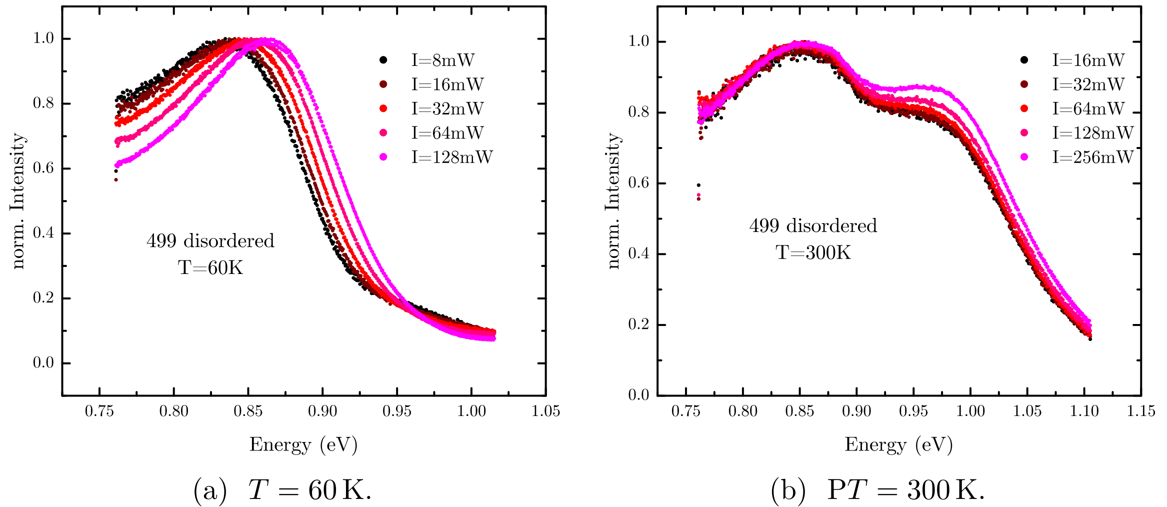

(a) $T = 60\,\mathrm{K}$.

(b) P$T = 300\,\mathrm{K}$.

Figure 4.16.: Evolution of the PL emission of the not annealed disordered sample 499 with excitation intensity at two different temperatures.

from the behavior of the other samples. It is especially different from the behavior of the BI-transition in the other not annealed samples. In fact the PL emission of this sample rather resembles a BT-transition with a BB-transition becoming visible at higher temperatures. Unlike the BT-transition of the annealed samples discussed previously, the distribution of the charge carriers within the localized tail states could be out of quasi-equilibrium at low temperatures, which could explain the red-shift with increasing temperatures and the blue-shift with increasing excitation intensities. It would also explain the blue-shift with increasing temperature from a certain temperature on. Even though this attribution of the PL emission should be treated with caution, because it is not obvious if the alleged BT-transition ceases to shift with increasing excitation intensity, as soon as it starts blue-shifting with increasing temperature, it is clear that this samples does not show a BI-transition. This leads to the conclusion that the dwell temperature of 250 °C during the disordering procedure is apparently high enough to remove the defect level found in the other not annealed samples.

The second case, where there ordering treatment seemed to have a more extensive effect, was the ordered piece of the annealed sample 487. It was shown in table 4.3 that the depth of the potential fluctuations of this sample appeared to have increased, after the sample was treated with the ordering procedure 2. This was not in accordance with the finding that γ remained constant in the not annealed sample 499, after it was subjected to the ordering procedure 2.

To check, whether the increase in γ in the ordered annealed sample 487 is due to a genuine influence of the ordering procedure on the fluctuation depth, figure 4.17 shows the normalized PL spectra of the as grown and the ordered piece of the annealed sample

487 on a logarithmic scale. From this plot it is apparent that the emission of the ordered specimen is considerably broader than that of the as grown one. Furthermore, the low energy side of the ordered PL overlaps almost completely with the as grown PL. A small kink in the low energy slope between 0.85 eV and 0.90 eV indicates that there might actually be a peak at the same position as the PL of the as grown sample.

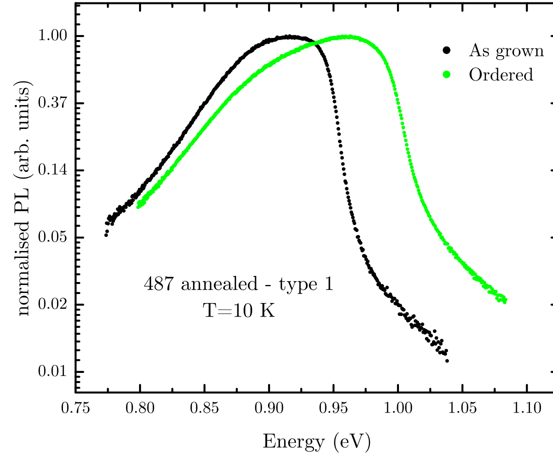

Figure 4.17.: PL spectra of the as grown and ordered parts of the annealed sample 487 at $T = 10\,\mathrm{K}$.

This can be explained in the following manner. In the case of the not annealed sample 499, it was found that the ordering procedure 1 led to a higher increase of the band gap, as determined by ellipsometry, than the ordering procedure 2 (see table 3.3). As indicated by the small kink in the ordered spectrum of figure 4.17, the ordering procedure 2 is less efficient than the ordering procedure 1 such, that it apparently leaves some areas of the sample in the as grown state. The broadening of the low energy side of the ordered spectrum is then more likely to be the result of the overlapping of two peaks: One coming from the areas of the sample, which were unaffected by the ordering and a second one coming from the ordered areas of the sample. Consequently, the apparent increase in γ for the annealed sample 487, after the ordering procedure was applied, is not due to a genuine change in the fluctuation depth. In the case of the not annealed sample 499, the ordering procedure 1 was more efficient and therefore no change in γ is observed in the ordered species. This is an indication that a change in the $\mathrm{Cu_{Zn}} + \mathrm{Zn_{Cu}}$ antisite density, even though it does change the band gap, as was confirmed by ellipsometry, does not significantly change the average depth of the band gap fluctuations.

4.3.6. Summary

In the previous sections the PL emission of the epitaxial CZTSe samples could successfully be described by a model containing a fluctuating band structure with localized tail states. The PL of the not annealed samples could be attributed to a BI transition while the PL of the annealed samples could be explained by a combination of BT and BB

transitions. The analysis of the low temperature emission yielded an average fluctuation depth of 44 meV to 54 meV, which did not seem to be affected by the annealing stage during the growth. The PL of the not annealed samples indicated that an ordering procedure does not influence the average fluctuation depth as well. This led to the conclusion that the $Cu_{Zn} + Zn_{Cu}$ defect clusters, even though they affect the band gap energy, do not contribute significantly to the average depth of the fluctuating band structure, which is likely to be caused by band gap fluctuations.

Furthermore, it was found that the disordering procedure led to a significant change in the PL behavior of one not annealed sample, which indicated that the defect level, that was involved in the BI-transition in the other not annealed samples, was removed.

It was shown that the PL yield increased linearly with the excitation energy at essentially all temperatures for all samples. From this it was deduced that the PL is not influenced by a mid-gap state, which was reported for CZTSe grown by a sequential process [96].

5. Conclusion

Summary

The aim of this work was to produce epitaxial CZTSe thin films in order to be able to study the material properties without the influence of grain boundaries. The samples were made by high temperature co-evaporation using two different processes. One containing an in-situ annealing stage and a second one, where this annealing stage was omitted. X-ray diffraction confirmed the mono-crystallinity of both types of samples and Raman spectroscopy could not detect any traces of secondary phases on the surface of a multitude of the samples. However, Hall measurements indicated that the samples have a very high doping density up to the point of degeneracy.

The films were studied in detail with spectroscopic ellipsometry and temperature and excitation dependent photoluminescence spectroscopy. The PL measurements showed that the samples can be described with a fluctuating band structure containing localized tail states, which is probably caused by band gap fluctuations with an average fluctuation depth of $45 - 55\,\mathrm{meV}$ for both the annealed and the not annealed samples. Fluctuations due to randomly distributed defect clusters can most likely be excluded as the underlying reason because the majority of samples did not show any screening effects with increasing excitation intensity. Furthermore, the high doping density suggests that these electrostatic potential fluctuations are screened by the free doping charge carriers, so they cannot be observed. Only one spot of the annealed sample 497 showed a change of the shape of the PL emission with increasing excitation intensity upon re-measurement, which could be described by screening effects.

It was shown that the not annealed samples contain a defect level, which gave rise to the BI-transition, which was visible even at room temperature. This defect level is apparently removed by the in-situ annealing stage, because the PL of the annealed samples showed only BT- and BB-transitions.

From the evolution of the PL yield with excitation intensity it could be concluded that both the annealed and the not annealed samples do not have an intermediate defect level within the band gap, which captures carriers from one of the bands. Otherwise the BI-transitions in the not annealed and the BT- and BB-transitions in the annealed samples would not scale linearly with the excitation intensity.

Ellipsometry measurements showed that the in-situ annealing stage leads to a slight increase of the band gap, compared to the not annealed samples. They also confirmed that two different ordering procedures, applied to not annealed and annealed samples, resulted in the expected increase of the band gap. At the same time, it was observed from the PL measurements on these ordered samples that the average fluctuation depth of

these samples was not influenced by the ordering treatment. This led to the conclusion, that the density of the Cu_{Zn}+Zn_{Cu} antisites, which is reduced by the ordering procedures, does influence the band gap energy. However, it does not seem to have an influence on the average fluctuation depth. Consequently, these antisite clusters are probably not the underlying reason for the band gap fluctuations, which were observed here.

Lastly, it was found that the disordering procedure caused a significant change in the electronic structure of the not annealed sample 499. This was concluded from the fact, that this sample showed the highest band gap of all samples in ellipsometry. The PL emission of this sample was more similar to the annealed samples than it was to the other not annealed samples. This showed that the defect level, which was observed in the not annealed samples, was removed by the ordering procedure.

Outlook

With this work it was demonstrated that CZTSe without grain boundaries and without apparent amounts of secondary phases can be produced by molecular beam epitaxy. However, their doping density of $10^{20}\,\mathrm{cm}^{-3}$ is roughly four orders of magnitude higher than the doping level of around $10^{16}\,\mathrm{cm}^{-3}$ of the absorber layers used in CZTSe-based solar cells [97]. In order to make the epitaxial samples more comparable to these absorber layers, the growth process obviously needs adjusting. It was seen that the disordering procedure increased the band gap energy of a not annealed sample to 1.06 eV. This could not be achieved with the in-situ annealing stage. In addition to that, the PL emission of this sample probably showed a BB-transition. The disordering procedure consisted of an annealing under vacuum at 250 °C. This suggests that a systematic study of the in-situ annealing stage might be useful to investigate the influence of the Sn- and Se-atmosphere during this stage.

As it was mentioned in the introduction of this thesis, the main limiting factor for the conversion-efficiency of CZTS(e)-based solar cells is currently the high V_{OC}-deficit, which is at least in parts caused by band tail states. It was shown that the fluctuating band structure of the epitaxial and consequently the tail states, which come with this structure, are very likely to be caused in large parts by band gap fluctuations. The fact that their fluctuation depth remained unchanged, when the density of the $Cu_{Zn} + Zn_{Cu}$ antisites was reduced by ordering procedures, indicates that those antisites do not play a significant role for the band gap fluctuations. This implies that other mechanisms for the formation of the band tails in CZTSe need to be considered.

A. Appendix

A.1. Detailed XPS Scans

506 not annealed

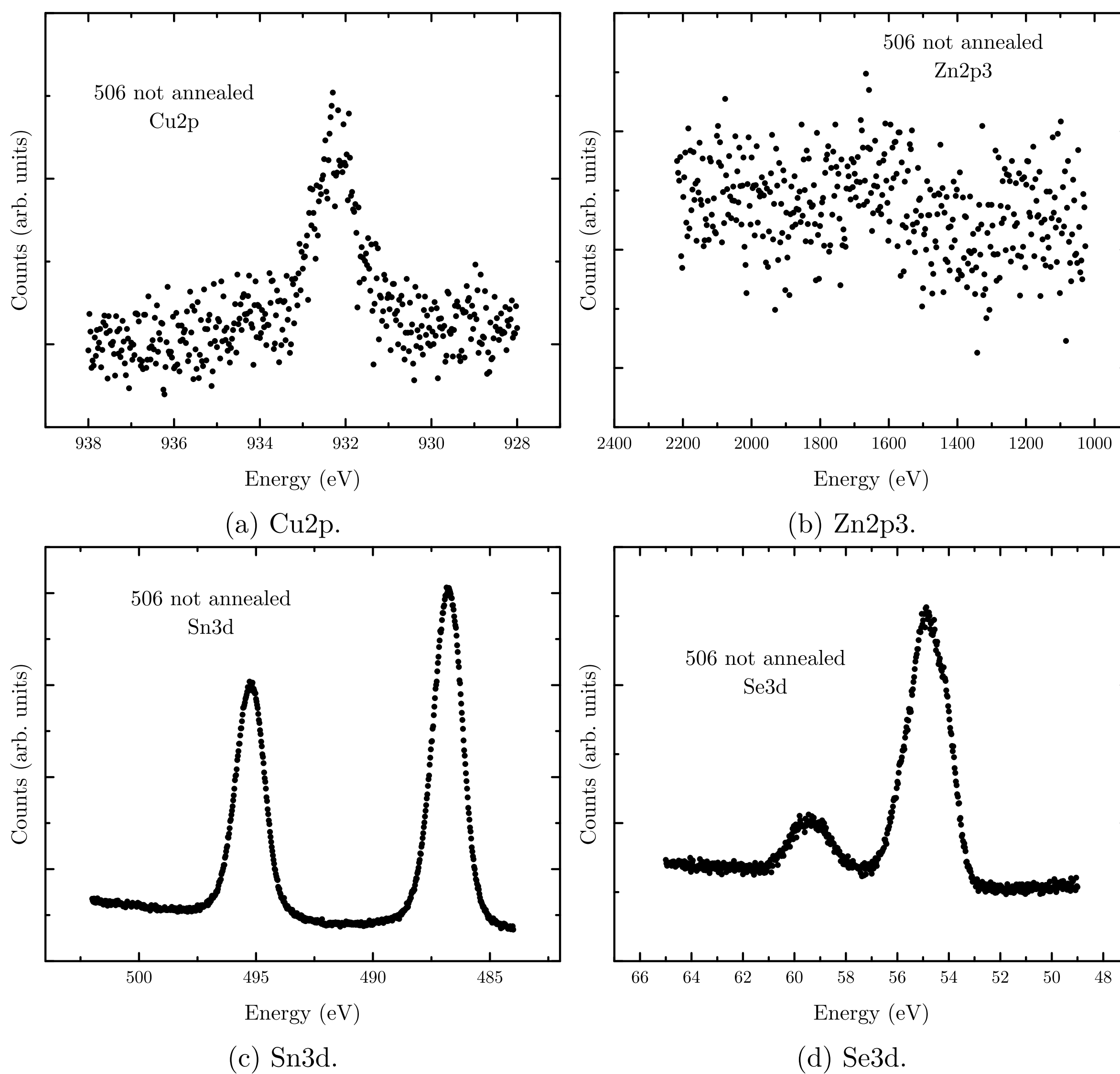

(a) Cu2p.

(b) Zn2p3.

(c) Sn3d.

(d) Se3d.

Figure A.1.: 506 not annealed.

487 not annealed

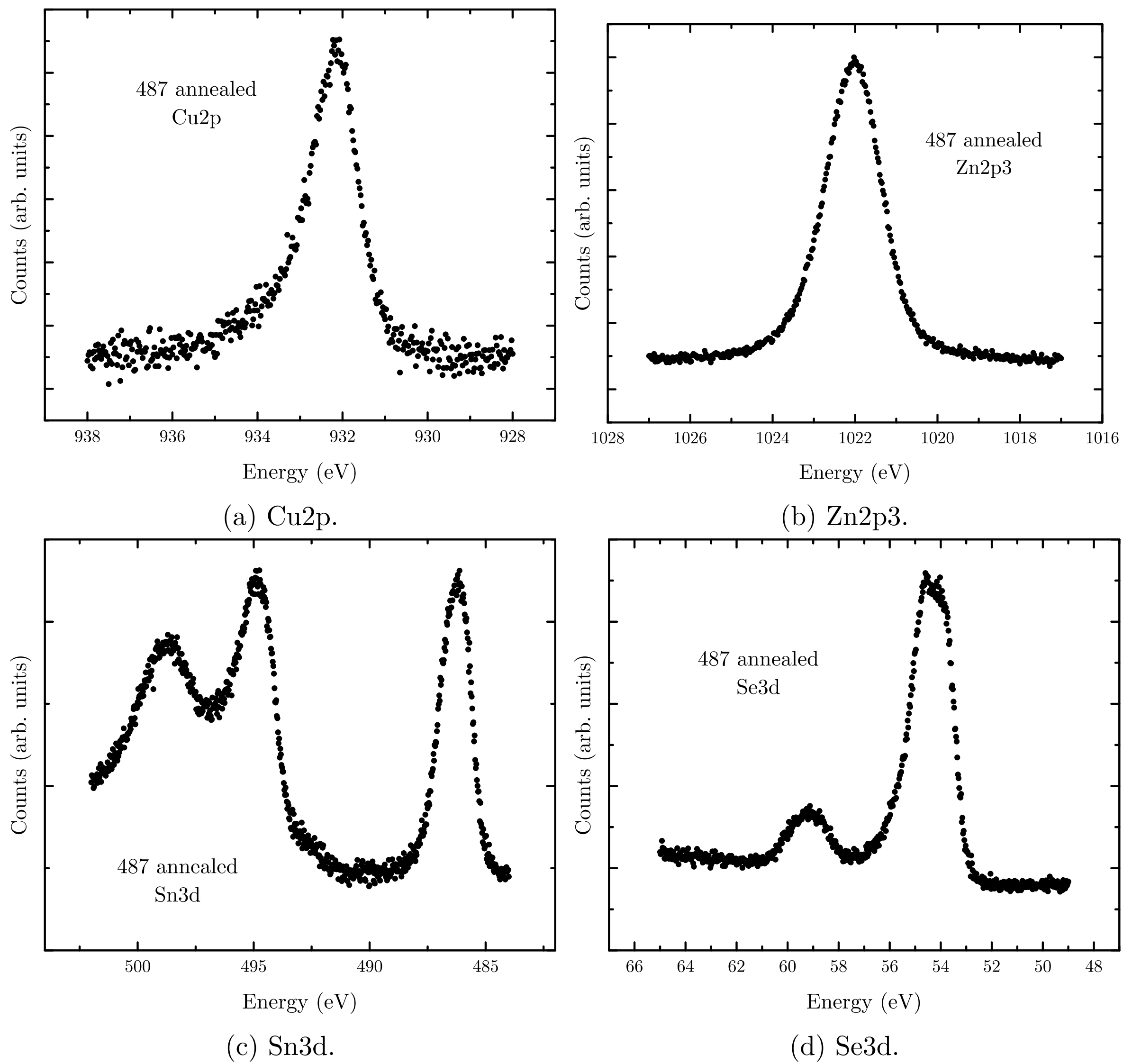

(a) Cu2p.

(b) Zn2p3.

(c) Sn3d.

(d) Se3d.

Figure A.2.: 487 annealed.

A.2. Fits of the Models to the Ellipsometric Parameters

If not stated otherwise, the models contain the additional ZnSe-layer.

A.2.1. Not annealed samples

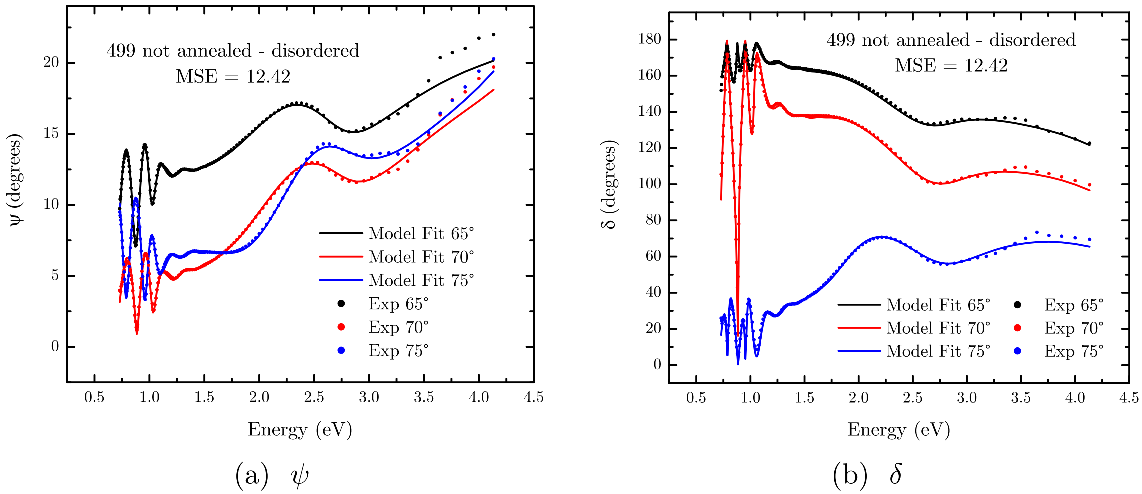

(a) ψ (b) δ

Figure A.3.: Model fit for the not annealed sample 499, treated with the disordering procedure.

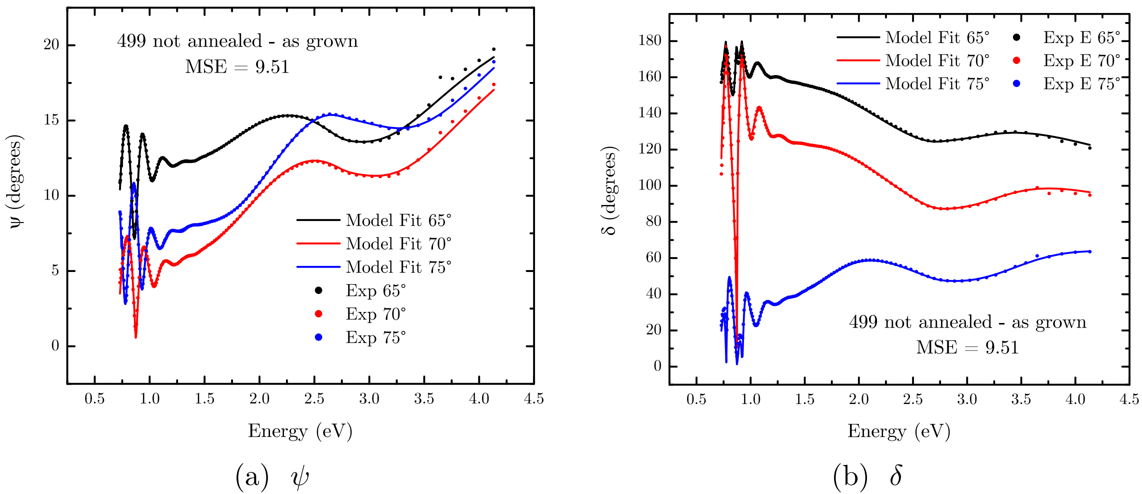

(a) ψ (b) δ

Figure A.4.: Model fit for the not annealed, as grown sample 499.

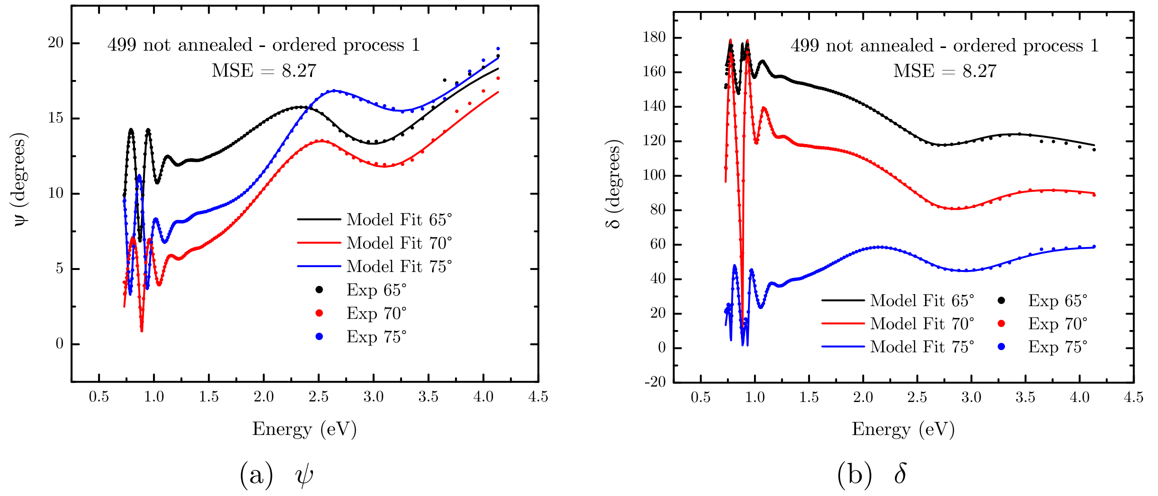

(a) ψ (b) δ

Figure A.5.: Model fit for the not annealed sample 499, treated with ordering process 1.

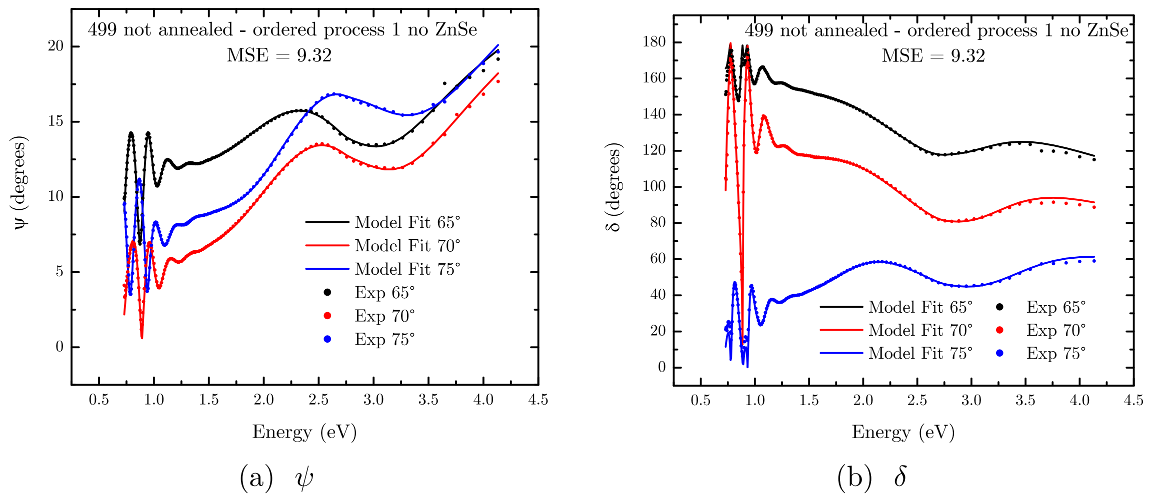

(a) ψ (b) δ

Figure A.6.: Model fit for the not annealed sample 499, treated with ordering process 1, without the additional ZnSe layer in the model.

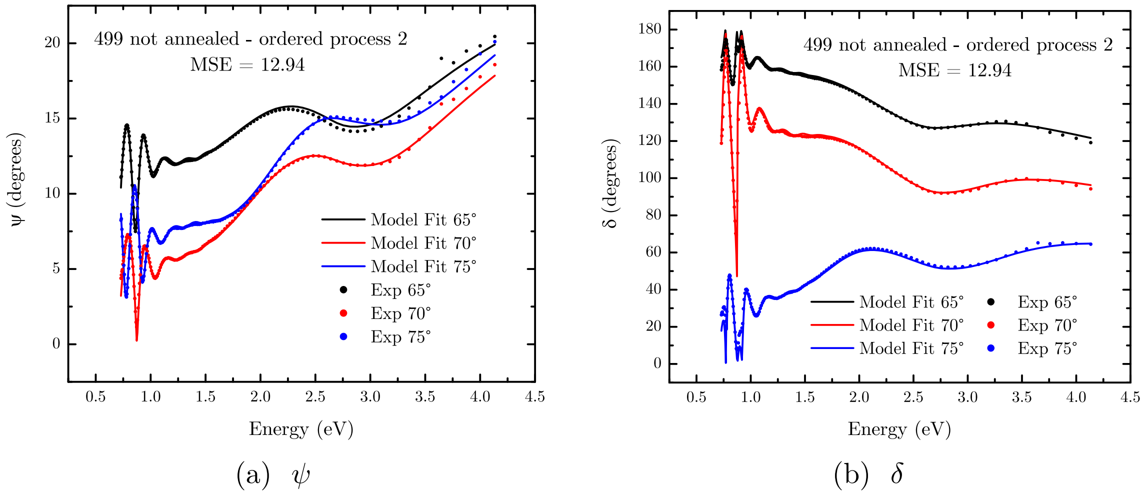

Figure A.7.: Model fit for the not annealed sample 499, treated with ordering process 2.

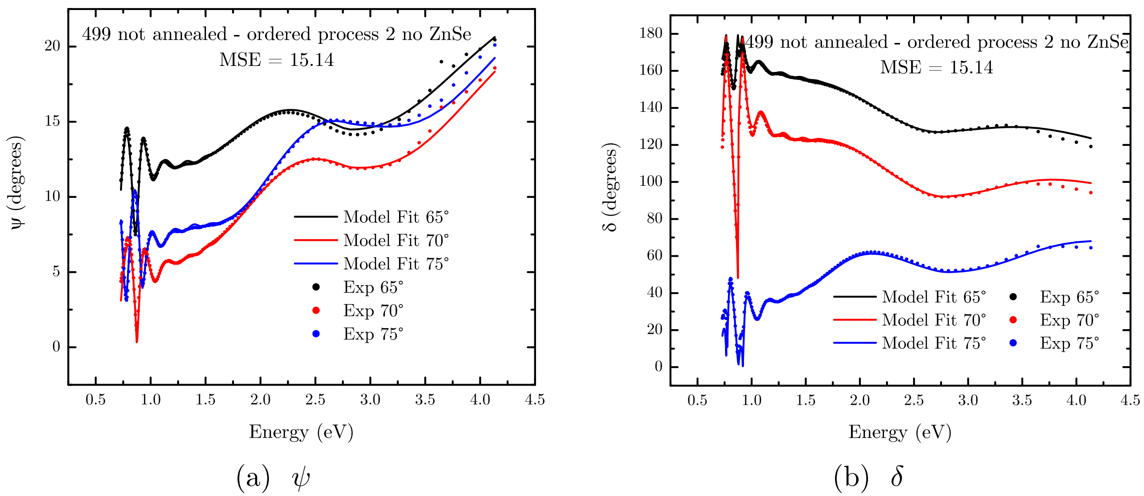

Figure A.8.: Model fit for the not annealed sample 499, treated with ordering process 2, without the additional ZnSe layer in the model.

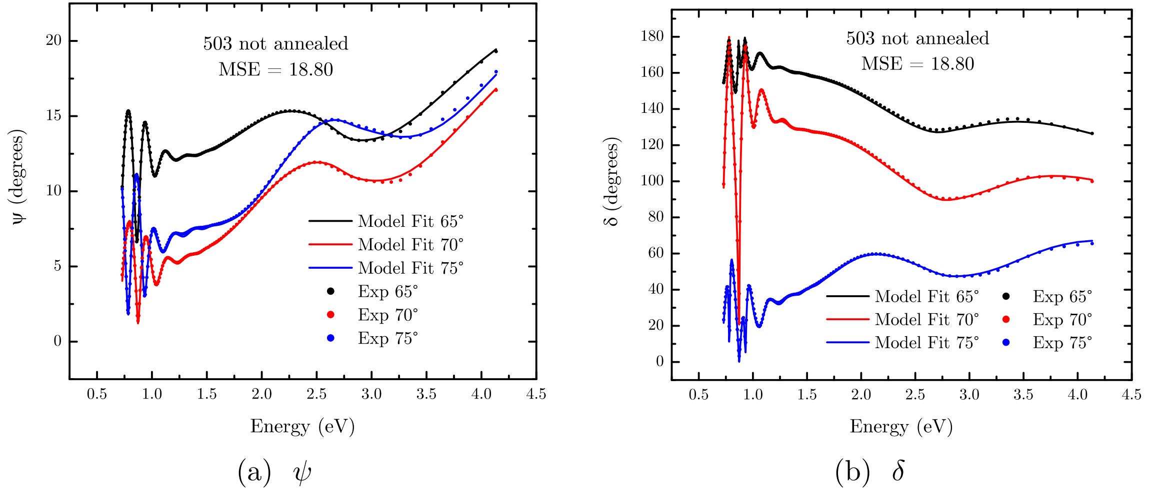

(a) ψ (b) δ

Figure A.9.: Model fit for the not annealed sample 503.

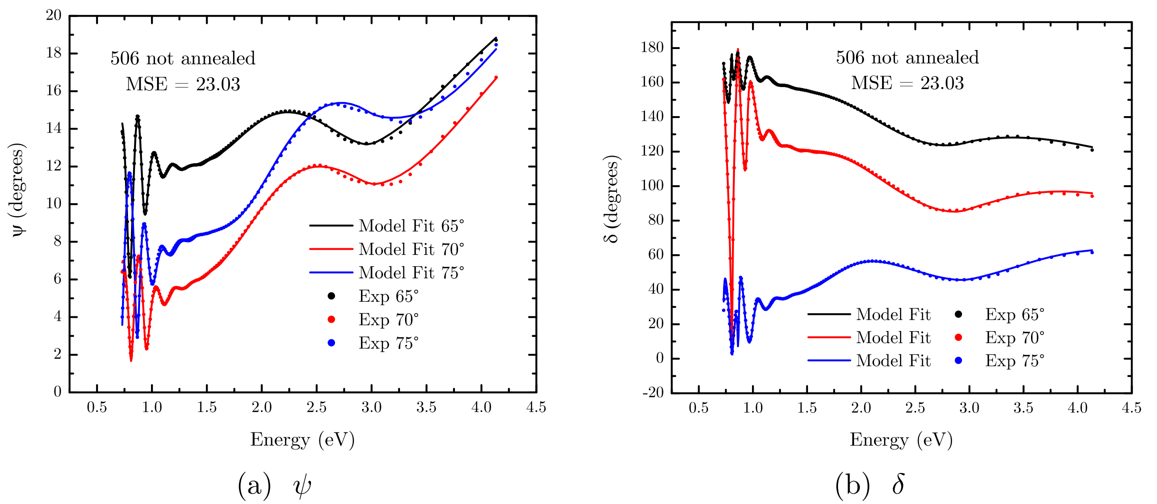

(a) ψ (b) δ

Figure A.10.: Model fit for the not annealed sample 506.

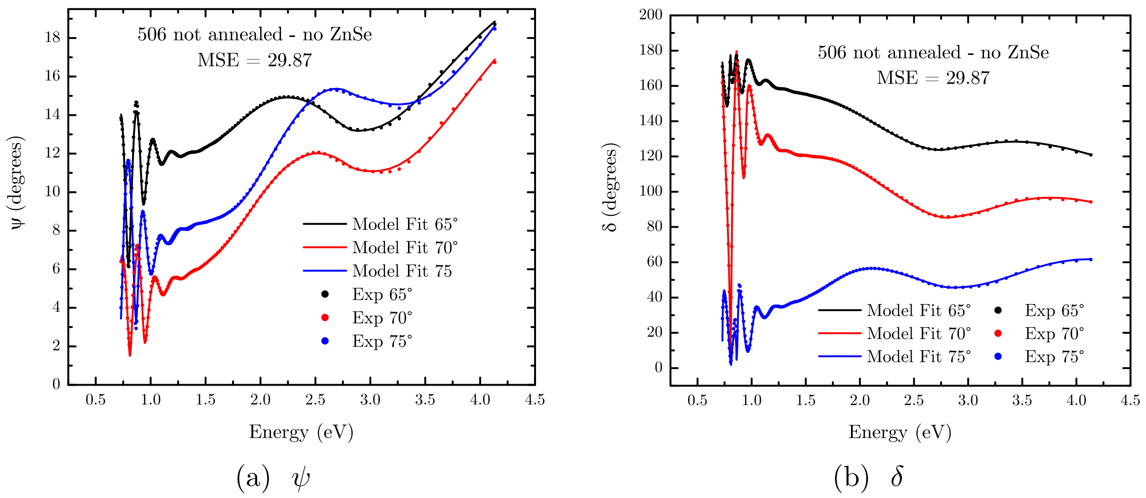

(a) ψ

(b) δ

Figure A.11.: Model fit for the not annealed sample 506, without the additional ZnSe layer in the model.

A.2.2. Annealed Samples

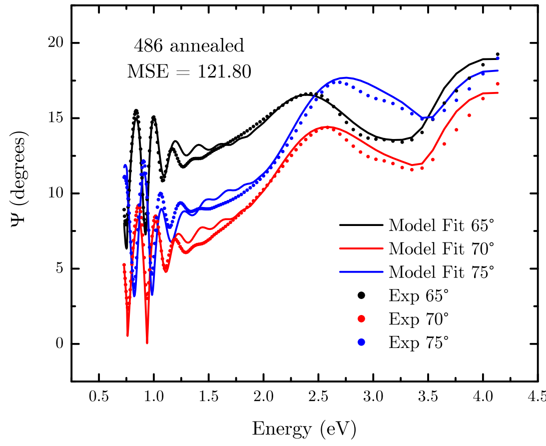

(a) ψ

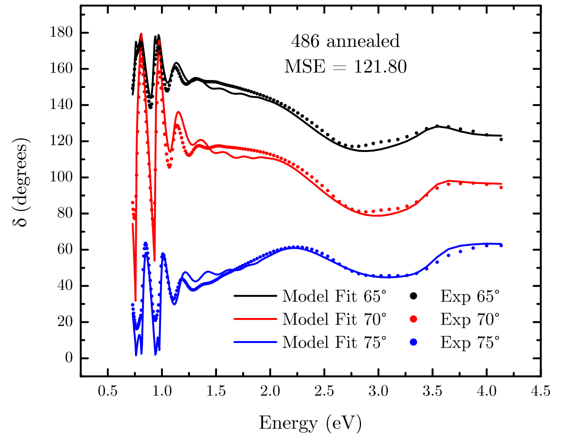

(b) δ

Figure A.12.: Model fit for the annealed sample 486.

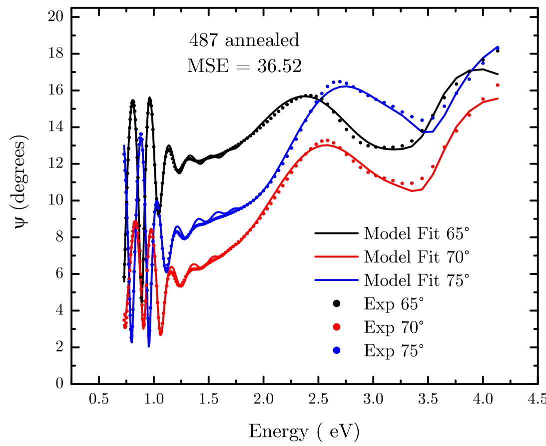

(a) ψ

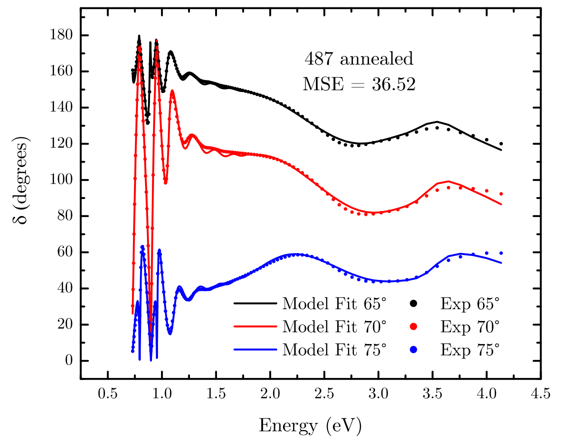

(b) δ

Figure A.13.: Model fit for the annealed sample 487.

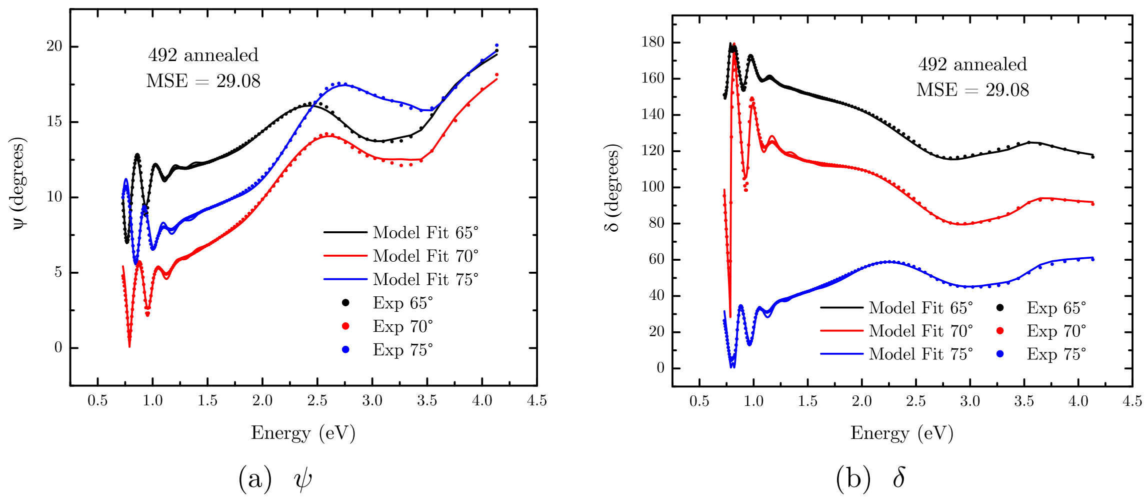

(a) ψ

(b) δ

Figure A.14.: Model fit for the annealed sample 492.

A.3. Fits of the Second Derivative Spectra of $\tilde{\varepsilon}$

Fits of the second derivative spectra around the critical points (CP). The plots contain the adjusted r-square value, which is calculated by Origin to estimate the goodness of the fits.

499 not annealed with ZnSe

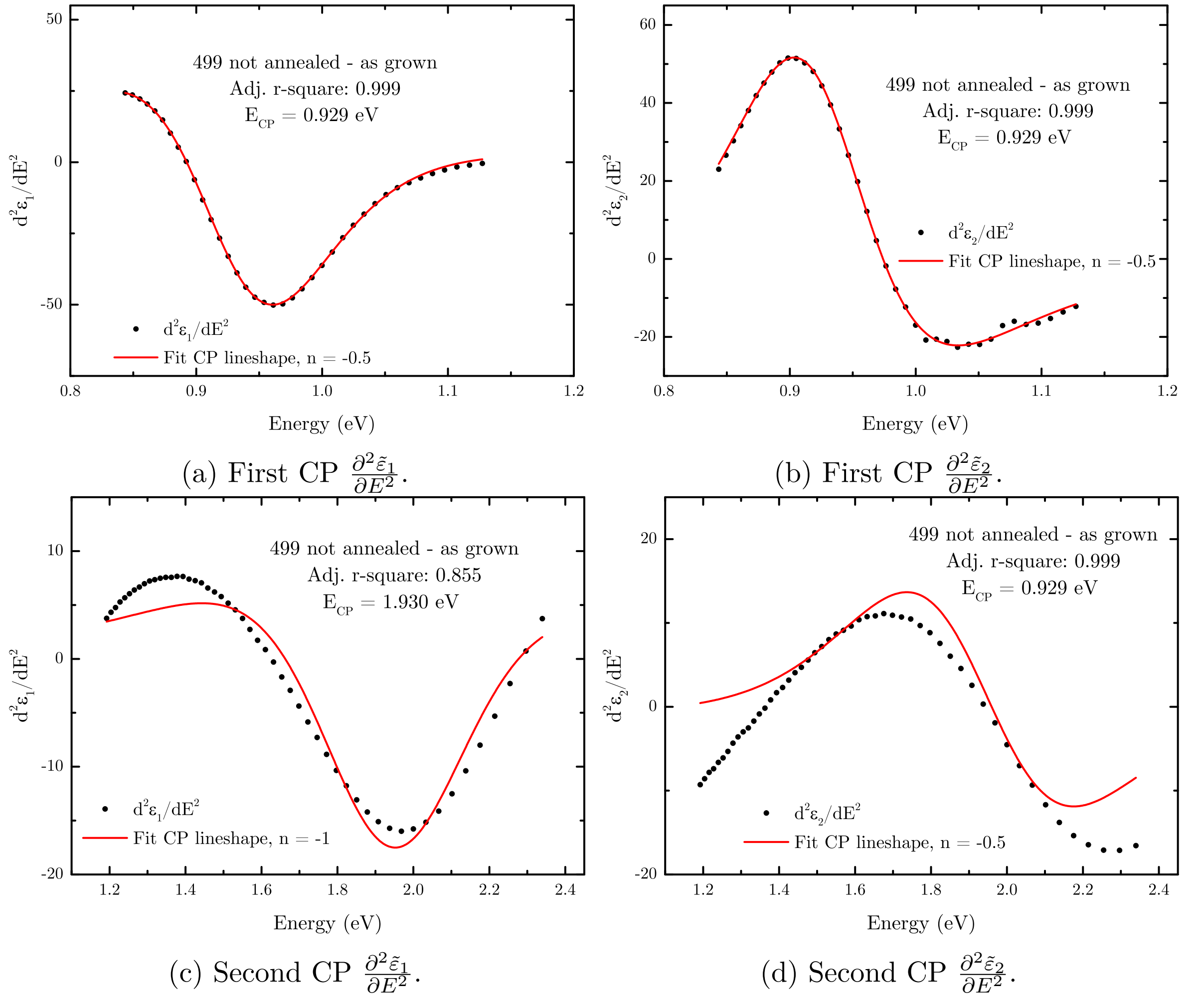

(a) First CP $\frac{\partial^2 \tilde{\varepsilon}_1}{\partial E^2}$.

(b) First CP $\frac{\partial^2 \tilde{\varepsilon}_2}{\partial E^2}$.

(c) Second CP $\frac{\partial^2 \tilde{\varepsilon}_1}{\partial E^2}$.

(d) Second CP $\frac{\partial^2 \tilde{\varepsilon}_2}{\partial E^2}$.

Figure A.15.: 499 not annealed, as grown.

499 not annealed disordered with ZnSe

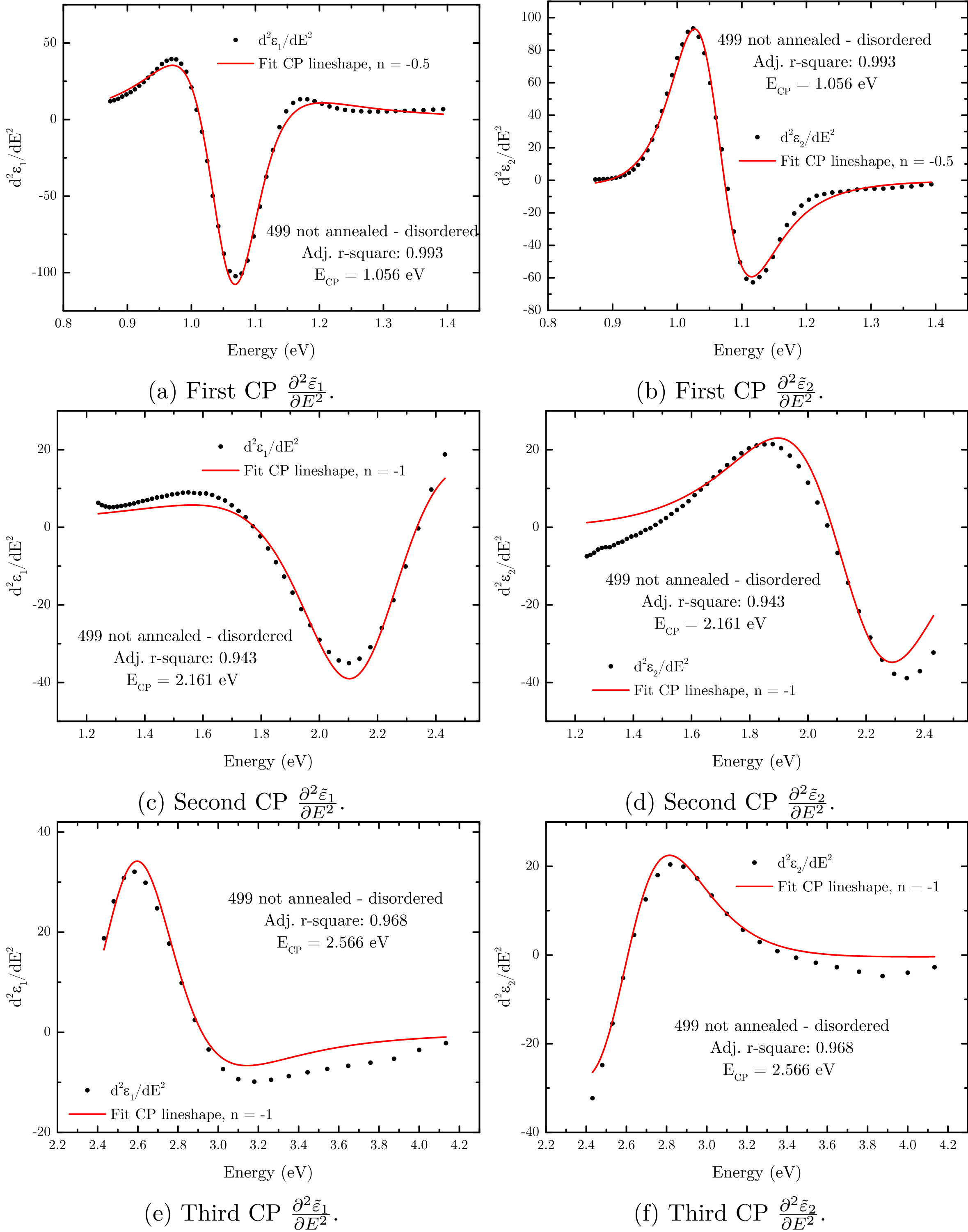

(a) First CP $\frac{\partial^2 \tilde{\varepsilon}_1}{\partial E^2}$.

(b) First CP $\frac{\partial^2 \tilde{\varepsilon}_2}{\partial E^2}$.

(c) Second CP $\frac{\partial^2 \tilde{\varepsilon}_1}{\partial E^2}$.

(d) Second CP $\frac{\partial^2 \tilde{\varepsilon}_2}{\partial E^2}$.

(e) Third CP $\frac{\partial^2 \tilde{\varepsilon}_1}{\partial E^2}$.

(f) Third CP $\frac{\partial^2 \tilde{\varepsilon}_2}{\partial E^2}$.

Figure A.16.: 487 annealed.

503 not annealed with ZnSe

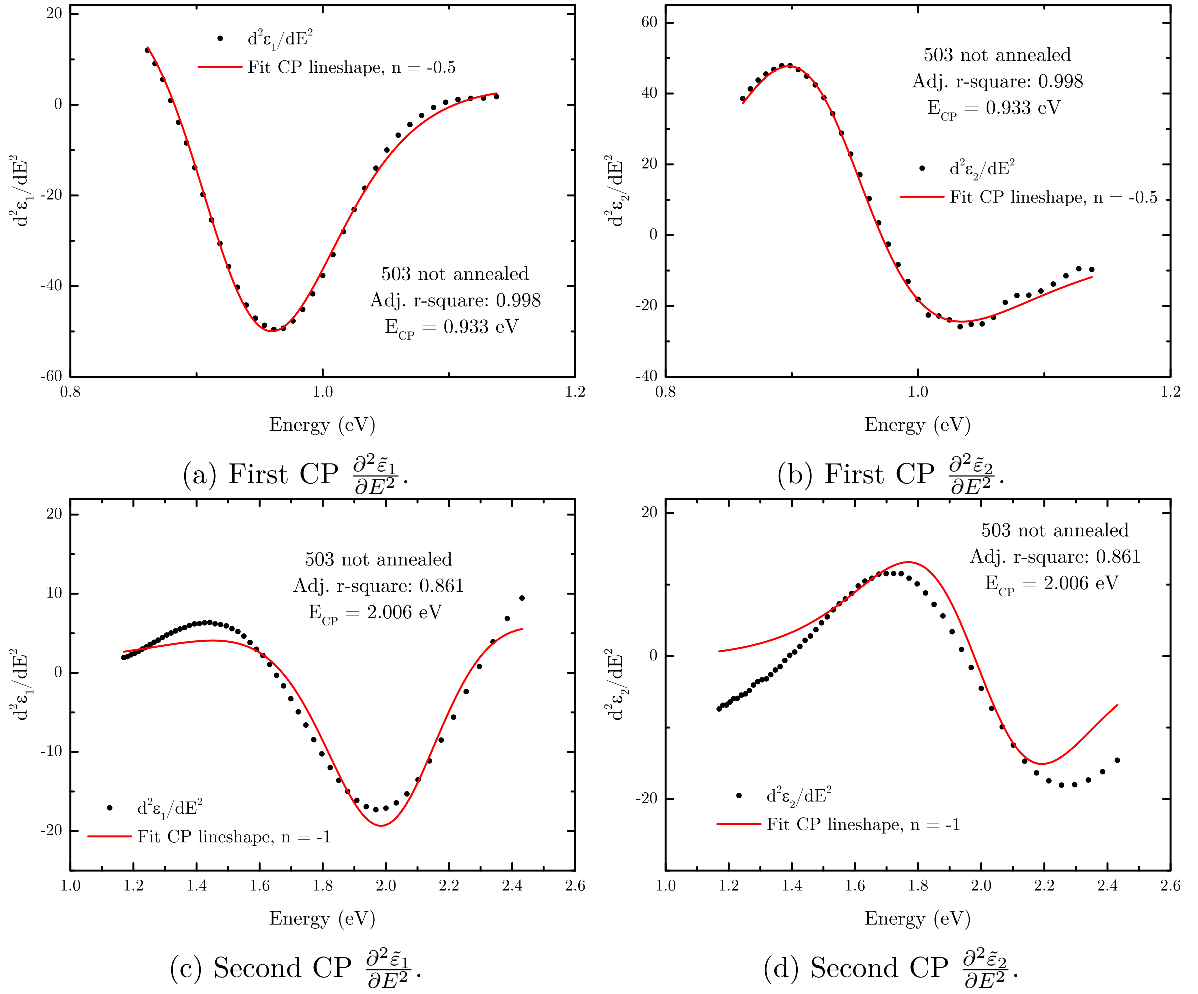

(a) First CP $\frac{\partial^2 \tilde{\varepsilon}_1}{\partial E^2}$.

(b) First CP $\frac{\partial^2 \tilde{\varepsilon}_2}{\partial E^2}$.

(c) Second CP $\frac{\partial^2 \tilde{\varepsilon}_1}{\partial E^2}$.

(d) Second CP $\frac{\partial^2 \tilde{\varepsilon}_2}{\partial E^2}$.

Figure A.17.: 503 not annealed.

506 not annealed with ZnSe

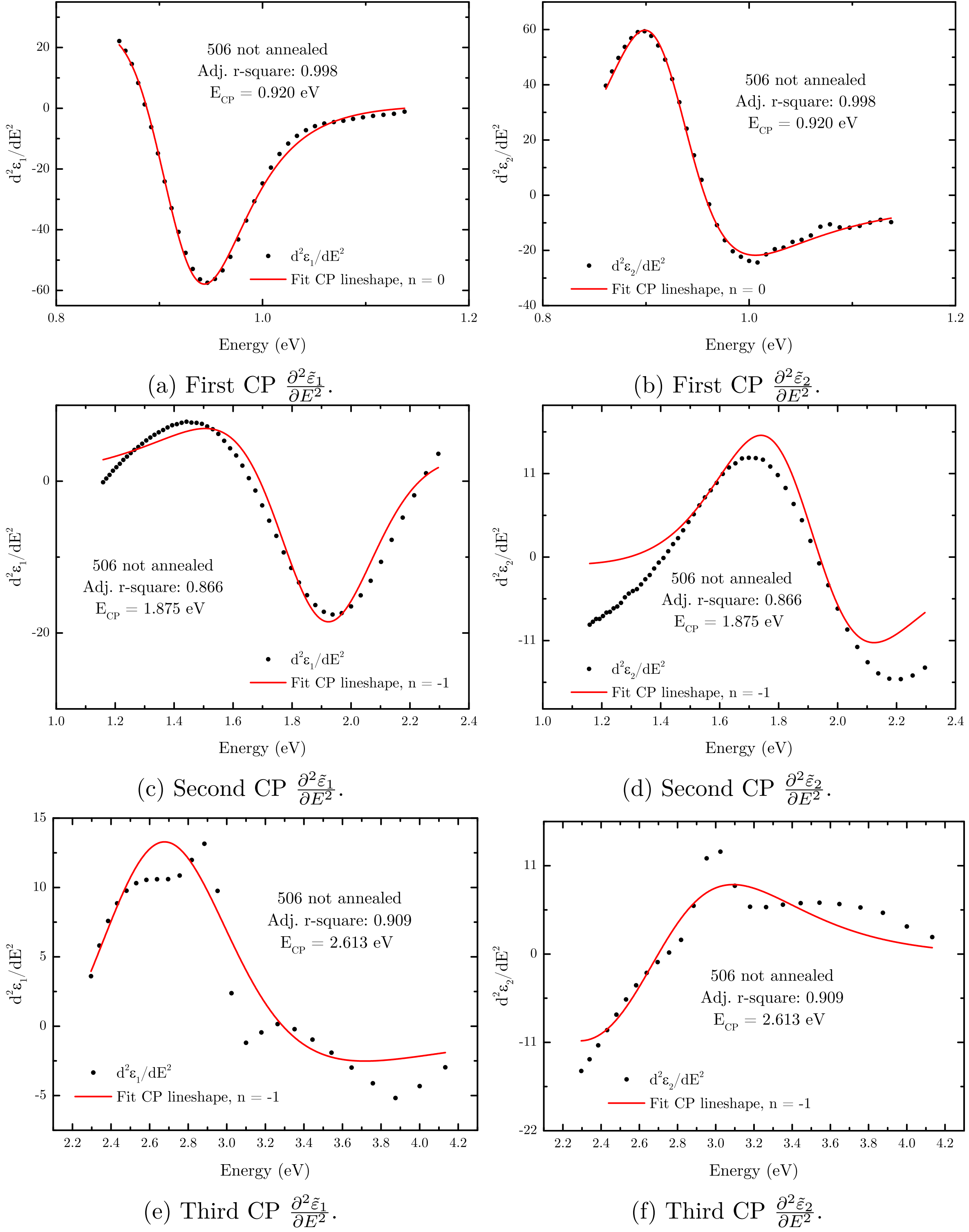

(a) First CP $\frac{\partial^2 \tilde{\varepsilon}_1}{\partial E^2}$. (b) First CP $\frac{\partial^2 \tilde{\varepsilon}_2}{\partial E^2}$.

(c) Second CP $\frac{\partial^2 \tilde{\varepsilon}_1}{\partial E^2}$. (d) Second CP $\frac{\partial^2 \tilde{\varepsilon}_2}{\partial E^2}$.

(e) Third CP $\frac{\partial^2 \tilde{\varepsilon}_1}{\partial E^2}$. (f) Third CP $\frac{\partial^2 \tilde{\varepsilon}_2}{\partial E^2}$.

Figure A.18.: 506 not annealed.

499 not annealed ordered process 1 without ZnSe

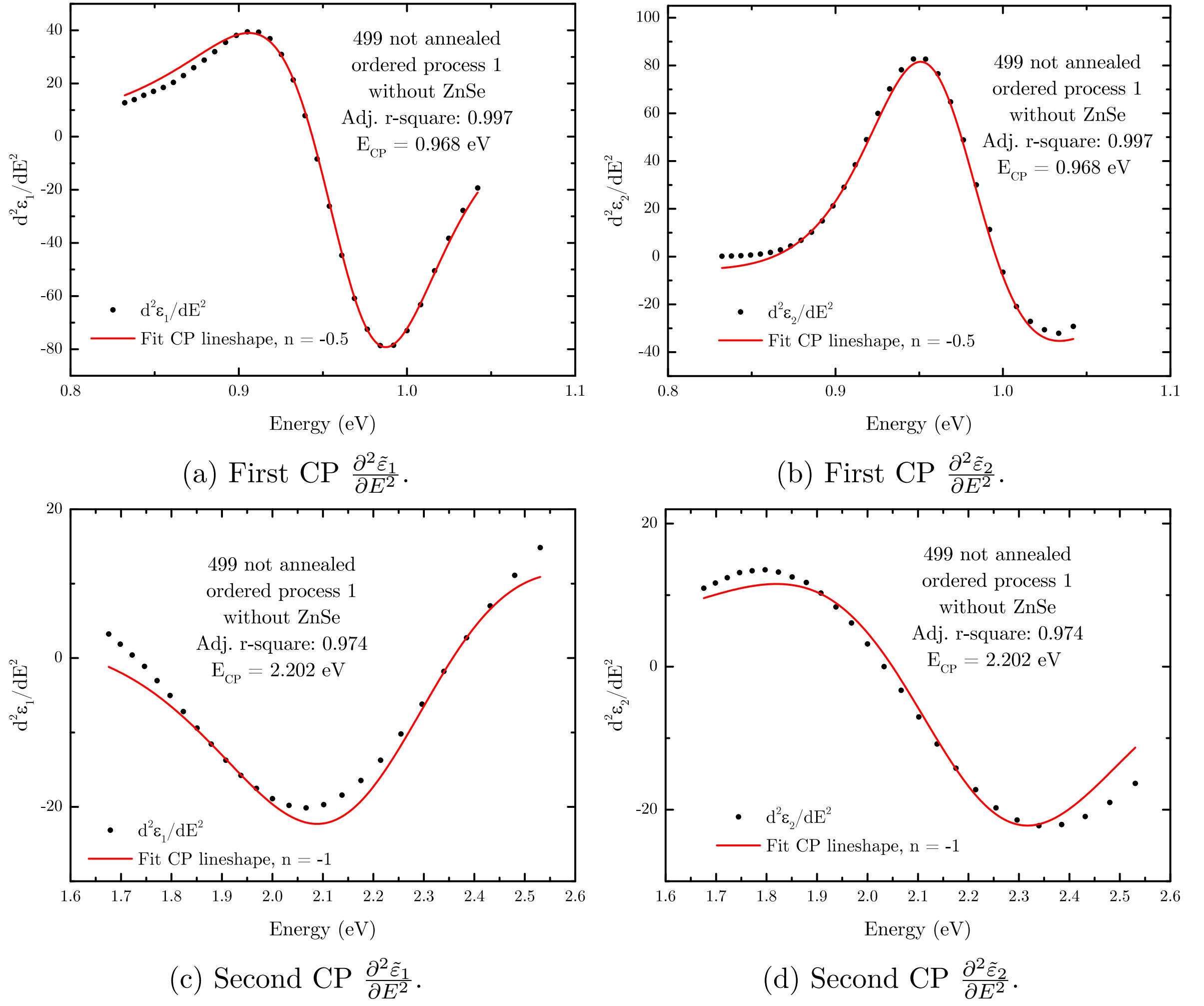

(a) First CP $\frac{\partial^2 \tilde{\varepsilon}_1}{\partial E^2}$.

(b) First CP $\frac{\partial^2 \tilde{\varepsilon}_2}{\partial E^2}$.

(c) Second CP $\frac{\partial^2 \tilde{\varepsilon}_1}{\partial E^2}$.

(d) Second CP $\frac{\partial^2 \tilde{\varepsilon}_2}{\partial E^2}$.

Figure A.19.: 499 not annealed ordered process 1 without ZnSe.

499 not annealed ordered process 2 without ZnSe

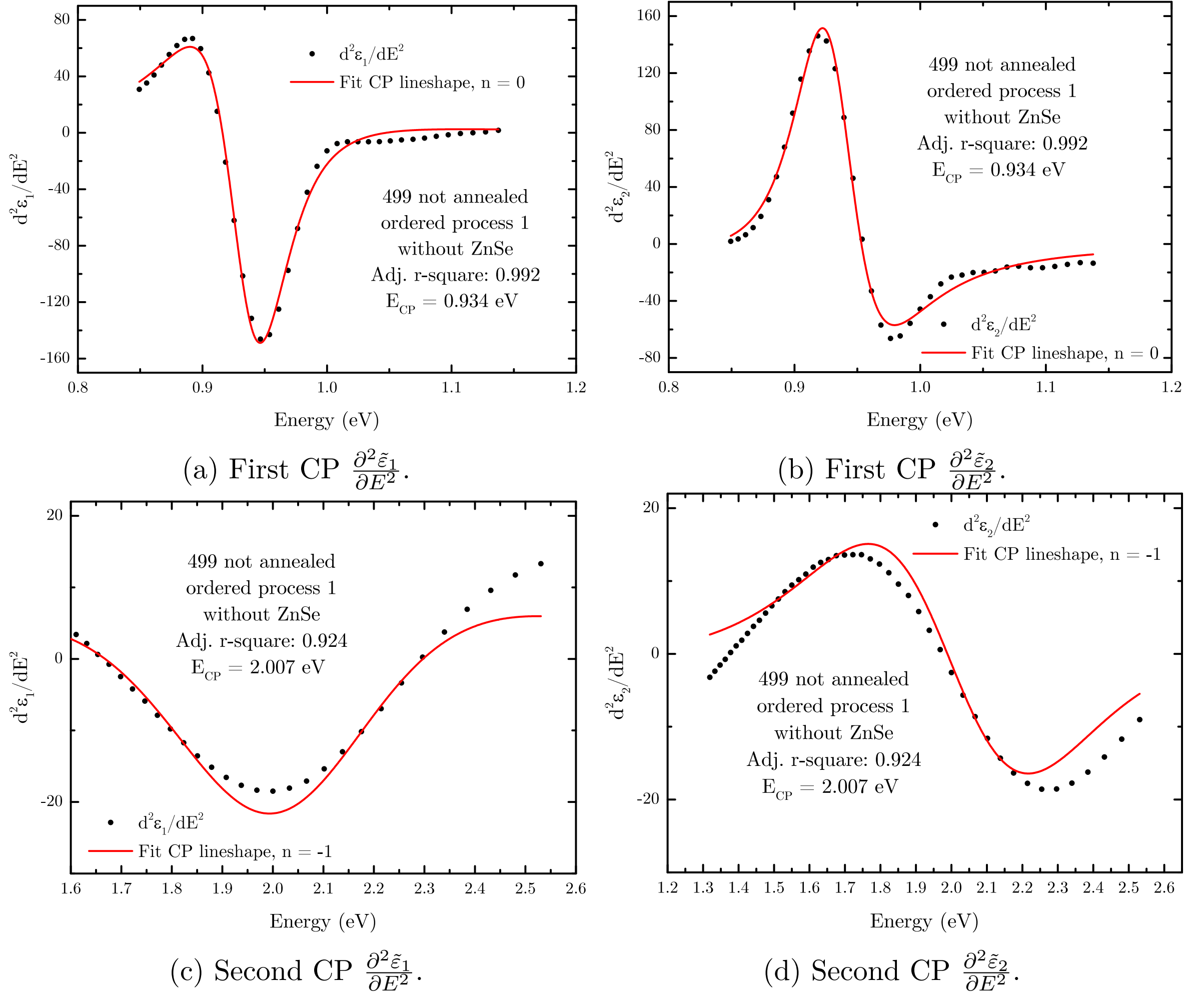

(a) First CP $\frac{\partial^2 \tilde{\varepsilon}_1}{\partial E^2}$.

(b) First CP $\frac{\partial^2 \tilde{\varepsilon}_2}{\partial E^2}$.

(c) Second CP $\frac{\partial^2 \tilde{\varepsilon}_1}{\partial E^2}$.

(d) Second CP $\frac{\partial^2 \tilde{\varepsilon}_2}{\partial E^2}$.

Figure A.20.: 499 not annealed ordered process 2 without ZnSe.

506 not annealed without ZnSe

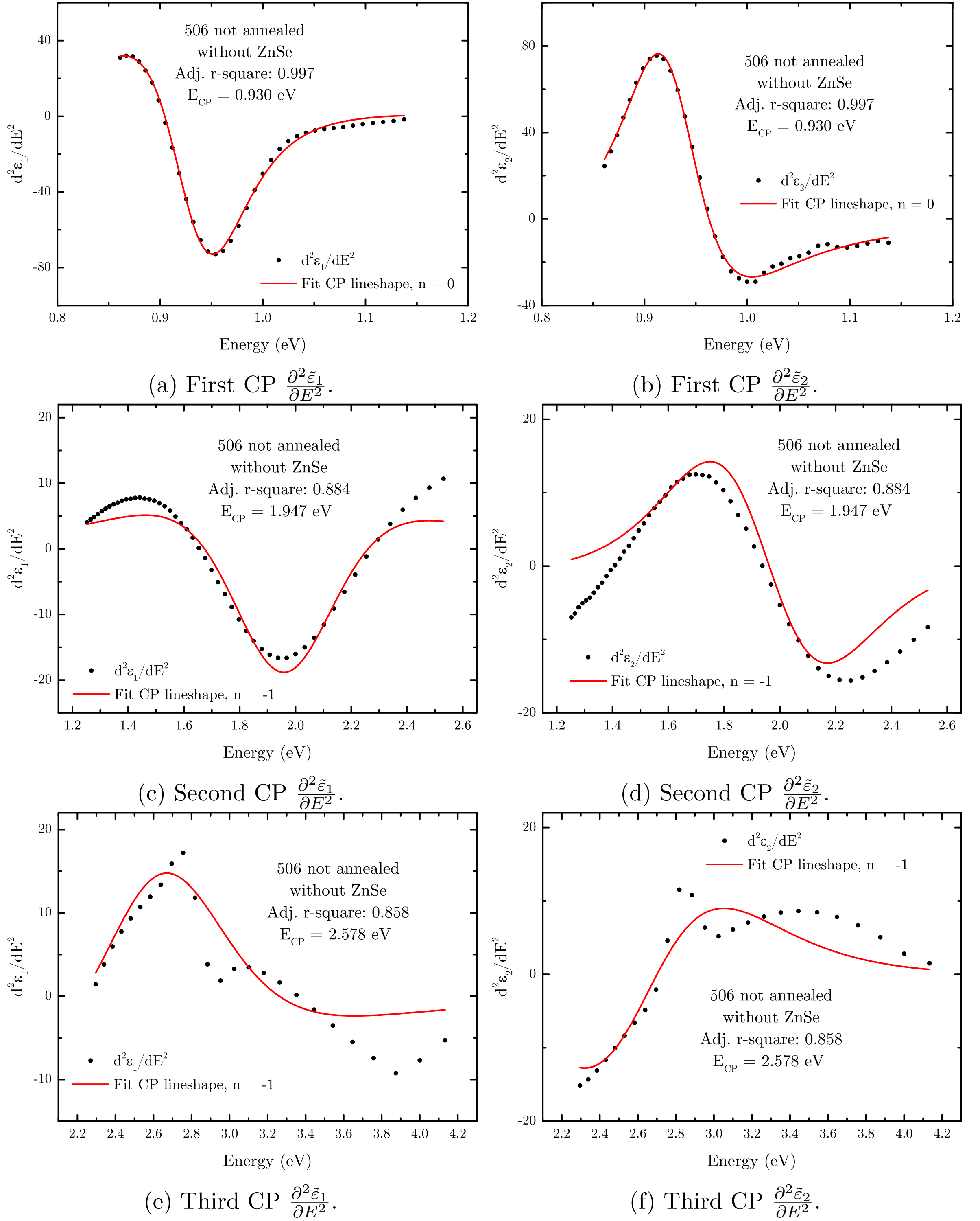

(a) First CP $\frac{\partial^2 \tilde{\varepsilon}_1}{\partial E^2}$.

(b) First CP $\frac{\partial^2 \tilde{\varepsilon}_2}{\partial E^2}$.

(c) Second CP $\frac{\partial^2 \tilde{\varepsilon}_1}{\partial E^2}$.

(d) Second CP $\frac{\partial^2 \tilde{\varepsilon}_2}{\partial E^2}$.

(e) Third CP $\frac{\partial^2 \tilde{\varepsilon}_1}{\partial E^2}$.

(f) Third CP $\frac{\partial^2 \tilde{\varepsilon}_2}{\partial E^2}$.

Figure A.21.: 506 not annealed without ZnSe.

486 annealed with ZnSe

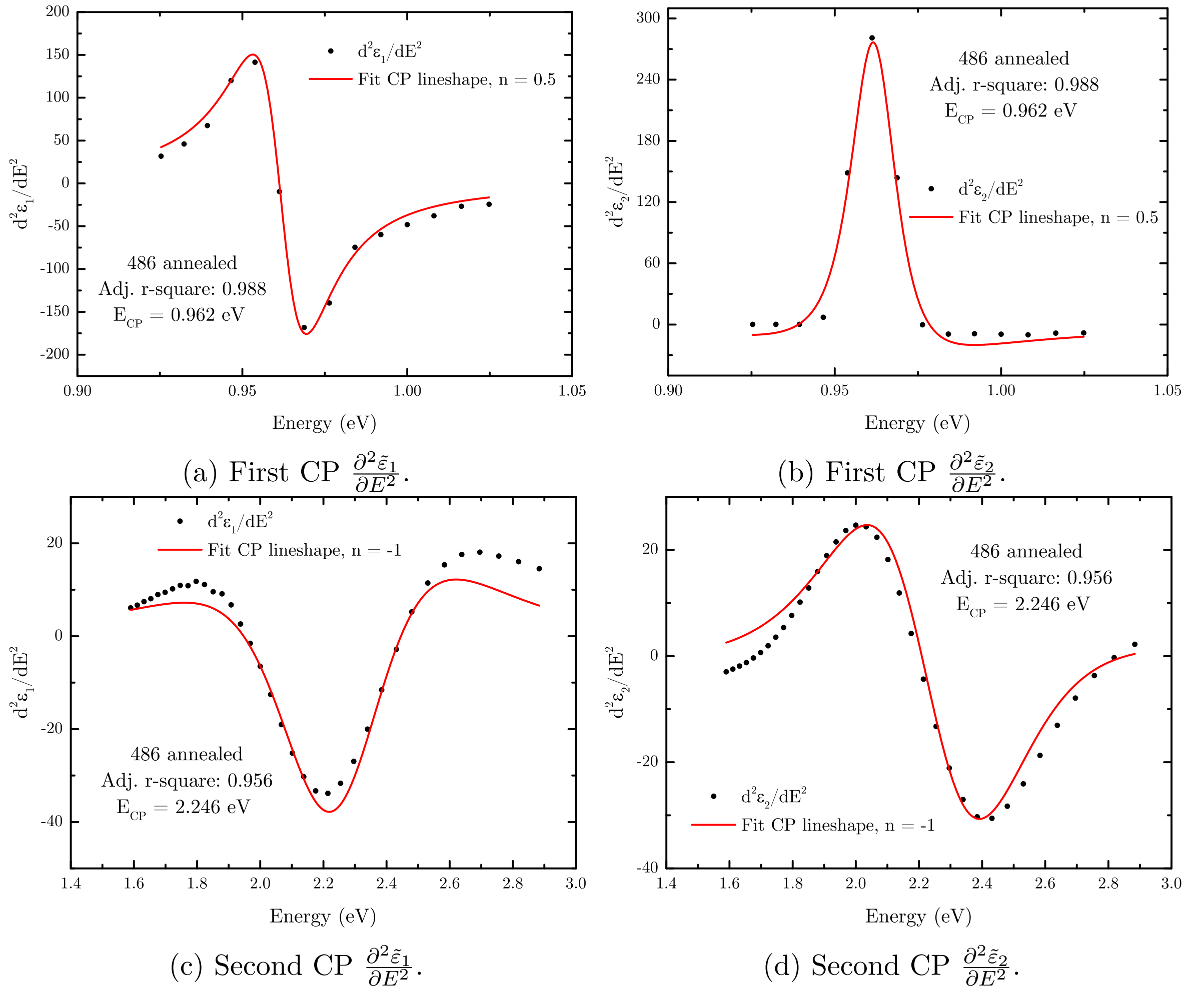

(a) First CP $\frac{\partial^2 \tilde{\varepsilon}_1}{\partial E^2}$.

(b) First CP $\frac{\partial^2 \tilde{\varepsilon}_2}{\partial E^2}$.

(c) Second CP $\frac{\partial^2 \tilde{\varepsilon}_1}{\partial E^2}$.

(d) Second CP $\frac{\partial^2 \tilde{\varepsilon}_2}{\partial E^2}$.

Figure A.22.: 486 annealed.

487 annealed with ZnSe

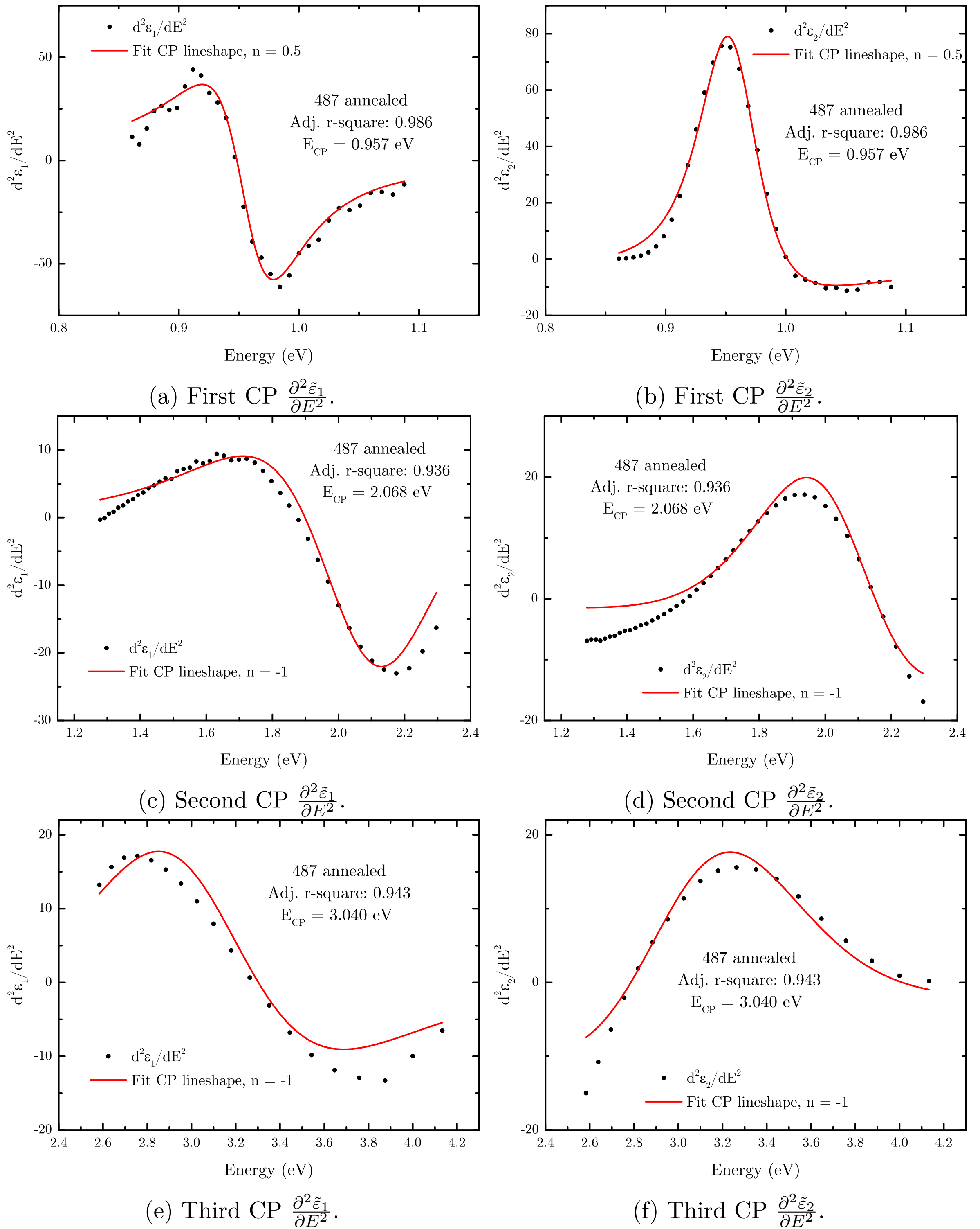

(a) First CP $\frac{\partial^2 \tilde{\varepsilon}_1}{\partial E^2}$.

(b) First CP $\frac{\partial^2 \tilde{\varepsilon}_2}{\partial E^2}$.

(c) Second CP $\frac{\partial^2 \tilde{\varepsilon}_1}{\partial E^2}$.

(d) Second CP $\frac{\partial^2 \tilde{\varepsilon}_2}{\partial E^2}$.

(e) Third CP $\frac{\partial^2 \tilde{\varepsilon}_1}{\partial E^2}$.

(f) Third CP $\frac{\partial^2 \tilde{\varepsilon}_2}{\partial E^2}$.

Figure A.23.: 487 annealed.

A.4. Remaining PL Spectra

In this section the evolution of the remaining PL spectra with temperature are shown. The k-values (equation 4.16) are now shown here, since they are 1 at all temperatures. The only two exceptions are the not annealed sample 506 at 4 K and the disordered piece of the not annealed sample 499, for which the k-values were not determined. These samples are shown in figures 4.8 and 4.16 respectively.

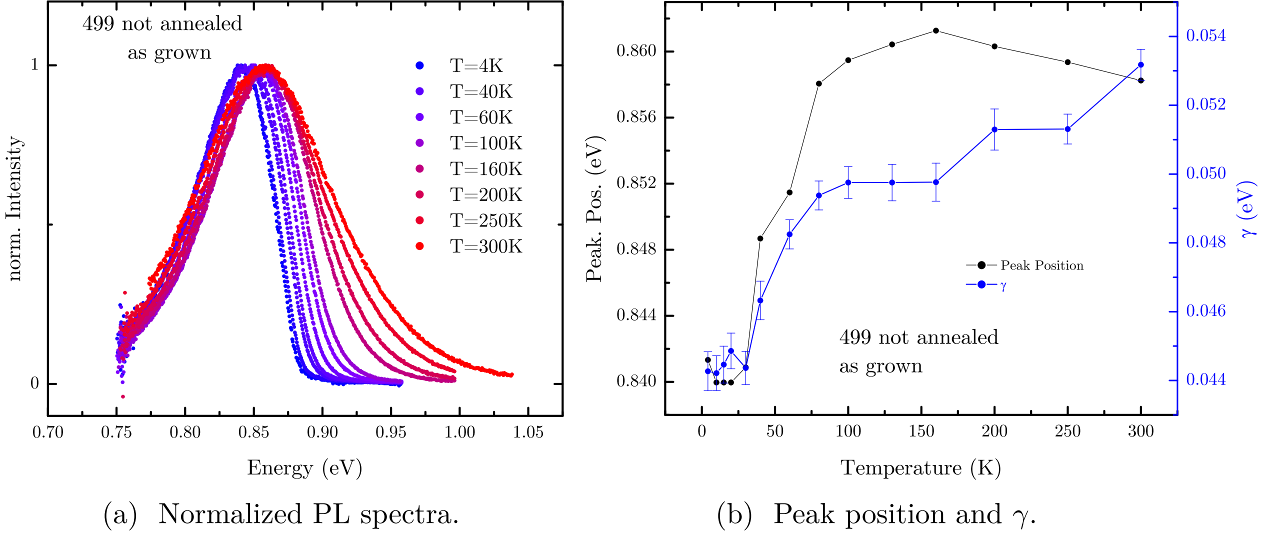

(a) Normalized PL spectra.

(b) Peak position and γ.

Figure A.24.: Evolution of the PL emission with temperature of the not annealed, as grown sample 499.

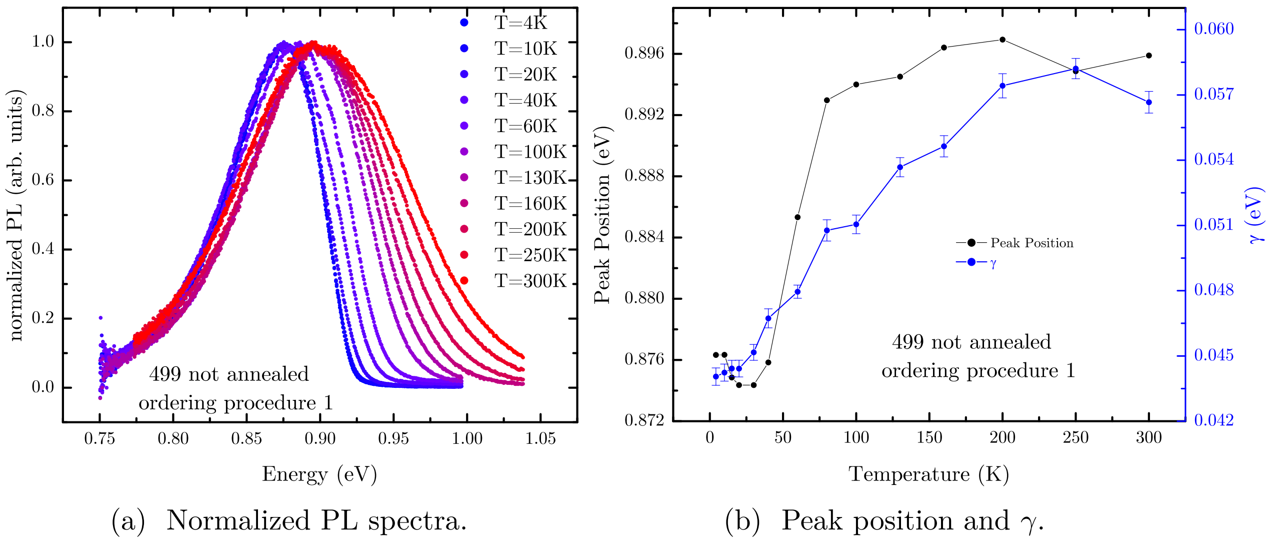

(a) Normalized PL spectra.

(b) Peak position and γ.

Figure A.25.: Evolution of the PL emission with temperature of the not annealed sample 499, treated with the ordering procedure 1.

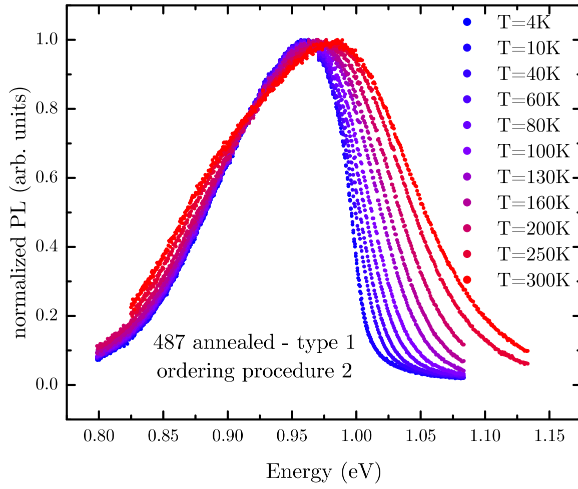

(a) Normalized PL spectra.

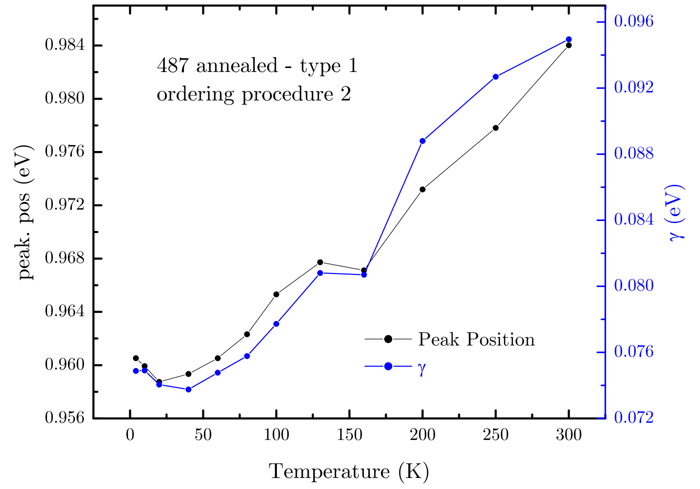

(b) Peak position and γ.

Figure A.26.: Evolution of the PL emission with temperature of the annealed sample 487, treated with the ordering procedure 2.

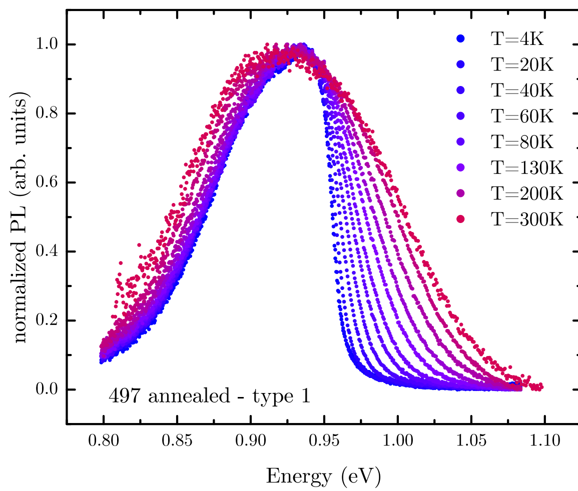

(a) Normalized PL spectra.

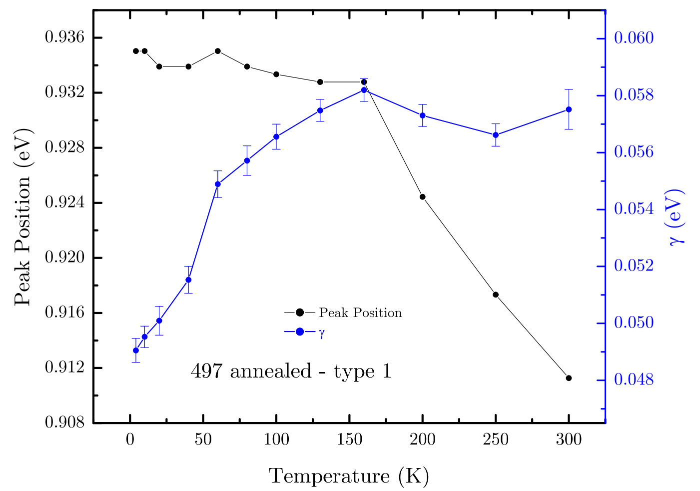

(b) Peak position and γ.

Figure A.27.: Evolution of the PL emission with temperature of the annealed sample 497.

B. Acknowledgement

There are many people, who supported me in writing this thesis and to whom I am very grateful.

First and foremost, I would like to start by thanking my supervisor Susanne Siebentritt for giving me the opportunity to do my PhD at the Laboratory of Photovoltaics on this challenging topic. Thank you for your guidance and your patience, especially in discussing the infamous Osipov paper, which in the end led to our, I hope at least somewhat correct, understanding of the PL of the epitaxial samples.

Alex Redinger for helping me find my way in the world of semiconductors and solar cells, which was in large parts uncharted territory for me, especially for the PVD training and of course for being part of my CET committee.

Charlotte Platzer Björkman, also for being part of my CET committee. But more importantly, thank you for having me at the Ångström laboratory in Uppsala and for allowing me to perform the ellipsometry measurements. Thank you for letting my keep the WVASE dongle for so long.

Roland Sanctuary and Jan Lagerwall for agreeing to be part of my jury.

I would like to thank all of my colleagues from LPV, LEM and LIST for helping make my PhD the great experience, that it was. I am especially grateful to David and Rabie for helping me getting started with PL. The ”PL gang” for discussions and help in the lab. Maxime and Michele for the SEM and EDX measurements. Florian for the Hall measurements. Hiroki for the XRD measurements. Tobias Bertram for proofreading of this thesis. Thomas Schuler for technical and IT support. Patricia for taking care of all organisational things. Mads from LIST for taking the time for Raman measurements despite writing his own thesis. My office colleagues for making our office maybe not the quietest, but certainly the most fun and endearing one.

I would also like to acknowledge the Kestcells project. Not only for funding this work, but also for organizing a very nice training network including the courses at the ESADE business school and extended stays at partnering institutes. In that regard I would also like to thank the PV group at the Ångström laboratory for making my stay there as pleasant as it was. In particular I would like to thank Carl and Shuyi for their help with the ellipsometer and with the data analysis.

Last, but certainly not least, I want to express my gratitude towards those people outside of the scientific world, who gave me the support, that was necessary to see this thesis to completion and who were understanding at those times, when I needed to give my undivided attention to my work: My parents and my two sisters. My friends, especially Judith, Stefan and Moritz and my fellow ”Avoid” bandmates and friends Matze, Paul, Pablo and Hanna.

C. List of Publications

Publications in Peer-reviewed Journals

1. J. Sendler, M. Thevenin, F. Werner, A. Redinger, S. Li, Ca. Hägglund, Ch. Platzer-Björkman and S. Siebentritt. Photoluminescence studies in epitaxial CZTSe thin films. *Journal of Applied Physics* 120(12):125701, 2016.

2. A. Redinger, Djemour, T. P. Weiss, J. Sendler and S. Siebentritt. Molecular beam epitaxy of Cu2ZnSnSe4 thin films grown on GaAs(001). In *2013 IEEE 39th Photovoltaic Specialists Conference (PVSC)*, pages 0420 - 0425, June 2013.

3. G. Rey, A. Redinger, J. Sendler, T. P. Weiss, M. Thevenin, M. Guennou, B. El Adib, and S. Siebentritt. The band gap of Cu2ZnSnSe4: Effect of order-disorder. *Applied Physics Letters*, 105(11):112106, 2014.

4. A.Redinger, H. Groiss, J. Sendler, R. Djemour, D. Regesch, D. Gerthsen and S. Siebentritt. Epitaxial Cu2ZnSnSe4 thin films and devices. *Thin Solid Films*, 582: 193-197, 2015.

5. H. Meadows, D. Regesch, M. Thevenin, J. Sendler, T. Schuler, S. Misra, B. Simonds, M. Scarpulla, V. Gerlitz, L. Gütay, J. Guillot and P. Dale. CuInSe2 semiconductor formation by laser annealing. *Thin Solid Films*, 582:23 - 26, 2015

6. J.Malaquias, D. Berg, J. Sendler, M. Steichen, N. Valle and P.J. Dale. Controlled bandgap $CuIn_{1-x}Ga_x(S_{0.1}Se_{0.9})_2$ $(0.10 \leq x \leq 0.72)$ solar cells from electrodeposited precursors *Thin Solid Films*, 582:2 - 6, 2015

7. M.Mousel, T.Schwarz, R. Djemour, T. P Weiss, J. Sendler, J. Malaquias, A. Redinger, O. Cojocaru-Mirédin, P.-P. Choi and S. Siebentritt. Cu-rich precursors improve kesterite solar cells. *Advanced Energy Materials* 4(2), 2014.

8. G. Rey, T.P. Weiss, J. Sendler, A. Finger, C. Spindler, F. Werner, M. Melchiorre, M. Hála, M. Guennou, S. Siebentritt. Ordering kesterite improves solar cells: A low temperature post-deposition annealing study. *Solar Energy Materials and Solar Cells*, 151:131 - 138, 2016.

9. S. Siebentritt, G. Rey, A. Finger, D. Regesch, J. Sendler, T.P. Weiss, T. Bertram. What is the bandgap of kesterite? *Solar Energy Materials and Solar Cells*, 158, Part 2:126 - 129, 2016.

10. J. J. S. Scragg, J. K. Larsen, M. Kumar, C. Persson, J. Sendler, S. Siebentritt and C. Platzer Björkman. Cu-Zn disorder and band gap fluctuations in Cu2ZnSn(S,Se)4: Theoretical and experimental investigations. *Physica Status Solidi (b)*, 253(2):247 - 254, 2016.

Conference Contributions

1. J. Sendler, A. Redinger, R. Djemour and S. Siebentritt. Optical characterization of epitaxial CZTSe absorbers with varying Cu-content. In *4th European Kesterite Workshop*, Berlin, Germany, 2013 (Poster).

2. J. Sendler, G. Rey and S. Siebentritt. Photoluminescence in epitaxial CZTSe with strong tailing. In *5th European Kesterite Workshop*, Tallinn, Estonia, 2014 (Oral presentation).

3. A. Redinger, J. Sendler, R. Djemour, H. Groiss, D. Gerthsen and S. Siebentritt. Epitaxial Cu2ZnSnSe4In. In *E-MRS*, Lille, France, 2014 (Poster).

4. Garcia-Llamas, J.M. Merino, R. Caballero, J.M. Cano-Torres, D. Regesch, J. Sendler, S. Siebentritt and M. León. Synthesis of Cu_2ZnSnS_4 from different routes by solid state reaction. In *4th European Kesterite Workshop*, Berlin, Germany, 2013 (Poster).

5. C. Spindler, J. Sendler and S. Siebentritt. Excitation dependence of photoluminescence transitions. In *Gordon Conference on Defects in Semiconductors*, New London, USA, 2016 (Poster).

Bibliography

[1] GISS Surface Temperature Analysis. http://data.giss.nasa.gov/gistemp/graphs/. Accessed: 2016-11-29.

[2] *Climate Change 2013 The Physical Science Basis*. Cambridge University Press, 2013.

[3] J. Cook, N. Oreskes, P. T. Doran, W. R. L. Anderegg, B. Verheggen, E. W. Maibach, J. S. Carlton, S. Lewandowsky, A. G. Skuce, S. A. Green, D. Nuccitelli, P. Jacobs, M. Richardson, B. Winkler, R. Painting, and K. Rice. Consensus on consensus: a synthesis of consensus estimates on human-caused global warming. *Environmental Research Letters*, 11(4):048002, 2016.

[4] Eurostat - Greenhouse gas emission statistics. http://ec.europa.eu/eurostat/statistics-explained/index.php/Greenhouse_gas_emission_statistics. Accessed: 2016-11-30.

[5] R. Knutti, J. Rogelj, J. Sedlacek, and E. M. Fischer. A scientific critique of the two-degree climate change target. *Nature Geosci*, 9(1):13–18, Jan 2016.

[6] REN21 - Renewables 2016 Global Staus Report. http://www.ren21.net/status-of-renewables/global-status-report/. Accessed: 2016-11-30.

[7] European Comission - Climate Action. http://ec.europa.eu/clima/policies/strategies/2020_en. Accessed: 2016-11-30.

[8] International Energy Agency - Photovoltaic Power systems. Annual Report 2015. http://iea-pvps.org/index.php?id=6\&eID=dam_frontend_push\&docID=3195, 2016. Accessed: 2016-11-30.

[9] F. institute. *Fraunhofer Institute photovoltaics report*. 2016, https://www.ise.fraunhofer.de/de/downloads/pdf-files/aktuelles/photovoltaics-report-in-englischer-sprache.pdf.

[10] B. Mattson. 7 Reasons Thin Film Is Alive and Set to Win in Solar. http://www.renewableenergyworld.com/articles/2014/07/7-reasons-thin-film-is-alive-and-set-to-win-in-solar.html, 2014. Accessed: 2016-11-30.

[11] V. Fthenakis. Sustainability of photovoltaics: The case for thin-film solar cells. *Renewable and Sustainable Energy Reviews*, 13(9):2746 – 2750, 2009.

[12] M. P. Paranthaman, W. Wong-Ng, and R. N. Bhattacharya, editors. *Semiconductor Materials for Solar Photovoltaic Cells*, volume 218 of *Springer Series in Materials Science*. Springer International Publishing, 1 edition, 2016.

[13] I. Repins, C. Beall, N. Vora, C. DeHart, D. Kuciauskas, P. Dippo, B. To, J. Mann, W.-C. Hsu, A. Goodrich, and R. Noufi. Co-evaporated Cu2ZnSnSe4 films and devices. *Solar Energy Materials and Solar Cells*, 101:154 – 159, 2012.

[14] W. Wang, M. T. Winkler, O. Gunawan, T. Gokmen, T. K. Todorov, Y. Zhu, and D. B. Mitzi. Device Characteristics of CZTSSe Thin-Film Solar Cells with 12.6 % Efficiency. *Advanced Energy Materials*, 4(7), 2014.

[15] Y. S. Lee, T. Gershon, O. Gunawan, T. K. Todorov, T. Gokmen, Y. Virgus, and S. Guha. Cu2ZnSnSe4 Thin-Film Solar Cells by Thermal Co-evaporation with 11.6 % Efficiency and Improved Minority Carrier Diffusion Length. *Advanced Energy Materials*, 5(7), 2015.

[16] H. Hiroi, N. Sakai, T. Kato, and H. Sugimoto. High voltage Cu2ZnSnS4 submodules by hybrid buffer layer. In *2013 IEEE 39th Photovoltaic Specialists Conference (PVSC)*, pages 0863–0866, June 2013. doi: 10.1109/PVSC.2013.6744281.

[17] S. F. press release. Solar Frontier Achieves World Record Thin-Film Solar Cell Efficiency: 22.3 %, 2015, http://www.solar-frontier.com/eng/news/2015/C051171.html.

[18] P. Jackson, R. Wuerz, D. Hariskos, E. Lotter, W. Witte, and M. Powalla. Effects of heavy alkali elements in Cu(In,Ga)Se2 solar cells with efficiencies up to 22.6 %. *physica status solidi (RRL) âĂŞ Rapid Research Letters*, 10(8):583–586, 2016.

[19] K. Masuko, M. Shigematsu, T. Hashiguchi, D. Fujishima, M. Kai, N. Yoshimura, T. Yamaguchi, Y. Ichihashi, T. Mishima, N. Matsubara, T. Yamanishi, T. Takahama, M. Taguchi, E. Maruyama, and S. Okamoto. Achievement of More Than 25 % Conversion Efficiency With Crystalline Silicon Heterojunction Solar Cell. *IEEE Journal of Photovoltaics*, 4(6):1433–1435, Nov 2014.

[20] S. Siebentritt. Why are kesterite solar cells not 20 % efficient? *Thin Solid Films*, 535:1 – 4, 2013.

[21] T. Gokmen, O. Gunawan, T. K. Todorov, and D. B. Mitzi. Band taitail and efficiency limitation in kesterite solar cells. *Applied Physics Letters*, 2013.

[22] D. A. R. Barkhouse, O. Gunawan, T. Gokmen, T. K. Todorov, and D. B. Mitzi. Device characteristics of a 10.1 % hydrazine-processed Cu2ZnSn(Se,S)4 solar cell. *Progress in Photovoltaics: Research and Applications*, 20(1):6–11, 2012.

[23] Kestcells Project. `http://kestcells.eu/`. Accessed: 2016-11-30.

[24] J. B. Li, V. Chawla, and B. M. Clemens. Investigating the Role of Grain Boundaries in CZTS and CZTSSe Thin Film Solar Cells with Scanning Probe Microscopy. *Advanced Materials*, 24(6):720–723, 2012.

[25] S. Schorr. The crystal structure of kesterite type compounds: A neutron and X-ray diffraction study. *Solar Energy Materials and Solar Cells*, 95(6):1482 – 1488, 2011.

[26] J. Paier, R. Asahi, A. Nagoya, and G. Kresse. Cu_2ZnSnS_4 as a potential photovoltaic material: A hybrid Hartree-Fock density functional theory study. *Phys. Rev. B*, 79: 115126, Mar 2009.

[27] C. Persson. Electronic and optical properties of Cu2ZnSnS4 and Cu2ZnSnSe4. *Journal of Applied Physics*, 2010.

[28] S. Siebentritt and S. Schorr. Kesterites - a challenging material for solar cells. *Progress in Photovoltaics: Research and Applications*, 20(5):512–519, 2012.

[29] S. Chen, A. Walsh, J.-H. Yang, X. G. Gong, L. Sun, P.-X. Yang, J.-H. Chu, and S.-H. Wei. Compositional dependence of structural and electronic properties of $Cu_2ZnSn(S,Se)_4$ alloys for thin film solar cells. *Phys. Rev. B*, 83:125201, Mar 2011.

[30] S. Botti, D. Kammerlander, and M. A. L. Marques. Band structures of Cu2ZnSnS4 and Cu2ZnSnSe4 from many-body methods. *Applied Physics Letters*, 98(24):241915, 2011.

[31] G. H. Vineyard. Theory of Order-Disorder Kinetics. *Phys. Rev.*, 102:981–992, May 1956.

[32] J. Scragg, L. Chubrac, A. Lafond, T. Ericson, and C. Platzer-Björkman. A low-temperature order-disorder transition in Cu2ZnSnS4 thin films. *Applied Physics Letters*, 2014.

[33] G. Rey, A. Redinger, J. Sendler, T. P. Weiss, M. Thevenin, M. Guennou, B. El Adib, and S. Siebentritt. The band gap of Cu2ZnSnSe4: Effect of order-disorder. *Applied Physics Letters*, 105(11):112106, 2014.

[34] I. Olekseyuk, I. Dudchak, and L. Piskach. Phase equilibria in the Cu2S-ZnS-SnS2 system. *Journal of Alloys and Compounds*, 368(1-2):135 – 143, 2004.

[35] A. Redinger, R. Djemour, T. P. Weiss, J. Sendler, S. Siebentritt, and L. Gütay. Molecular beam epitaxy of Cu2ZnSnSe4 thin films grown on GaAs(001). In *2013 IEEE 39th Photovoltaic Specialists Conference (PVSC)*, pages 0420–0425, June 2013. doi: 10.1109/PVSC.2013.6744181.

[36] A. Walsh, S. Chen, S.-H. Wei, and X.-G. Gong. Kesterite Thin-Film Solar Cells: Advances in Materials Modelling of Cu2ZnSnS4. *Advanced Energy Materials*, 2(4): 400–409, 2012.

[37] U. W. Pohl. *Epitaxy of Semiconductors*. Springer-Verlag Berlin Heidelberg, 2013.

[38] J. S. Blakemore. Semiconducting and other major properties of gallium arsenide. *Journal of Applied Physics*, 53(10):R123–R181, 1982.

[39] C. Krämmer, M. Lang, A. Redinger, J. Sachs, C. Gao, H. Kalt, S. Siebentritt, and M. Hetterich. Assessment of crystal quality and unit cell orientation in epitaxial Cu2ZnSnSe4 layers using polarized Raman scattering. *Opt. Express*, 22(23):28240–28246, Nov 2014.

[40] A. Redinger, D. M. Berg, P. J. Dale, and S. Siebentritt. The Consequences of Kesterite Equilibria for Efficient Solar Cells. *Journal of the American Chemical Society*, 133(10):3320–3323, 2011.

[41] J. Goldstein, D. E. Newbury, D. C. Joy, C. E. Lyman, P. Echlin, E. Lifshin, L. Sawyer, and J. Michael. *Scanning Electron Microscopy and X-ray Microanalysis*. Springer US, 3 edition, 2003.

[42] A. Redinger, H. Groiss, J. Sendler, R. Djemour, D. Regesch, D. Gerthsen, and S. Siebentritt. Epitaxial Cu2ZnSnSe4 thin films and devices. *Thin Solid Films*, 582: 193 – 197, 2015.

[43] S. Hunklinger. *Festkörperphysik*. Oldenbourg, 2007. ISBN 9783486575620.

[44] T. international Center of Diffraction Data database PDF 00-032-0389, 2015.

[45] T. international Center of Diffraction Data database PDF 01-082-9984, 2015.

[46] P. Yu and M. Cardona. *Fundamentals of Semiconductors*. Springer-Verlag Berlin Heidelberg New York, 2 edition, 2003.

[47] R. Drago. *Physical Methods in Chemistry*. Philadelphia: Saunders, 1997.

[48] M. Guc, S. Levcenko, V. Izquierdo-Roca, X. Fontané, E. Arushanov, and A. Pérez-Rodríguez. Polarized Raman scattering analysis of Cu2ZnSnSe4 and Cu2ZnGeSe4 single crystals. *Journal of Applied Physics*, 114(19):193514, 2013.

[49] W. Taylor. The raman spectra of cubic zinc selenide and telluride. *Physics Letters A*, 24(10):556 – 558, 1967.

[50] R. Djemour, M. Mousel, A. Redinger, L. Gütay, A. Crossay, D. Colombara, P. J. Dale, and S. Siebentritt. Detecting ZnSe secondary phase in Cu2ZnSnSe4 by room temperature photoluminescence. *Applied Physics Letters*, 102(22):222108, 2013.

[51] R. Chandramohan, C. Sanjeeviraja, and T. Mahalingam. Preparation of Zinc Selenide Thin Films by Electrodeposition Technique for Solar Cell Applications. *physica status solidi (a)*, 163(2):R11–R12, 1997.

[52] A. A. Mitioglu, P. Plochocka, G. Deligeorgis, S. Anghel, L. Kulyuk, and D. K. Maude. Second-order resonant Raman scattering in single-layer tungsten disulfide WS_2. *Phys. Rev. B*, 89:245442, Jun 2014.

[53] M. Ishii, K. Shibata, and H. Nozaki. Anion Distributions and Phase Transitions in CuS1-xSex(x = 0-1) Studied by Raman Spectroscopy. *Journal of Solid State Chemistry*, 105(2):504 – 511, 1993.

[54] *Guide to Using WVASE: Spectroscopic Ellipsometry Data Acquisition and Analysis Software.*

[55] J. Moulder and J. Chastain. *Handbook of X-ray Photoelectron Spectroscopy: A Reference Book of Standard Spectra for Identification and Interpretation of XPS Data.* Physical Electronics Division, Perkin-Elmer Corporation, 1992. ISBN 9780962702624.

[56] T. Farrell. Surface oxides on Al, Cu, Sn, Pb, and some of their alloys: an ESCA study. *Metal Science*, 10(3):87–93, 1976.

[57] L. J. van der Pauw. *Philips Technical Review*, 20:220–224, 1958.

[58] W. Demtröder. *Experimentalphysik 2.* Springer-Verlag Berlin Heidelberg, 2013.

[59] J. Huml/’iček. 1 - Polarized Light and Ellipsometry. In H. G. Tompkins and E. A. Irene, editors, *Handbook of Ellipsometry*, pages 3 – 91. William Andrew Publishing, Norwich, NY, 2005.

[60] G. R. Fowles. *Introduction to Modern Optics.* Dover Publications, 1975.

[61] L. Van Hove. The Occurrence of Singularities in the Elastic Frequency Distribution of a Crystal. *Phys. Rev.*, 89:1189–1193, Mar 1953.

[62] S. Loughin, R. H. French, L. K. D. Noyer, W.-Y. Ching, and Y.-N. Xu. Critical point analysis of the interband transition strength of electrons. *Journal of Physics D: Applied Physics*, 29(7):1740, 1996.

[63] R. W. Collins, I. An, and C. Chen. 5 - Rotating Polarizer and Analyzer Ellipsometry. In H. G. Tompkins and E. A. Irene, editors, *Handbook of Ellipsometry*, pages 329 – 432. William Andrew Publishing, Norwich, NY, 2005.

[64] G. E. J. Jr. 3 - Data Analysis for Spectroscopic Ellipsometry. In H. G. Tompkins and E. A. Irene, editors, *Handbook of Ellipsometry*, pages 237 – 296. William Andrew Publishing, Norwich, NY, 2005.

[65] D. W. Marquardt. An algorithm for least-squares estimation of nonlinear parameters. *SIAM Journal on Applied Mathematics*, 11(2):431–441, 1963.

[66] A. Redinger, K. Hönes, X. Fontané, V. Izquierdo-Roca, E. Saucedo, N. Valle, A. Pérez-Rodríguez, and S. Siebentritt. Detection of a ZnSe secondary phase in co-evaporated Cu2ZnSnSe4 thin films. *Applied Physics Letters*, 98(10):101907, 2011.

[67] S. Zollner. Model dielectric functions for native oxides on compound semiconductors. *Applied Physics Letters*, 63(18):2523–2524, 1993.

[68] N. A. Torkhov. Formation of a native-oxide structure on the surface of n-GaAs under natural oxidation in air. *Semiconductors*, 37(10):1177–1184, 2003.

[69] J. Zuo and A. Erbe. Optical and electronic properties of native zinc oxide films on polycrystalline Zn. *Phys. Chem. Chem. Phys.*, 12:11467–11476, 2010.

[70] S. G. Choi, H. Y. Zhao, C. Persson, C. L. Perkins, A. L. Donohue, B. To, A. G. Norman, J. Li, and I. L. Repins. Dielectric function spectra and critical-point energies of Cu2ZnSnSe4 from 0.5 to 9.0 eV. *Journal of Applied Physics*, 111(3): 033506, 2012.

[71] H. Zhao and C. Persson. Optical Properties of Cu(In,Ga)Se2 and Cu2ZnSn(S,Se)4. *Thin Solid Films*, 2011.

[72] M. Cardona. *Solid State Physics, Suppl. 11: Modulation Spectroscopy*. Solid State Physics : Advances in Research and Applications. Academic Press, 1969.

[73] J. I. Pankove. *Optical processes in semiconductors*. Dover Publications, 1975.

[74] P. Lautenschlager, M. Garriga, S. Logothetidis, and M. Cardona. Interband critical points of GaAs and their temperature dependence. *Phys. Rev. B*, 35:9174–9189, Jun 1987.

[75] Y. Sun, S. E. Thompson, and T. Nishida. Physics of strain effects in semiconductors and metal-oxide-semiconductor field-effect transistors. *Journal of Applied Physics*, 101(10):104503, 2007.

[76] V. Palankovski, G. Kaiblinger-Grujin, and S. Selberherr. Study of dopant-dependent band gap narrowing in compound semiconductor devices. *Materials Science and Engineering: B*, 66(1âĂŞ3):46 – 49, 1999.

[77] Y. Hirate, H. Tampo, S. Minoura, H. Kadowaki, A. Nakane, K. M. Kim, H. Shibata, S. Niki, and H. Fujiwara. Dielectric functions of Cu2ZnSnSe4 and Cu2SnSe3 semiconductors. *Journal of Applied Physics*, 117(1):015702, 2015.

[78] M. Kuball, M. K. Kelly, M. Cardona, K. Köhler, and J. Wagner. Doping dependence of the E_1 and $E_1{+}\Delta_1$ critical points in highly doped n - and p -type GaAs: Importance of surface band bending and depletion. *Phys. Rev. B*, 49:16569–16574, Jun 1994.

[79] P. Würfel. *Physics of Solar Cells - From Principles to New Concepts.* Wiley-VCH, 2005.

[80] S. Siebentritt and U. Rau. *Wide-Gap Chalcopyrites, Chapter 7.* Springer, 2006.

[81] A. P. Levanyuk and V. V. Osipov. Edge luminescence of direct-gap semiconductors. *Physics-Uspekhi*, 24(3):187–215, 1981.

[82] P. Van Mieghem. Theory of band tails in heavily doped semiconductors. *Rev. Mod. Phys.*, 64:755–793, Jul 1992.

[83] A. L. Éfros. Electron localization in disordered systems (the anderson transition). *Soviet Physics Uspekhi*, 21(9):746, 1978.

[84] F. Scheck. *Theoretische Physik 2.* Springer Spektrum, 2013.

[85] Y. A. Goldberg. *Handbook Series on Semiconductor Parameters - Chapter 9*, volume 1. World Scientfic, 1996.

[86] K. A. Olive et al. Review of Particle Physics. *Chin. Phys.*, C38:090001, 2014.

[87] L. Gütay and G. Bauer. Local fluctuations of absorber properties of Cu(In,Ga)Se2 by sub-micron resolved {PL} towards “real life” conditions. *Thin Solid Films*, 517 (7):2222 – 2225, 2009.

[88] S. John, C. Soukoulis, M. H. Cohen, and E. N. Economou. Theory of electron band tails and the urbach optical-absorption edge. *Phys. Rev. Lett.*, 57:1777–1780, Oct 1986.

[89] B. Shklovskii and A. Efros. *Electronic Properties of Doped Semiconductors.* Springer-Verlag, 1984.

[90] P. W. Yu. Excitation-dependent emission in Mg-, Be-, Cd-, and Zn-implanted GaAs. *Journal of Applied Physics*, 48(12):5043–5051, 1977.

[91] S. M. Sze and K. K. Ng. *Physics of Semiconductor Devices.* Wiley, 2006.

[92] S. Choi, T. Kim, S. Hwang, J. Li, C. Persson, Y. Kim, S.-H. Wei, and I. Repins. Temperature dependent band-gap energy for Cu2ZnSnSe4: A spectroscopic ellipsometric study. *Solar Energy Materials and Solar Cells*, 130:375 – 379, 2014.

[93] S. Chen, A. Walsh, X.-G. Gong, and S.-H. Wei. Classification of Lattice Defects in the Kesterite Cu2ZnSnS4 and Cu2ZnSnSe4 Earth-Abundant Solar Cell Absorbers. *Advanced Materials*, 25(11):1522–1539, 2013.

[94] T. Schmidt, K. Lischka, and W. Zulehner. Excitation-power dependence of the near-band-edge photoluminescence of semiconductors. *Phys. Rev. B*, 45:8989–8994, Apr 1992.

[95] W. Grieshaber, E. F. Schubert, I. D. Goepfert, R. F. Karlicek, M. J. Schurman, and C. Tran. Competition between band gap and yellow luminescence in GaN and its relevance for optoelectronic devices. *Journal of Applied Physics*, 80(8):4615–4620, 1996.

[96] T. P. Weiss, A. Redinger, G. Rey, T. Schwarz, M. Spies, O. Cojocura-Mirédin, P.-P. Choi, and S. Siebentritt. Impact of annealing on electrical properties of Cu2ZnSnSe4 absorber layers. *Journal of Applied Physics*, 120(4):045703, 2016.

[97] G. Brammertz, Y. Ren, M. Buffière, S. Mertens, J. Hendrickx, H. Marko, A. E. Zaghi, N. Lenaers, C. Köble, J. Vleugels, M. Meuris, and J. Poortmans. Electrical characterization of Cu2ZnSnSe4 solar cells from selenization of sputtered metal layers. *Thin Solid Films*, 535:348 – 352, 2013.